

ABSTRACT

THOMPSON, SIMON THOMAS. Palladium-Rhenium Catalysts for Production of Chemicals and Fuels from Biomass. (Under the direction of H. Henry Lamb).

Catalytic hydrodeoxygenation (HDO) of organic liquids (“bio-oils”) obtained by pyrolysis of woody biomass offers a route to renewable hydrocarbons that could reduce our dependence on petroleum-derived transportation fuels. In the first phase of this research, a novel PdRe/C catalyst was developed that couples the hydrogenation activity of Pd and the C-O bond hydrogenolysis selectivity of Re. The PdRe/C catalyst was evaluated for HDO of guaiacol, a lignin pyrolysis model compound. Yields of benzene and cyclohexane over PdRe/C at 300°C and 1 atm are much greater than over Pd/C, Re/C or Ru/C (at comparable conversions). Pd/C is highly selective to phenol (and cyclohexanol), but this catalyst does not produce significant hydrocarbon yields, even at 100% guaiacol conversion. Re/C is active and moderately selective to benzene and cyclohexane, but this catalyst deactivates rapidly with time on stream. A substantial increase in HDO activity was observed for PdRe/C after higher reduction temperature (400°C, as compared to 300°C). Extended x-ray absorption fine structure (EXAFS) spectroscopy indicates intimate contact between the metals, as evidenced by a 2.70-Å Pd-Re bond distance. Scanning-transmission electron microscopy (STEM) with energy dispersive x-ray (EDX) imaging of the bimetallic catalyst shows Re clusters on the surface of larger Pd particles (10-50 nm). In summary, the catalysis and characterization results indicate that (1) the catalytically active sites comprise Re and Pd atoms and (2) bimetallic synergy enhances guaiacol HDO performance.

Selective hydrogenation of biomass-derived organic compounds provides an opportunity and means to offset use of petroleum for chemical intermediates. In the second phase of this research, PdRe/Al₂O₃ catalysts were demonstrated to be highly active and

selective for hydrogenation of furfural to furfuryl alcohol (FAL). PdRe/Al₂O₃ catalyst morphology depends on the Pd precursor and the sequence of metal precursor addition (via incipient wetness) to the γ -Al₂O₃ support. Enhanced performance in furfural hydrogenation correlates strongly with suppression of H₂ chemisorption (relative to CO chemisorption) after 400°C reduction. All reduced PdRe/Al₂O₃ catalysts exhibit surface contact between Re-rich and Pd-rich particles, as evidenced by STEM-EDX. Alloy formation is inferred for reduced catalysts prepared by co-impregnation, as evidenced by EXAFS spectroscopy and suppression of β -PdH_x formation in temperature-programmed hydride decomposition. Catalysts were prepared by two sequential impregnation methods: (1) impregnation of Re/Al₂O₃ with Pd salts and subsequent calcination and (2) impregnation of reduced and passivated Pd/Al₂O₃ with perrhenic acid, [HReO₄], without subsequent calcination. Irrespective of the preparation method, PdRe/Al₂O₃ catalysts prepared from [Pd(NH₃)₄(NO₃)₂] facilitate Re reduction at low temperatures—based on temperature-programmed reduction (TPR)—and are highly active in furfural hydrogenation. Small Pd particles (<5 nm) predominate in catalysts prepared from [Pd(NH₃)₄(NO₃)₂] due to a strong electrostatic adsorption effect at high pH, whereas Pd particles in [Pd(NO₃)₂]-derived catalysts are larger (>10 nm) diameter. The latter observation correlates with the presence of PdO crystallites in these catalysts after calcination, as evidenced by Raman spectroscopy. Varying degrees of Pd-Re interaction in the reduced catalysts are evidenced by EXAFS spectroscopy, STEM-EDX and CO diffuse reflectance infrared Fourier transform spectroscopy. A novel PdRe (1:2 atomic ratio) catalyst comprising Pd clusters in intimate contact with Re-rich nanoparticles (~2 nm diameter) was prepared by direct reduction of the double complex salt (DCS), [Pd(NH₃)₄][ReO₄]₂, deposited on γ -Al₂O₃. This catalyst

exhibits higher FAL and furfural turnover frequencies (TOFs) than any other PdRe/Al₂O₃ catalyst investigated. Calcination of the DCS deposited on γ -Al₂O₃ results in segregation of the metals accompanied by substantial Pd sintering; this catalyst (after reduction) gave a much lower furfural hydrogenation rate (and TOF) than that derived from the DCS without calcination.

© Copyright 2015 Simon Thompson

All Rights Reserved

Palladium-Rhenium Catalysts for Production of Chemicals and Fuels from Biomass

by
Simon Thomas Thompson

A dissertation submitted to the Graduate Faculty of
North Carolina State University
in partial fulfillment of the
requirements for the degree of
Doctor of Philosophy

Chemical Engineering

Raleigh, North Carolina

2015

APPROVED BY:

H. Henry Lamb
Committee Chair

Phillip R. Westmoreland

Fanxing Li

Jerry Whitten

DEDICATION

To my parents, for their hard work and deep interest in my well-being and development.

BIOGRAPHY

Simon Thompson was born in Charlotte, NC, and raised in nearby Monroe. He grew up in an atmosphere that encouraged learning: his parents and several of his aunt and uncles were teachers. From a young age, his parents encouraged his interest in science and the natural world: from gardening and horticulture, to collecting rocks and minerals, to helping catch bugs, always supplementing these activities with books and museum visits. After developing a passion for chemistry in high school, Simon attended the School of Engineering and Applied Science at Columbia University, where he received a B.S. in Chemical Engineering. He returned to his native state in 2010 to attend North Carolina State University, and he was pleased to welcome his brother, Ethan, to Raleigh when he also enrolled in 2013. During his tenure in graduate school, Simon cultivated many interests outside of research, most notably training for marathons and triathlons, playing guitar in a band with classmates, astronomy, genealogy, and Civil War history.

ACKNOWLEDGEMENTS

Hydrodeoxygenation work was supported by the Department of Energy under Award Number DE-FG36-08GO88053. I am grateful to ExxonMobil for use of Beamline X10C and to the Naval Research Laboratory for use of Beamline X11A at the National Synchrotron Light Source, Brookhaven National Laboratory, supported by the Department of Energy.

Selective hydrogenation work was funded by Eastman Chemical Company through the Center of Excellence here at NCSU. I am grateful to Eastman for all my ICP-OES analysis as well. X-ray absorption spectroscopy on PdRe/Al₂O₃ catalysts was performed at the Advanced Photon Source, a U.S. Department of Energy (DOE) Office of Science User Facility operated for the DOE Office of Science by Argonne National Laboratory under Contract No. DE-AC02-06CH11357. I gratefully acknowledge the loan of EXAFS equipment from Dr. Jeffrey Miller, and the assistance of Dr. Joshua Wright and Dr. John Katsoudas in operating beamline MR-CAT-10BM. I would also like to thank Dr. Bruce Ravel, Dr. Matthew Newville and Dr. Shelly Kelly for their willingness to freely share their knowledge of XAFS. I would also like to acknowledge the Analytical Instrumentation Facility at NCSU, which is supported by the State of North Carolina and the National Science Foundation, and, in particular, Dr. Xiahan Sang for assistance with STEM-EDX.

On a personal note, I would like to thank my labmates, Dr. Taylor Schulz, Dr. Keyi Sun, Dr. Adria Wilson and Dr. M. Jason Kelly for their support and cooperation. I also appreciate the camaraderie of my fellow classmates, in particular Dr. Dennis McOwen and Patrick Fahey, and to my triathlon training buddies, Cameron Cook and Edwin Walker.

Finally, I owe a debt of gratitude to my girlfriend, Natalia Escobar, for her support and friendship throughout these years.

TABLE OF CONTENTS

LIST OF TABLES	viii
LIST OF FIGURES	ix
CHAPTER 1: HYDRODEOXYGENATION OF GUAIACOL TO C6 HYDROCARBONS OVER PdRe/C	1
1 Introduction.....	2
2 Experimental	5
3 Results and Discussion	11
4 Conclusions.....	37
5 Acknowledgements.....	38
CHAPTER 2: PALLADIUM-RHENIUM CATALYSTS FOR SELECTIVE HYDROGENATION OF FURFURAL.....	43
1 Introduction.....	44
2 Experimental	47
3 Results and Discussion	54
4 Conclusions.....	89
5 Acknowledgements.....	90
References.....	91
CHAPTER 3: PREPARATION OF PdRe/Al ₂ O ₃ CATALYSTS: CHARACTERIZATION BY RAMAN, TPR, XAFS AND STEM-EDX.....	95
1 Introduction.....	96
2 Experimental	101
3 Results and Discussion	105
4 Conclusions.....	131
5 Acknowledgements.....	133
References.....	134
CHAPTER 4: PALLADIUM-RHENIUM SELECTIVE HYDROGENATION CATALYSTS PREPARED FROM A PdRe ₂ DOUBLE COMPLEX SALT	138
1 Introduction.....	139
2 Experimental	140
3 Results and Discussion	143
4 Conclusions.....	164
5 Acknowledgements.....	164

References.....	166
CHAPTER 5: SUMMARY AND OUTLOOK.....	169
1 Bimetallic Synergy in PdRe Catalysts	170
2 Future Work.....	177
References.....	180

LIST OF TABLES

Chapter 1

Table 1. Metal loadings and CO chemisorption results	14
Table 2. EXAFS spectroscopy fitting parameters.....	17
Table 3. Guaiacol conversion and C selectivity at 260°C	25
Table 4. Guaiacol conversion and C selectivity to products at 300°C	26
Table 5. Anisole conversion and C selectivity to products at 300°C	30
Table 6. Product formation rates and TOFs at 300°C.....	35

Chapter 2

Table 1. Catalyst preparation and metal content from ICP-OES.....	48
Table 2. BET surface areas for Al ₂ O ₃ supports and PdRe/Al ₂ O ₃ catalysts	50
Table 3. Volumetric CO and H ₂ chemisorption results	58
Table 4. Furfural TOFs (min ⁻¹) at 150°C.....	63
Table 5. TPHD results for H/Pd stoichiometry.....	70
Table 6. EXAFS fitting parameters	75

Chapter 3

Table 1. Summary of supported PdRe catalyst preparation.....	99
Table 2. Characterization of γ -Al ₂ O ₃ support by N ₂ physisorption and ICP-OES	102
Table 3. Catalyst preparation and metal content from ICP-OES.....	102
Table 4. CO and H ₂ chemisorption results.....	116
Table 5. EXAFS fitting parameters for PdRe/Al ₂ O ₃ catalysts.....	121
Table 6. Furfural TOFs at 150°C	131

Chapter 4

Table 1. ICP-OES analysis of PdRe/Al ₂ O ₃ catalysts	141
Table 2. CO and H ₂ chemisorption results.....	147
Table 3. H/Pd ratios based on H ₂ evolution in TPHD	152
Table 4. EXAFS fitting parameters for uncalcined DCS-derived catalyst	155
Table 5. Furfural TOFs at 150°C	162

LIST OF FIGURES

Chapter 1

Figure 1. Diagram of continuous-flow packed-bed reactor	8
Figure 2. TPR profiles of Pd/C, Re/C and PdRe/C catalysts after drying in air	12
Figure 3. TPR profiles Pd/C, Re/C and PdRe/C catalysts after ex situ reduction	12
Figure 4. TPHD profiles of Pd/C and PdRe/C catalysts	13
Figure 5. Calibration curve for edge position with Re oxidation state	16
Figure 6. Re L _{III} EXAFS spectra for as-prepared PdRe/C and Re/C catalysts	18
Figure 7. FT magnitudes and fits of in situ reduced and He-purged PdRe/C	19
Figure 8. Fitting of <i>in situ</i> reduced and He-purged PdRe/C	20
Figure 9. STEM images of Re/C catalyst	22
Figure 10. STEM images of PdRe/C catalyst	22
Figure 11. Catalyst behavior with TOS at 300°C	27
Figure 12. Yields of fully deoxygenated products of guaiacol HDO at 300°C	28
Figure 13. Yields of fully deoxygenated products of anisole HDO at 300°C	32
Figure 14. First-order delplots for guaiacol HDO	33
Figure 15. Reaction pathways for guaiacol and anisole over supported noble metal catalysts	34

Chapter 2

Figure 1. TPR profiles of PdRe/Al ₂ O ₃ catalysts	55
Figure 2. TPR profiles of Pd/Al ₂ O ₃ catalysts.....	55
Figure 3. Delplots for furfural conversion at 150°C	61
Figure 4. Furfural reaction pathways over PdRe/Al ₂ O ₃ catalysts.....	62
Figure 5. Product formation rates at 150°C over PdRe/Al ₂ O ₃	63
Figure 6. Furfural hydrogenation results at 150°C vs. H/CO uptake.....	66
Figure 7. CO DRIFT spectra on PdRe/Al ₂ O ₃ catalysts.....	67
Figure 8. TPHD profiles for PdRe/Al ₂ O ₃	69
Figure 9. Re L _{III} XANES results of Re/Al ₂ O ₃ and RePd/Al ₂ O ₃ catalysts	71
Figure 10. EXAFS Fourier tranforms for PdRe/Al ₂ O ₃ catalysts.	73
Figure 11. Theoretical EXAFS Fourier transforms at the Pd K- and Re L _{III} -edge.....	74
Figure 12. TPR profiles of Re/Al ₂ O ₃	76
Figure 13. Data and fitting of 5% Re/Al ₂ O ₃ (H).....	77
Figure 14. Data and fitting of PdRe/Al ₂ O ₃ co.....	78
Figure 15. Data and fitting of PdRe/Al ₂ O ₃ seq. (350)	79
Figure 16. Data and fitting of PdRe(1:2)/Al ₂ O ₃ seq.	80
Figure 17. HAADF-STEM images of Pd/Al ₂ O ₃	83
Figure 18. HAADF-STEM images of Re/Al ₂ O ₃ (H).....	83
Figure 19. Low magnification HAADF-STEM comparison of PdRe/Al ₂ O ₃ catalysts.....	84
Figure 20. STEM images of PdRe/Al ₂ O ₃ co.....	86
Figure 21. STEM-EDX images of Re-Pd ⁰ seq.....	86
Figure 22. STEM images of PdRe/Al ₂ O ₃ seq. (350)	87
Figure 23. STEM images of PdRe/Al ₂ O ₃ seq. (400)	87

Figure 24. STEM-EDX images of a.)PdRe seq. (350) and b.) PdRe seq. (400).....	88
---	----

Chapter 3

Figure 1. Raman spectra of calcined catalysts after exposure to ambient air	107
Figure 2. TPR profiles of PdRe/Al ₂ O ₃ catalysts	109
Figure 3. EXAFS FT magnitudes and fits (<i>k</i> ² -weighting) of "as prepared" Re/Al ₂ O ₃ catalysts	111
Figure 4. EXAFS (<i>k</i> ² -weighting) of Pd ⁰ /Al ₂ O ₃ (B) at room temperature	113
Figure 5. CO DRIFT spectra on PdRe/Al ₂ O ₃ catalysts.....	117
Figure 6. EXAFS (<i>k</i> ² -weighting) of PdRe/Al ₂ O ₃ catalysts.....	120
Figure 7. Low-magnification HAADF-STEM images of PdRe/Al ₂ O ₃ catalysts.....	124
Figure 8. STEM images of PdRe co	125
Figure 9. STEM of Re-Pd ⁰ seq. (B)	126
Figure 10. STEM images of Pd(TA)Re seq.....	128
Figure 11. Product formation rates at 150°C.	130

Chapter 4

Figure 1. FT-IR spectra of Pd(NH ₃) ₄ (ReO ₄) ₂ and reactants used in its preparation	142
Figure 2. Raman spectra of Pd(NH ₃) ₄ (ReO ₄) ₂ and reactants used in its preparation.....	142
Figure 3. TPR of PdRe/Al ₂ O ₃	144
Figure 4. TGA of the unsupported DCS.	145
Figure 5. CO DRIFT spectra of PdRe/Al ₂ O ₃	148
Figure 6. CO DRIFTS on 3% Pd/Al ₂ O ₃	150
Figure 7. TPHD of PdRe/Al ₂ O ₃	152
Figure 8. EXAFS spectra of PdRe/Al ₂ O ₃ DCS.....	153
Figure 9. PdRe/Al ₂ O ₃ DCS EXAFS Fourier transform fits	154
Figure 10. STEM images of PdRe/Al ₂ O ₃ DCS.....	158
Figure 11. STEM images of calcined DCS -prepared catalyst	160
Figure 12. Furfural consumption rate over Al ₂ O ₃ -supported catalysts.....	161

Chapter 5

Figure 1. Production rates versus furfural consumption rate.....	173
Figure 2. Furfural TOF versus the ratio of strongly adsorbed H/CO in chemisorption.....	177
Figure 3. Schematic diagram of bench-scale apparatus for continuous biomass pyrolysis and catalytic upgrading.....	178

CHAPTER 1: HYDRODEOXYGENATION OF GUAIACOL TO C6

HYDROCARBONS OVER PdRe/C

Abstract

Guaiacol hydrodeoxygenation (HDO) with high selectivity to benzene and cyclohexane is demonstrated using a PdRe/C catalyst. Yields of benzene and cyclohexane, over PdRe/C at atmospheric pressure and 300°C at 1 atm are much greater than over Pd/C, Re/C or Ru/C (at comparable conversions). These yields increase with increasing H₂ pressure over PdRe/C, Re/C and Ru/C, but not Pd/C. Production rates of phenol, anisole, benzene and cyclohexane from differential conversion measurements are much higher over PdRe/C than Pd/C. Similar rates of production of phenol and methanol over Pd/C indicate demethoxylation via scission of the phenyl C-O bond; concomitant production of methane and phenol indicates facile methyl C-O bond scission over Re/C. The bimetallic catalyst exhibits the activity of both metals, with higher rates of demethoxylation than Pd/C. The same C-O bond scission selectivities were observed in anisole HDO experiments. Fitting of extended x-ray absorption fine structure (EXAFS) spectra using theory yields a Pd-Re coordination number of 1.5, suggesting intimate contact of the two metals. This finding is in agreement with scanning-transmission electron microscopy (STEM) with energy dispersive x-ray (EDX) imaging of the catalyst, which shows Re⁰ clusters on the surface of large Pd particles (10-50 nm). Surface sites comprising metallic Re and Pd are proposed to be responsible for the enhanced HDO performance of PdRe/C.

1 Introduction

Modern transportation depends heavily on liquid hydrocarbon fuels, nearly all of which come from petroleum sources. Concerns over the limited supply of petroleum, national security issues and global warming have made the need for alternative fuels clear [1]. Liquid transportation fuels made from biomass processing are among the most promising options; biomass is renewable and fuels created from it are, in principle, carbon-neutral [2]. One viable approach to generating biofuels is through the catalytic upgrading of fast pyrolysis oil, "bio-oil." Bio-oil is unsuitable for use as a fuel due to its low energy density, low pH and limited shelf-life—all due to the high content of oxygenated organics, such as organic acids, ketones and aldehydes [1-4]. Work on hydrodeoxygenation over supported metal catalysts began with conventional hydrotreating catalysts, sulfided CoMo- and NiMo/Al₂O₃ [5, 6]; however, these were not ideal, as leaching of sulfur, coking and acid attack on the Al₂O₃ support led to deactivation [3, 7, 8]. Recently, carbon-supported noble metal catalysts, specifically Pd/C and Ru/C, were shown to be the most promising candidates maximizing oil yield with the lowest oxygen content of bio-oil samples as compared to CoMoS- and NiMoS/Al₂O₃ and to noble metals on other supports (TiO₂, Al₂O₃, SiO₂) [7].

Guaiacol is a model compound for lignin fast-pyrolysis products, i.e., phenolics such as eugenol, vanillin and syringol, that make up a significant fraction of bio-oil [9, 10]. The proportion of phenolics in treated bio-oil has been shown to increase as compared to untreated oil due to the further degradation of lignin pyrolysis products, thus it is important to ensure catalytic activity in HDO of phenolics [11]. Recently, aqueous phase deoxygenation of guaiacol, catechol and phenol over Ni/HZSM-5 has been demonstrated [12]. Guaiacol

HDO has also been performed on several supported noble metal catalysts, such as Pd- and Ru/C [11, 13, 14], Pt-, Pd- and Rh/ZrO₂ [8, 15], Pt/Al₂O₃[16] and Pt/HY [17]. Several commercial noble metal catalysts (Pt-, Pd-, Rh- and Ru/C) were screened by Gao, et al., in guaiacol HDO at 300°C and ambient pressure [18]. Of these catalysts, Pt/C was found to have the highest deoxygenation activity and slowest deactivation, though in all cases, the main product was phenol. Bimetallic candidates have been investigated as well and have typically improved on the activity of the monometallic analogues [19, 20]. Sun, et al., have demonstrated that PdFe/C has enhanced activity and a higher yield of benzene as compared to Pd/C and Fe/C [20]. A well-chosen second metal can thus increase yields of fully deoxygenated products, i.e., benzene and cyclohexane, and minimize ring saturation—undesirable due to the potential use of H₂ as a fuel itself.

Enhancement of deoxygenation activity is hypothesized to be achieved with a more oxophilic second metal, one which can break C-O bonds that Pd alone cannot; e.g., the phenyl C-O bond in phenol. Recently, a PtRe/C catalyst was demonstrated to increase hydrogenolysis of glycerol [21-23]. The addition of Re was suggested to lower CO-surface bond energy, slowing CO poisoning of the catalyst and increasing water-gas shift activity [22]. Also, stronger coordination of hydroxyls and other oxygenated functional groups to the surface of the metals increases activity—this may be an effective strategy to increase HDO activity. The Tomishige group has studied several Group VIII-Re bimetallic catalysts [24-27] for CO oxidation [27], hydrogenolysis of tetrahydrofurfuryl alcohol to 1,5-pentanediol [28], selective hydrogenation of fatty acids (Takeda). In each case, they conclude that, after reduction, several Re species were present, including Re metal, low valence ReO_x clusters on

the surface of Rh, Pd or Pt, and clusters on the support. Their results suggest that the active species is the ReO_x (Re oxidation state +2.7) clusters which are in intimate contact with the Group VIII metal [24, 27].

Bulk phase diagrams indicate a large miscibility gap for PdRe alloys; however, previous investigations have suggested that incipient wetness impregnation followed by calcination on Al_2O_3 or SiO_2 supports can produce Pd-Re alloy particles and, furthermore, that alloying is responsible for modified activity, e.g., [25, 29-32]. For example, Malinowski, et al. [29], and likewise Ziemecki, et al. [33], attribute decreased H:Pd ratio during temperature-programmed hydride decomposition (TPHD) to alloying of Pd and Re. X-ray diffraction (XRD) results indicate suppression of PdH_x formation in Pd black impregnated with Re_2O_7 due to Pd-Re alloying. This conclusion is extended to a PdRe/ Al_2O_3 catalyst in which hydride formation is almost completely suppressed [33].

Herein, the guaiacol and anisole HDO performance of PdRe/C is shown to be superior to Pd/C, Re/C or Ru/C. Higher yields of benzene and cyclohexane are demonstrated with decreased gas yields as compared to Re/C and Ru/C. Guaiacol HDO under differential conversion conditions suggests phenol, anisole, 2-methoxycyclohexanol, and catechol as primary products over all catalysts, while benzene, cyclohexane and cyclohexanol are formed upon multiple adsorption events (secondary products). The bimetallic catalyst benefits from the high initial activity of Re/C, but does not deactivate rapidly, as Re/C does. Characterization of these catalysts by temperature-programmed reduction (TPR) suggests proximity of Pd and Re within the catalysts. Theoretical fitting of extended x-ray absorption fine structure (EXAFS) spectra are consistent with limited Pd-Re interaction; however, this

interaction appears to be limited to the surface of Pd particles from scanning transmission emission microscopy with energy-dispersive x-ray spectroscopy (STEM-EDX) images and palladium hydride formation, apparent in temperature-programmed hydride decomposition (TPHD) and EXAFS spectroscopy. Superficial Re species on Pd particles create favorable sites for complete deoxygenation of guaiacol and anisole.

2 Experimental

2.1 Catalyst preparation

PdRe catalysts and monometallic analogues were prepared by incipient wetness impregnation of Norit SX-1G activated carbon (880 m²/g, BET surface area) using Pd(NO₃)₂·H₂O (99.9% Pd basis from Strem) and a 76.5 wt% solution of HReO₄ (99.99% Re from Acros Organics). These catalysts were made using a solution of the proper precursor(s) that was added to the carbon support to achieve incipient wetness. The resultant paste was dried at 110°C in air for several days, and the powder stored in a desiccator until use. Commercial catalysts, 5% Pd/C Evonik E117, denoted as Pd/C (E), and 5% Ru/C from Alfa Aesar, were used as received. Metal loadings determined by inductively coupled plasma – optical emission spectrum (ICP-OES) are listed in Table 1.

2.2 TPR and TPHD

TPR measurements were performed using a Micromeritics 2920 AutoChem II. After purging the sample tube with He (UHP from National Welders), the sample was exposed to 5% H₂/Ar (Certified, Machine and Welding Co.) and heated at 10°C/min to 400°C, held for 1 h, and then cooled to ambient. A second ramp to 400°C in 5% H₂/Ar was used to characterize

the Pd β -hydride phase via TPHD. The H₂ uptake (1st ramp)/desorption (2nd ramp) was monitored by a TCD that was calibrated using a AgO standard.

2.4 CO Chemisorption

CO chemisorption measurements were made using a Micromeritics 2020 ASAP instrument. Catalysts were initially evacuated for an hour at 100C, then reduced in H₂ (research grade from National Welders) at either 300°C or 400°C for 1 h, and evacuated at that temperature for 4 h. After a leak test, uptake of pure CO (Research grade from National Welders) was measured at 35°C. The sample was evacuated to remove the weakly bound CO, and then the analysis was repeated. The difference between these two isotherms corresponds to strongly bound CO, representative of surface sites. Stoichiometric factors of 2 Pd/CO and 1 Re/CO were used.

2.5 X-ray Absorption Fine Structure (XAFS) Spectroscopy

XAFS spectra at the Pd K (24350 eV) and Re L_{III} edges (10535 eV) were recorded at the National Synchrotron Light Source at Brookhaven National Lab using beam lines X-10C and X-11A. Catalysts were reduced in situ in 5% H₂/He (Airgas, certified) in an *in situ* cell with beryllium windows [34]. After cooling to room temperature, the cell was purged for 30 minutes in He (UHP, Airgas) in order to decompose the β -PdH_x phase. X-ray absorption near-edge structure (XANES) spectra of Re standards were measured to enable quantitative analysis of PdRe/C and Re/C catalysts. Samples of each Re standard were mixed with boron nitride (99.5% from Fisher), pressed into a sample holder, and scanned in transmission mode. The X-ray monochromator comprised Si (311) crystals. Edge shifts were determined using Re metal powder in the reference position.

The data were processed using Athena (part of the IFEFFIT package [35]) and fit using Artemis [36]. FEFF references were generated using ATOMS [37] and relevant crystallographic data for NH_4ReO_4 [38], Pd and Re [39]. Amplitude-reduction factors, S_0^2 for Pd and Re, 0.78 and 0.71, respectively, were determined from fitting Pd foil and Re metal powder. A heterometallic bond reference (Pd-Re and Re-Pd) was created by replacing half of the nearest neighbors with atoms of the other metal at a distance equal to the average bond lengths the two metals within an fcc structure. The fit of PdRe/C after reduction was a simultaneous fit of both edges using certain logical combinations of variables in order to minimize the number of free parameters. The heterometallic paths were forced to have the same coordination number (N) and path length (r). Debye-Waller factors (σ^2) were assigned for two homometallic bonds, one for the heterometallic bond, and the Re-O bond. Also, the energy shifts, E_0 , for all paths of each absorber were given the same value.

2.6 High resolution-STEM with EDX spectroscopy

Scanning transmission electron microscopy was performed on an aberration-corrected FEI Titan 80-300 electron microscope using the high-angle annular dark field detector equipped with SuperX EDS system comprising four Bruker silicon drift detectors. Samples were reduced *ex situ* at 400°C and handled under N_2 ; however, brief exposure to ambient air was unavoidable when inserting the sample into the microscope. Grids were prepared by dipping 300-mesh carbon-coated copper grids (Ted Pella) into the dry catalyst powder.

2.7 Catalytic activity measurements

Catalyst testing was performed using a continuous-flow packed bed reactor consisting of a catalyst bed held in place by quartz wool within at ½-in. 316 stainless steel tube (Figure

1). The reactor tube was positioned vertically in a Lindberg Blue-M furnace. Gas and liquid were fed from the top after passing through a 6-ft evaporation coil of ¼-in. stainless steel tubing. A back-pressure regulator (Tescom) downstream allowed pressure control. Guaiacol (TCI and Sigma) and anisole (TCI) were fed via an Isco 260D syringe pump and evaporated into a carrier gas stream. Ultra-high purity H₂ and He (National Welders) were metered via mass flow controllers (Brooks). All lines upstream of the condenser were wrapped with heating tape and held at 200°C.

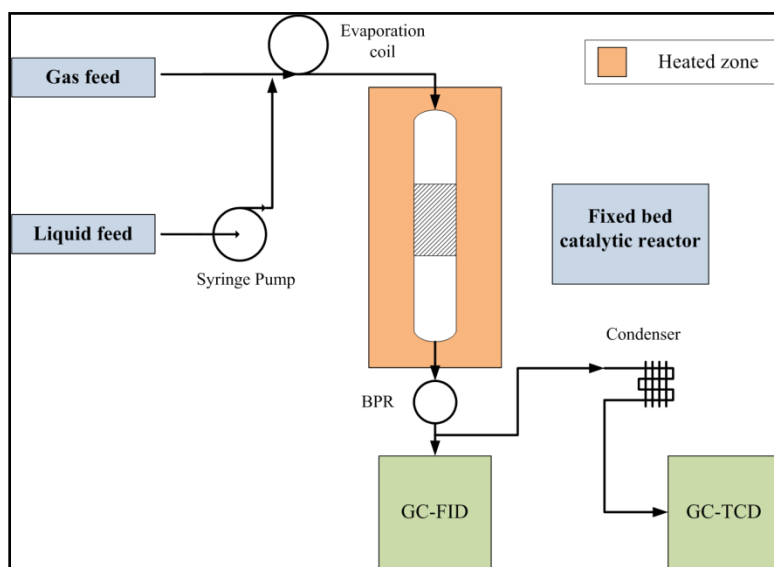


Figure 1. Diagram of continuous-flow packed-bed reactor

On-line monitoring was performed using two on-line gas chromatographs (GCs). A Shimadzu 2010 GC with a flame ionization detector (FID), and an Alltech 30 m x 0.53 mm ID EconoCap-1 column was used to separate and quantify organics in the reactor effluent stream. An automated sampling valve (Valco), held at 300°C, was located upstream of the

condenser. The split ratio was 10 and the GC column program was a 5 min. hold at 30°C, followed by a 30°C/min ramp to 120°C and a 45°C/min ramp from 120°C to 275°C, which was then held for 5 min. Product peaks were identified and calibrated by dissolving known standards in MeOH and injecting them onto the column. Permanent gases, CO and CO₂, were monitored using a SRI 8610C GC with a thermal conductivity detector (TCD) and a ShinCarbon ST100 (2 m x 1.0 mm ID) column (Restek). A gas mixture (5% H₂, 5% CO, 5% CO₂, 1% CH₄, balance He, National Welders) was used to calibrate the GC-TCD.

Guaiacol/anisole conversion was determined by subtracting the concentration of guaiacol in the effluent from GC peak area and response factor from the feed rate of reactant:

$$\text{Guaiacol/Anisole Conversion}(\%) = 100\% \left(1 - \frac{A_x RF_x \dot{V}}{\dot{F}_x} \right)$$

where A is GC peak area, RF is the response factor [concentration/area], V is gas flow rate, F is the feed rate of guaiacol, and the x subscript denotes the respective reactant. In differential conversion experiments, the conversion was calculated by the sum of the carbon yields of products, defined as:

$$C \text{ yield } (\%) = \frac{A_y RF_y S_y}{F_x S_x} * 100\%$$

where the y subscript denotes any species observed on the GC and S is the C stoichiometry factor for each compound. Carbon selectivities are the observed carbon content in the products out of the total carbon in the products:

$$C \text{ selectivity } (\%) = \frac{A_y RF_y S_y}{\sum_{\text{all products}} A_y RF_y S_y} * 100\%$$

The mass balance was calculated on a C basis by the sum of C yields (%) for all observed GC peaks.

Nine C₆-C₇ products were identified and calibrated; two more have not been identified. These unknowns are likely partially saturated products, i.e., substituted cyclohexenes, and are referred to by their retention times: RT9.718 and RT7.787. Several candidate compounds were ruled out, including 1,2-dihydroxycyclohexane, toluene, cresols and veratrole. Other low-molecular-weight products were formed, foremost by Ru/C, but they were not identified. The carbon content of these low-molecular-weight products was estimated from calibrations of the other products. Peaks for cyclohexanol and cyclohexanone co-eluted, thus they could not be separated, and they are henceforth accounted for by cyclohexanol alone, assuming complete saturation of the molecule.

Typically, 0.5 g of catalyst powder was loaded on top of a quartz wool plug, and a thermocouple was inserted into the bed to monitor catalyst temperature. Catalysts were reduced in situ using flowing H₂ (100 sccm) for 1 h at 300 or 400°C, and then cooled to a reaction temperature of 260 or 300°C. The H₂:reactant molar ratio was held constant (~60:1), unless otherwise noted, and the typical weight hourly space velocity (WHSV) was ~1 h⁻¹. Tests with an empty tube showed negligible thermal decomposition of guaiacol and anisole under these conditions..

Differential conversion experiments were performed to elucidate primary products and reaction networks. In order to get lower contact times (1/WHSV) while keeping the feed vaporized, less catalyst was used (typically 0.150 g), requiring use of borosilicate glass beads (ChemGlass) to spread the bed across the full cross-section of the tube to prevent channeling. The same reduction procedure was used. A complete reaction data set consisted of a series

of changes in WHSV at constant reactant concentration. The carbon molar balance was closed within 90% or greater.

3 Results and Discussion

3.1 TPR/TPHD

TPR profiles of previously untreated Pd/C (N), Re/C and PdRe/C samples are shown in Figure 2. Prominent hydrogen-consumption features at low temperatures (75-125°C) for Pd/C and PdRe/C are assigned to reductive decomposition of the Pd(NO₃)₂ precursor. Because these catalysts were not calcined prior to reduction, excess H₂ consumption in this region is associated with reduction of nitrogen oxides, as verified by on-line mass spectrometry. The sharp H₂ desorption features at 55°C are assigned to β-PdH decomposition [33]. These features indicate Pd reduction occurred at 35°C before the temperature ramp began, and thus they establish the formation of Pd particles at low temperature prior to reduction of Re. In the absence of Pd, Re reduction begins at ~200°C with a peak reduction temperature of 265°C, as seen in the Re/C TPR profile. Cumulative H₂ uptake during TPR to 400°C indicates an average Re oxidation state of +2.6; the average Re oxidation state after TPR to 800°C is +1.1. In contrast, a significant fraction of the Re in the PdRe/C catalyst is reduced at temperatures below 200°C, although there is a broad TPR peak at 280°C, consistent with reduction of isolated Re species. The lower reduction temperature suggests that Pd catalyzes the reduction of Re, likely via hydrogen spillover from Pd particles. We are unable to estimate the average Re oxidation state after 400°C reduction due the excess H₂ consumption associated with nitrate reduction. TPR of catalysts previously

reduced *ex situ* at 400°C and slowly exposed to air was performed to parallel catalyst pretreatment for XAFS spectroscopy experiments (Figure 3).

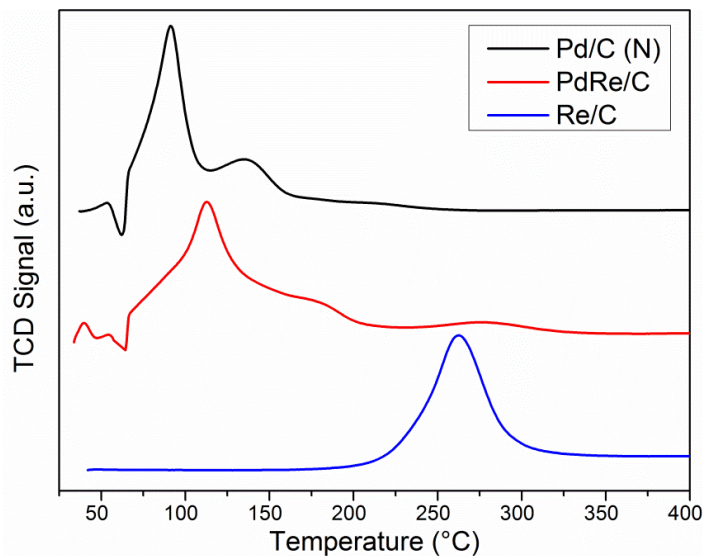


Figure 2. TPR profiles of Pd/C, Re/C and PdRe/C catalysts after drying in air

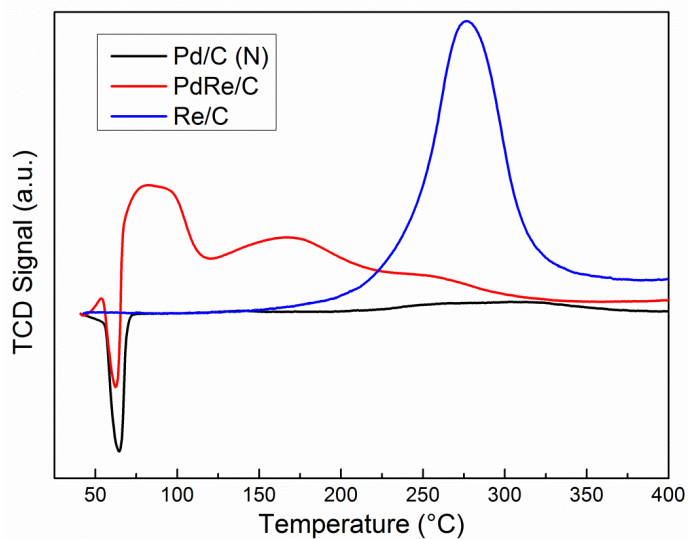


Figure 3. TPR profiles Pd/C, Re/C and PdRe/C catalysts after *ex situ* reduction at 400°C and slow exposure to air at 25°C

After cooling the Pd-containing catalysts in H₂, a second TPR in 5% H₂/Ar allowed the H:Pd ratios for β -PdH_x species to be determined by TPHD (Figure 4). The H:Pd ratio varies in proportion to *fcc* Pd lattice volume, and thus it increases with Pd particle size [40-42]. In the current work, nearly equivalent H:Pd ratios for Pd/C (N) and PdRe/C evidence segregated Pd particles in PdRe/C of approximately the same size as in Pd/C (N); i.e., Re atoms are not integrated into the Pd matrix. The values calculated for H₂ evolution by TPHD are much lower than the bulk value of 0.6-0.7 [40] and, indeed, are smaller than expected for particles <10 nm in diameter.

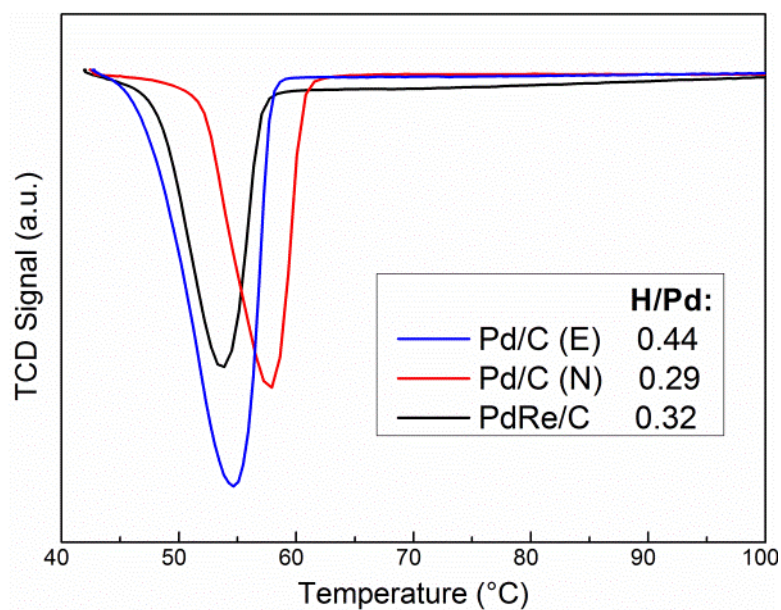


Figure 4. TPHD profiles of Pd/C and PdRe/C catalysts with H/Pd ratios for H₂ evolved

Table 1. Metal loadings and CO chemisorption results; samples previously untreated

Catalyst	Metal loading (wt%)	Reduction temperature (°C)	Total CO adsorbed ($\mu\text{mol CO/g}_{\text{cat}}$)	Strongly bound CO ($\mu\text{mol CO/g}_{\text{cat}}$)	Dispersion (%)*
Samples previously unreduced					
Pd/C (E)	4.8% Pd	300	87.0	39.3	17
Pd/C (N)	4.1% Pd	300	65.2	39.3	20
		400	28.1	6.7	3.5
Re/C	7.6% Re	400	259	222	54
PdRe/C	3.9% Pd, 7.5% Re	300	285	217	42
		400	286	224	43
Ru/C	4.6% Ru	400	150	97.8	22
Following ex situ reduction at 400°C; in situ reduction temperature given					
Pd/C (N)	4.1% Pd	300	61.6	24.6	13
		400	29.0	4.0	2.1
Re/C	7.6% Re	300	191	134	30
		400	204	147	43
PdRe/C	3.9% Pd, 7.5% Re	300	156	123	26
		400	213	178	28

* Stoichiometry factors: 0.5 CO/Pd, 1 CO/Re, and 1 CO/Ru

3.2 CO chemisorption

Metal loadings and CO chemisorption results for previously unreduced catalysts are given in Table 1. Metal dispersions were determined by CO chemisorption using stoichiometry factors of 2 Pd/CO [43], 1 Re/CO [44] and 1 Ru/CO [45]. Pd/C (N) and Pd/C (E) have similar dispersions when reduced at 300°C; *in situ* reduction of Pd/C (N) at 400°C results in a very low dispersion. In contrast, the apparent dispersion of Re/C increases with 400°C *in situ* reduction, which results from increased Re reduction, as seen in Figure 2. Reduction temperature does not change CO uptake on PdRe/C, probably due to the opposing effects of decreased Pd dispersion and increased reduction of Re or to inhibition of Pd

sintering on carbon by Re. A large fraction of CO adsorbed on Re/C is bound strongly; PdRe/C has an intermediate ratio of strongly bound CO to total CO. CO chemisorption results for catalysts after *ex situ* reduction at 400°C and slow air exposure are also given in Table 1. Similar trends are observed with composition and reduction temperature; however, the values are 10-30% lower than after *in situ* reduction at the same temperature.

3.3 XAFS spectroscopy

Re L_{III} edge shifts were determined from the XANES spectra of model compounds representing different Re oxidation states: Re metal powder, ReO₂, ReO₃, Re₂O₇ and NH₄ReO₇. A calibration curve was constructed so that the average oxidation states of Re in Re/C and PdRe/C catalysts under different conditions could be determined (Figure 5).

Despite prior *ex situ* reduction, Re in Re/C is re-oxidized fully to Re⁷⁺ by exposure to air, as evidenced by an edge shift of +4 eV. This agrees with TPR of Re/C after *ex situ* reduction (Figure 3). After subsequent reduction in the XAFS cell at 400°C, the edge shift of Re/C indicates an average Re oxidation state of +2.3. An equivalent oxidation state was obtained from H₂ uptake by Re/C up to 400°C in TPR. The average Re oxidation for PdRe/C after *in situ* reduction at 300°C is +2.6. Thus, the presence of Pd does not significantly alter the final oxidation state of Re in this catalyst; however, Pd does lower the reduction temperature.

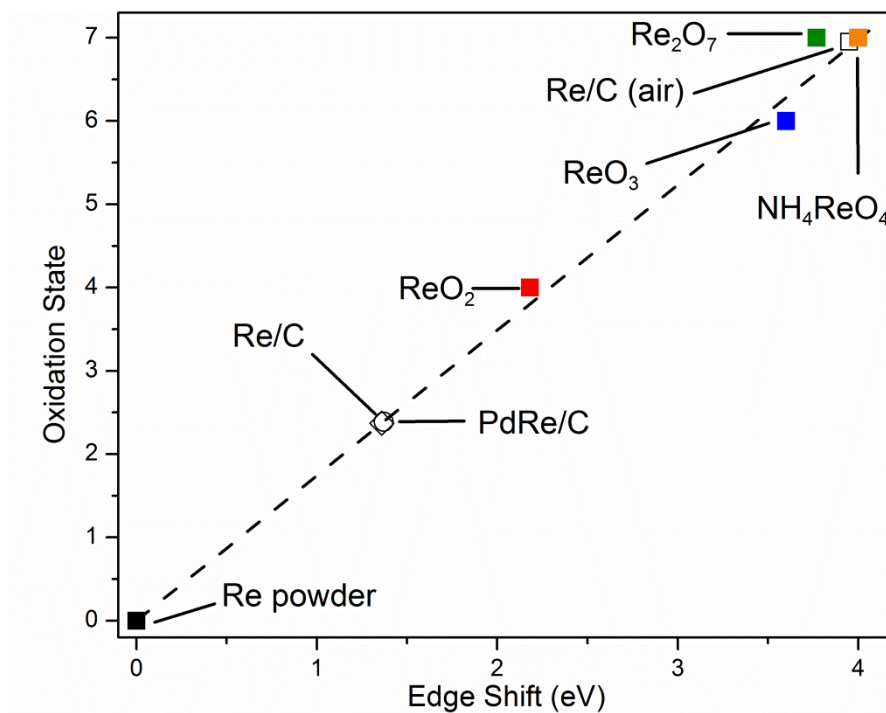


Figure 5. Calibration curve for edge position with Re oxidation state

The first-shell fitting results are given in Table 2 for Pd/C (E) after reduction at 300°C and for Pd/C (N) after reduction at 400°C. The Pd-Pd coordination number (CN) evidences large Pd particles in each catalyst, in general agreement with the low dispersion from CO chemisorption. As the first-shell CN approaches 12 for *fcc* metals, this parameter becomes insensitive to metal particle size because it changes only incrementally as particle size grows exponentially [42]. The longer Pd-Pd distances and higher Debye-Waller factors (σ^2) for Pd/C catalysts under H₂ are explained by β -PdH_x formation [42]. The Pd hydride was decomposed by purging in He at 100°C, as indicated by the reduction in Pd-Pd distance to 2.74-2.75 Å (equivalent to the bulk 2.75 Å distance) with a concomitant decrease in disorder.

Table 2. EXAFS spectroscopy fitting parameters

Treatment	Path*	N	R (Å)	σ^2 (10^{-3} Å ²)	ΔE_0 (eV)	R-value
Pd/C (E)						
Reduced 300°C, H ₂	Pd-Pd	11.1 ± 0.7	2.82 ± 0.01	9.2 ± 0.5	-0.3 ± 0.4	0.006
He purge	Pd-Pd	11.0 ± 0.5	2.75 ± 0.01	5.9 ± 0.3	-3.2 ± 0.3	0.004
Pd/C (N)						
Reduced 400°C, H ₂	Pd-Pd	11.1 ± 0.7	2.82 ± 0.01	9.1 ± 0.5	-0.3 ± 0.9	0.006
He purge	Pd-Pd	10.8 ± 0.3	2.74 ± 0.01	5.8 ± 0.2	0.0 ± 0.2	0.002
Re/C						
In air	Re-O	4.2 ± 0.3	1.73 ± 0.01	0.6 ± 0.6	10.3 ± 1.4	0.014
Reduced 400°C, He purge	Re-Re	7.2 ± 0.6	2.75 ± 0.01	6.3 ± 0.5	-1.7 ± 1.1	0.007
	Re-O	1.4 ± 0.5	2.02 ± 0.02	4.5 ± 3.3	-1.7 ± 1.1	
PdRe/C						
He purge	Pd-Pd	8.4 ± 1.7	2.74 ± 0.01	5.6 ± 1.2	-1.7 ± 1.5	0.004
	Pd-Re	0.8 ± 0.5	2.70 ± 0.03	3.5 ± 3.0	-1.7 ± 1.5	
	Re-Re	6.4 ± 0.6	2.72 ± 0.02	7.0 (set)	6.0 ± 2.4	0.028
	Re-Pd	0.8 ± 0.5	2.70 ± 0.03	3.7 ± 3.3	6.0 ± 2.4	
	Re-O	1.9 ± 0.3	2.01 ± 0.02	5.0 (set)	6.0 ± 2.4	

*First atom is absorber; second, backscatterer

Pd K-edge fit range: k-space 2.6-13.0 Å⁻¹; R-space 1.0-3.3 Å

Re L_{III}-edge fit range: k-space 3.5-12.8 Å⁻¹; R-space 1.0-3.1 Å

The Re L_{III} EXAFS spectrum of the Re/C catalyst after *ex situ* reduction at 400°C and passivation in air indicates complete oxidation to Re⁷⁺. A high-quality fit (Table 2) was obtained using a single Re-O bond distance of 1.73 Å and coordination number of approximately 4, consistent with structure of perrhenate ion (ReO₄⁻) [38]. A satisfactory fit to the EXAFS spectrum measured after subsequent reduction in the XAFS cell at 400°C was obtained using Re-Re and Re-O contributions. The Re-O bond distance is consistent with a single bond. For example, in the model compound ReO₂ the weighted-average Re-O bond

length in ReO_2 is 2.01 Å [46]. The Re-O Debye-Waller factor of $\sim 0.005 \text{ \AA}^2$ is consistent with higher static disorder. The Re-Re distance is equivalent to the average value in the *hcp* bulk metal. When adjusted for the Re-O contribution (assuming octahedral coordination), the Re-Re CN becomes 9.4, consistent with metallic Re particles approximately 2-3 nm in size. This value is also in reasonable agreement with CO chemisorption results for this catalyst (Table 1).

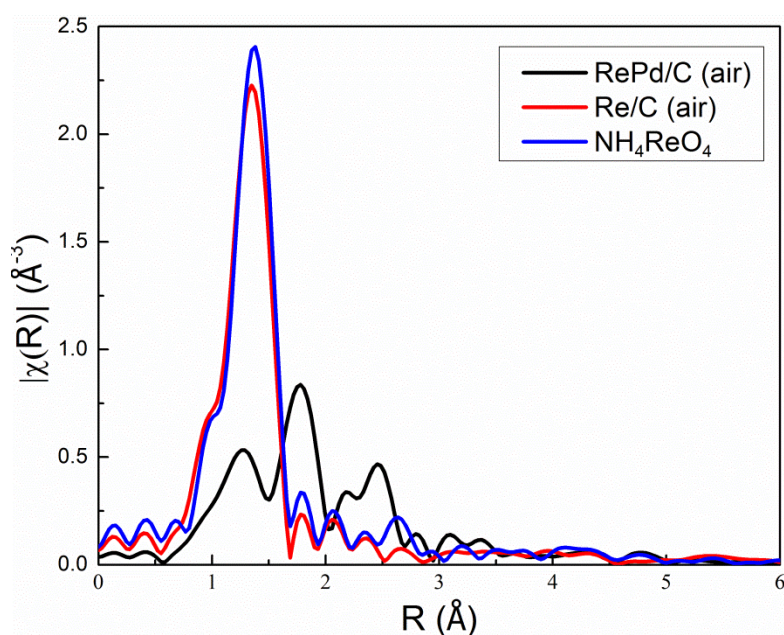


Figure 6. FT magnitudes of Re L_{III} EXAFS spectra for PdRe/C and Re/C catalysts following *ex situ* reduction and exposure to air, and for NH_4ReO_4 standard

The Fourier transform EXAFS spectra of *ex situ* reduced and passivated PdRe/C and Re/C (measured in air) and NH_4ReO_4 are compared in Figure 6. A single Re-O bond distance is observed for Re/C and NH_4ReO_4 consistent with Re^{7+} species (perrhenate ion). In contrast, the EXAFS spectrum of PdRe/C contains two additional contributions from

backscatterers at longer distances, e.g., Re-O of a lower Re oxidation state, and a metal-metal contribution. Due to the complexity of the spectrum, a satisfactory fit was not obtained. At a minimum, however, it is clear that Pd and Re interact sufficiently to prevent all of the Re from oxidizing fully to Re^{7+} after exposure to air.

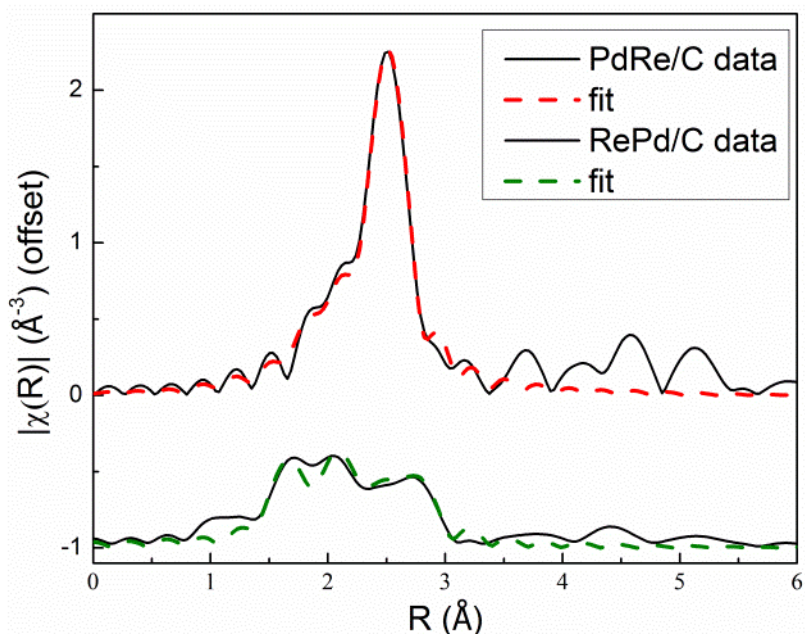


Figure 7. FT magnitudes and fits at Pd (red) and Re (green) edges of in situ reduced and He-purged PdRe/C

Following reduction of PdRe/C at 300°C in the XAFS cell, Re-Re and short Re-O contributions are apparent in the Re L_{III} EXAFS spectrum (Figure 7), but these two paths are not sufficient to achieve an adequate fit. It is clear from the real part of the Fourier transform (Figure 8) that a third path that destructively interferes with the Re-Re contribution is required. Adding a Re-Pd contribution improves the fit markedly, as illustrated in Figure 8. In addition to the overall fit, contributions from each of the three paths used: Re-Re, Re-Pd

and Re-O are shown, and destructive interference between the Re-Re and Re-Pd paths is evident. The Pd edge EXAFS spectrum can be fit satisfactorily with a single Pd-Pd path; however, adding a Pd-Re contribution does improve the fit, albeit marginally. In order to get internally consistent fits at both edges and given the necessity of the Re-Pd path at the Re edge, a Pd-Re path was added. The Pd-Re and Re-Pd coordination numbers were constrained to be equal because Pd and Re are present in a 1:1 molar ratio. The bimetallic fitting constraints put forth by Via, et al. [47], require that the ratio of coordination numbers of each metal about the other at their respective edges should equal the molar ratio of the two metals. The Pd-Re and Re-Pd bond distances and Debye-Waller factors were also set equal.

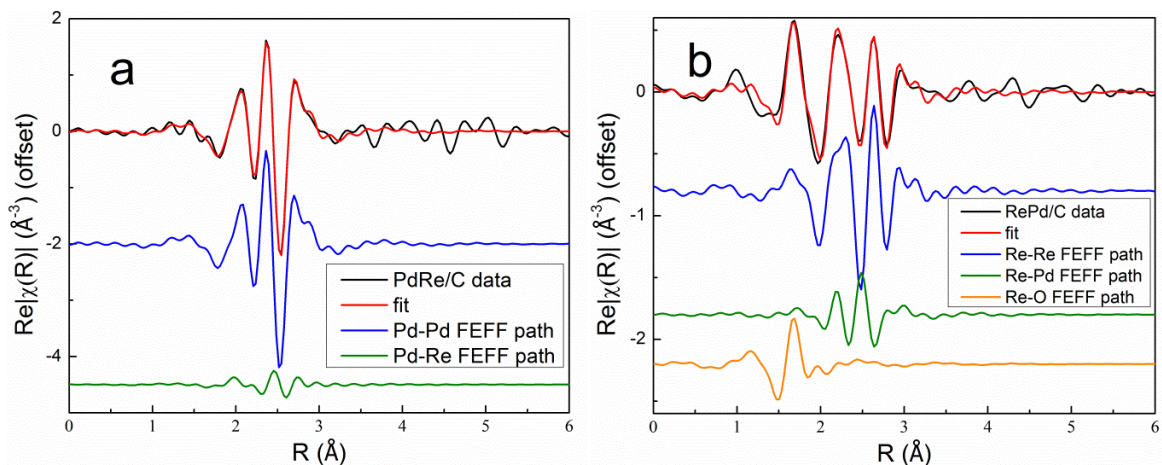


Figure 8. Fitting of *in situ* reduced and He-purged PdRe/C: a.) real portion of FT at Pd edge, b.) real portion of FT at Re edge

The resulting heterometallic coordination number and distance suggest a Pd-Re interaction (Table 2), but not a high degree of mixing, consistent with the large miscibility gap in the PdRe phase diagram [48]. The Pd-Re (Re-Pd) and Re-Re bond distances are short

relative to the interatomic distances in bulk Pd (2.75 Å) and bulk Re (2.74 Å). Contraction of both Pd-Re and Re-Re bonds in PdRe/Al₂O₃ has been reported previously by Meitzner, et al. [32], although the Pd-Re distance (2.67 Å) determined by Meitzner is much shorter than that found in the current work. The Re-O coordination number is slightly greater than for Re/C, and as with Re/C, the bond distance suggests Re⁴⁺ rather than Re⁷⁺.

3.4 STEM-HAADF-EDX analysis

HAADF images of the Re/C catalyst after reduction (Figure 9) reveal small Re particles spread evenly over the activated carbon support. In the region shown in Figure 9a, the largest particles visible are 4-5 nm in size, but most are much smaller. It is clear from the high-magnification HAADF image and EDX map of the highlighted region (Figure 9b-c) that Re particles exist over a 0.5-4 nm size range. CO chemisorption results for Re/C suggest an average Re particle size of about 3 nm, and so the more diffuse Re observed in Figure 9c (which does not correspond to an obvious particle in Figure 9b) may not be metallic and therefore, is not expected to chemisorb CO strongly.

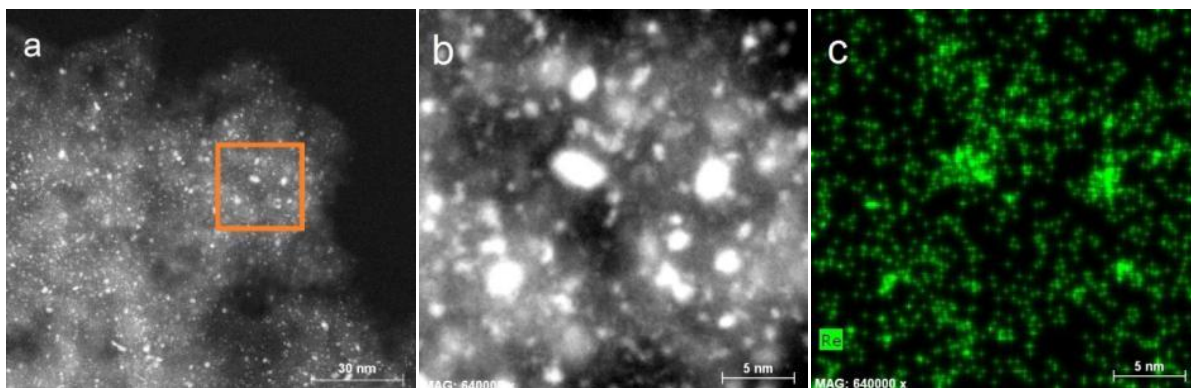


Figure 9. STEM images of Re/C catalyst a.) STEM-HAADF and b.) STEM-HAADF and c.) STEM-EDX of area indicated in a.)

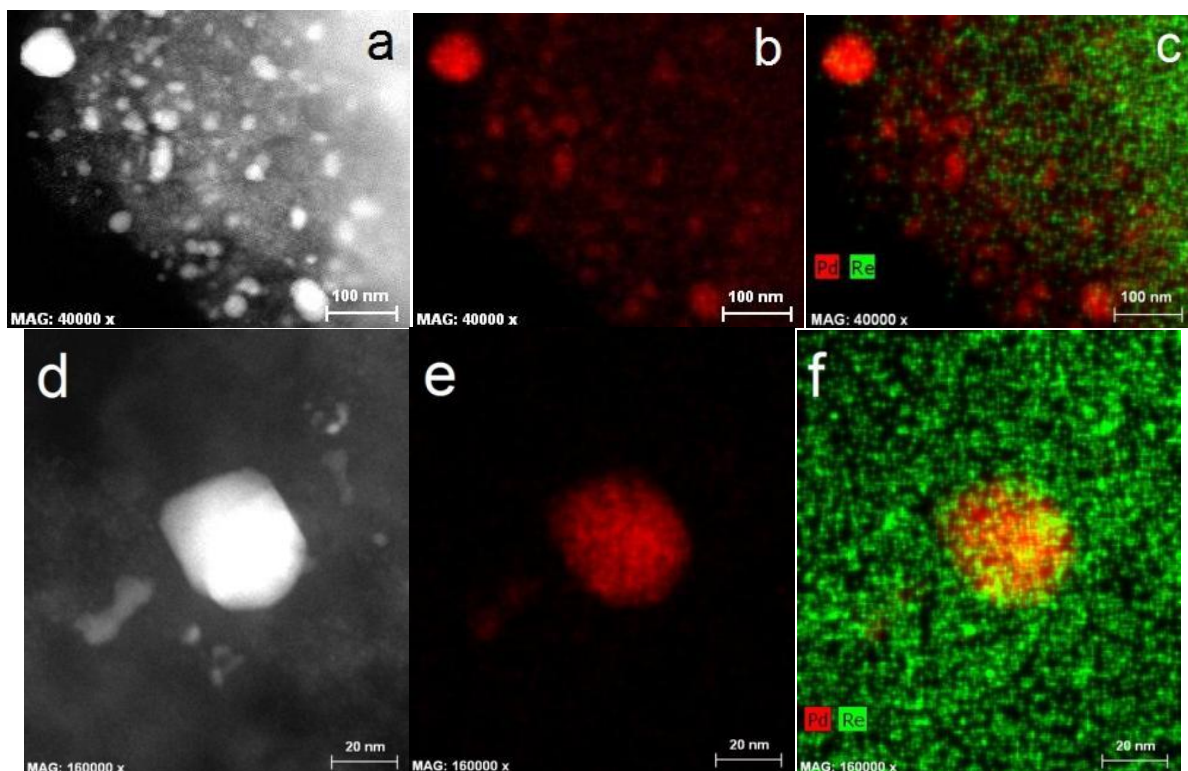


Figure 10. STEM images of PdRe/C catalyst a.) STEM-HAADF b.) Pd STEM-EDX and c.) Pd and Re STEM-EDX; d.), e.), and f.) show analogous images of another region (20 nm scale bar); red – Pd, green – Re, yellow – superposition

HAADF images of the bimetallic catalyst (Figure 10a-c) show mainly large Pd particles, with Re distributed relatively uniformly over the carbon support. Typical Pd particles are 10-30 nm and exist with varying amounts of adjacent Re. Figure 10d-f illustrate a 35-nm Pd particle, with Re scattered over the support and some Re that appears to be on the surface of the Pd particle. Yellow pixels in the EDX map indicate superposition of Pd (red) and Re (green) counts. Figure 10f also shows that Re is spread over the surface, forming smaller clusters of <2 nm. Most Pd particles shown here are <10 nm, but there are many much larger particles, even one approaching 100 nm in diameter in the top left of Figure 10a. In the areas of the catalyst that were examined, no Pd particles smaller than 5 nm were found, indicating that the relatively high CO uptake (and apparent dispersion) for PdRe/C is due to CO adsorption on small Re particles.

3.5 Guaiacol HDO at high conversion

The catalysts were screened initially for guaiacol HDO activity at 260°C. Cyclohexanol and phenol were major products over Pd/C (E), PdRe/C and Ru/C; however, selectivity to ring saturation products, 2-methoxycyclohexanol (2-MCH) and RT9.718, was high, especially over Pd/C (N) (Table 3). Only Pd/C (N) reduced at 300°C, PdRe/C reduced at 400°C, and Ru/C produced any significant benzene and cyclohexane under these conditions. Re/C was not tested under these reaction conditions. Conversion over Pd/C (N) was lower than Pd/C (E), regardless of reduction temperature. The activity of Pd/C (N) declined after reduction at 400°C, consistent with loss of Pd surface area due to sintering (Table 1). Transalkylation reactions were not observed over any of the catalysts studied, nor

were they expected, since the activated carbon support lacks strong acid sites necessary for carbocation formation [16, 17].

Table 3. Guaiacol conversion and C selectivity at 260°C, 1atm, WHSV 1 h⁻¹

	Pd/C (E)		Pd/C (N)		PdRe/C		Ru/C	
Reduction T (°C)	300	300	400	300	400	400		
Conversion	97.9	59.3	21.9	32.3	46.9	55.8		
	% C selectivity							
cyclohexane	0.3	6.1	1.4	0.5	11.3	9.2		
benzene	0.0	1.3	0.1	0.3	8.5	4.9		
phenol	2.4	3.1	2.9	5.3	13.7	36.9		
cyclohexanol	48.7	8.8	2.9	5.0	28.0	29.8		
anisole	0.1	2.1	0.5	3.6	11.7	1.7		
2-MCH	40.7	56.2	47.4	60.1	17.1	4.7		
MCH	0.0	3.4	1.6	0.9	3.3	0.6		
catechol	0.1	2.4	1.5	4.4	0.3	1.2		
RT 7.787	0.8	12.4	1.9	0.0	0.0	1.6		
RT 9.718	2.4	1.0	39.5	12.9	3.0	0.5		
low MW	0.0	0.1	0.0	0.0	0.0	5.0		
MeOH	1.1	2.3	0.2	0.2	0.7	1.7		
CO	3.2	0.3	0.0	1.4	2.0	1.2		
CH ₄	0.0	0.5	0.1	5.3	0.3	1.0		
Yield benzene + cyclohexane	0.3	4.0	0.3	0.3	9.3	7.9		
% C balance closure	103.7	90.7	86.6	90.7	93.4	93.5		

By increasing the reaction temperature to 300°C, extensive guaiacol HDO is achieved over Pd/C (E), PdRe/C and Ru/C at 1 h⁻¹ WHSV. The C₆ and C₇ deoxygenated products and their corresponding C₁ products, methanol, CO and CH₄, indicate different pathways for oxygen removal (Table 4). Pd/C (E) is selective to phenol and cyclohexanol; however, the major product of guaiacol conversion at 300°C over Pd/C (N) is 2-MCH. The 2-MCH yield over Pd/C (N) is much higher after *in situ* reduction at 300°C than 400°C. Most notably, guaiacol HDO over Pd/C (E) does not produce significant yields of benzene and cyclohexane even at high conversion. The dominant HDO pathway over Pd/C is inferred to be demethoxylation, because CO and methanol are the main C₁ products. CO is suggested to

result from methanol decomposition, which has been observed over Group VIII metals [49-51]. Recently, Varma and coworkers have reported similar results for guaiacol HDO over Pd/C at 300°C [18].

Table 4. Guaiacol conversion and C selectivity to products at 300°C, 1 atm, 1 h⁻¹ WHSV

	Pd/C (E)	Pd/C (N)	PdRe/C		Re/C		Ru/C	
Reduction T (°C)	300	300	400	300	400	300	400	400
Conversion	97.8	50.4	24.2	59.0	79.5	29.2	47.5	78.2
C selectivity (%)								
cyclohexane	1.1	3.9	2.1	6.0	19.3	0.5	0.3	7.0
benzene	2.0	1.4	1.0	7.5	45.9	9.8	30.0	10.2
phenol	33.5	6.7	12.5	26.1	13.6	62.1	49.2	38.2
cyclohexanol	52.4	9.7	7.0	21.4	5.2	0.1	0.0	11.5
anisole	0.6	3.9	6.5	12.4	7.6	11.0	8.9	1.8
2-MCH	1.3	51.7	37.0	14.3	1.6	3.9	3.8	1.4
MCH	0.1	2.7	1.6	2.5	0.7	0.0	0.2	0.3
catechol	0.6	4.3	8.8	1.2	0.1	4.3	1.6	1.3
RT 7.787	3.3	11.2	9.5	0.0	0.0	0.0	0.0	2.1
RT 9.718	0.1	2.9	11.7	3.8	0.6	0.0	0.0	0.2
low MW	0.4	0.0	0.2	0.0	0.8	0.1	0.1	16.6
MeOH	1.1	0.4	0.1	0.8	0.3	0.1	0.1	1.4
CO	3.7	0.6	0.6	1.0	4.2	0.0	2.1	4.4
CH ₄	0.3	0.9	1.5	3.0	0.7	8.0	3.7	3.6
Yield benzene + cyclohexane	3.0	2.8	0.7	8.1	51.4	3.0	13.9	13.4
% C balance closure	97.0	87.5	94.1	85.0	105.8	93.6	94.1	105.1

Re/C is selective to guaiacol deoxygenation to phenol at 300°C, irrespective of catalyst reduction conditions; however, reduction at 400°C improves conversion and benzene selectivity when compared to 300°C reduction (Table 4). Selectivity to 2-MCH is very low, and no other ring-saturation products are observed at 300°C. The predominant C₁ product is CH₄. Methane is inferred to result from hydrogenolysis of the O-CH₃ bond to form catechol

[17, 18]. Unlike Pd/C (E), Re/C produces catechol and anisole in significant yields, which suggests that CH₄ results from hydrogenolysis, rather than from hydrogenation of MeOH. Of the catalysts tested, Re/C is most susceptible to deactivation, with a sharp initial decline in conversion in the first few hours on stream, followed by steady deactivation over the course of the next several hours (Figure 11). Full deoxygenation of guaiacol to benzene proceeds over Re/C, but the yield is less than 20%.

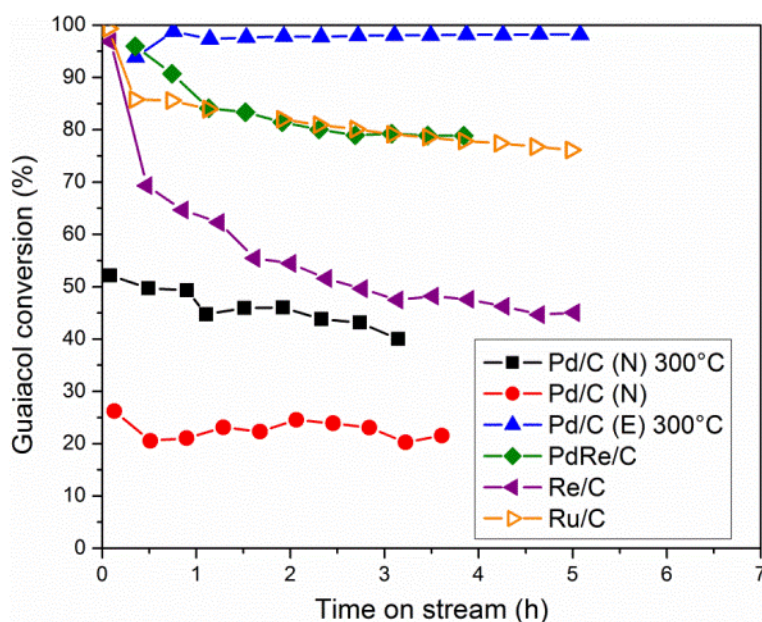


Figure 11. Catalyst behavior with TOS at 300°C, WHSV ~1 h⁻¹, ambient pressure; reduction temperatures indicated in legend, others are 400°C

PdRe/C reduced *in situ* at 400°C has greater guaiacol HDO activity and higher selectivity to fully deoxygenated products than Re/C. In contrast, PdRe/C reduced at 300°C favors 2-MCH and cyclohexanol, performing more like Pd/C (N) than Re/C. The higher reduction temperature increases extent of deoxygenation, as well as increased reduction to

Re⁰. H₂ uptake continues to 400°C in TPR experiments (*vide supra*). It may be assumed from the low reduction temperature for Pd in Pd/C (<100°C) that H₂ uptake between 300-400°C is due to Re reduction in the sample; however, the amount of H₂ consumed between 300-400°C is small in comparison to H₂ consumed below 300°C. The increase in deoxygenation with 400°C reduction may come from increased interaction of the two metals at the higher reduction temperature. PdRe/C also benefits from increased stability over Re/C. After an initial deactivation period, the conversion stabilized at 80% (Figure 11). The yield of benzene and cyclohexane at 300°C and ambient pressure over PdRe/C was higher than any other catalyst tested (Figure 12). PdRe/C combines the selectivity of Re to fully deoxygenated products and the hydrogenation activity of Pd.

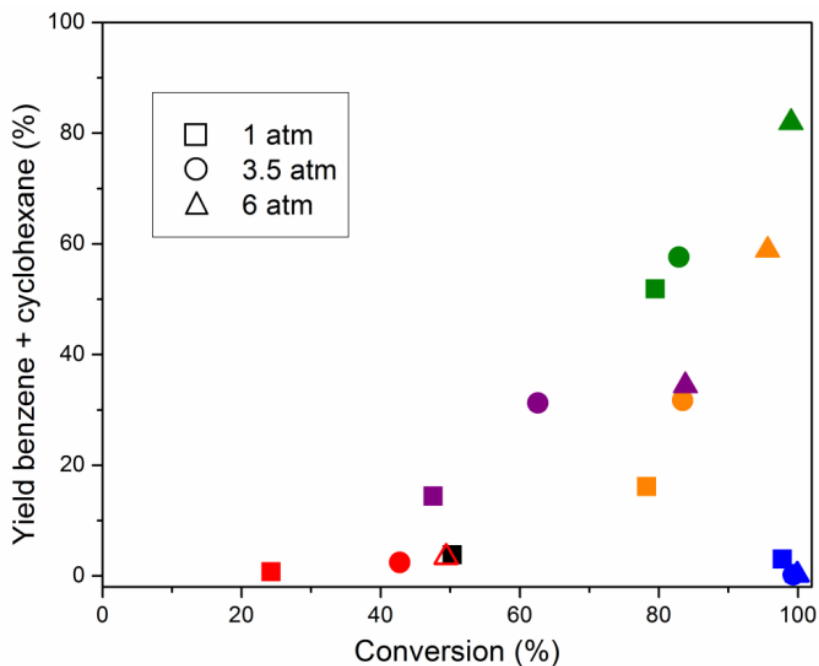


Figure 12. Yields of fully deoxygenated products at 300°C, WSHV ~1 h⁻¹, and 1-6 atm H₂; Pd/C (N – 300°C reduction)- black, Pd/C (N – 400°C reduction) – red, Pd/C (E) – blue, PdRe/C – green, Re/C – purple, Ru/C – orange; all others reduced at 400°C

The performance of PdRe/C is compared to Ru/C, which has been proven effective in HDO of bio-oil samples [13, 52]. Guaiacol conversion over Ru/C is nearly 80% at ambient pressure, equivalent to PdRe/C, albeit with much lower benzene and cyclohexane yields. Under these conditions, Ru/C is selective to phenol. Phenol is inferred to be produced via demethoxylation and via hydrogenolysis followed by catechol HDO, based on the observed selectivities to CO, CH₄ and MeOH (Table 4). High selectivity to phenol and production of CO, CH₄ and MeOH was also observed over Ru/C under similar conditions by Gao, et al. [18]. Although the performance of Ru/C is superior to that of Pd/C, it is less effective at complete HDO of guaiacol to hydrocarbons than PdRe/C. Ru/C is also the only catalyst that produces a substantial yield of low-molecular-weight cracking products.

Operating at higher pressures boosts benzene and cyclohexane yields over Re/C, PdRe/C, and Ru/C; however, operating pressure has little or no effect on the yields of these products over Pd/C (Figure 12). The yield of fully deoxygenated products over PdRe/C and Ru/C increases linearly with pressure. The slope (response to increasing pressure) is greater for Ru/C than PdRe/C. The yield does not increase substantially for Re/C between 3.5 and 6 atm, and this yield maximum over Re/C is due to increased CH₄ production at higher conversion. The Pd/C catalysts exhibit almost no change in fully deoxygenated product yields with increasing pressure; even at nearly 100% conversion, elevating H₂ pressure does not cause HDO to proceed to completion over Pd/C. This finding is in agreement with previous reports on HDO of guaiacol over Pd/C in which Pd is selective to phenol and cyclohexanol at high conversion [18, 20, 53].

3.7 Anisole HDO

Anisole HDO at 300°C was investigated in order to observe catalyst selectivity for phenyl-O-CH₃ bond cleavage in isolation, and because anisole is an intermediate in guaiacol HDO, particularly over Re/C and PdRe/C. As expected for a reactant molecule with only a single oxygen functional group, anisole HDO selectivity to fully deoxygenated products was greater over all the catalysts, in comparison to guaiacol (Table 5). The yields (except for Ru/C) fall much closer to the 45-degree line that represents 100% selectivity to benzene and cyclohexane, than they did in guaiacol HDO. This high selectivity suggests that benzene is a primary product in anisole HDO. The yield of benzene and cyclohexane over Ru/C is particularly low due to hydrogenolysis to phenol and to cracking to low-molecular weight products.

Table 5. Anisole conversion and C selectivity to products at 300°C, ambient pressure and 1 h⁻¹ WHSV

	Pd/C (E)*	Pd/C (N)*	Pd/C (N)	PdRe/C	Re/C	Ru/C
Conversion	36.6	32.1	14.2	86.4	50.7	83.7
	% C selectivity					
cyclohexane	2.4	38.5	30.6	27.7	3.0	6.7
benzene	51.5	29.9	24.3	68.5	93.8	48.3
phenol	14.8	0.7	15.1	0.1	0.6	14.6
cyclohexanol	10.8	1.4	3.3	0.0	0	3.5
MCH	14.2	21.6	20.1	0.8	0	2.5
MeOH	2.7	3.4	6.3	0.1	0	0.8
CO	0.6	0.9	0	0.1	0	1.3
CH ₄	0.8	0.1	0.1	2.1	2.6	5.7
low RT	0	0	0	0.6	0	16.0
Yield benzene + cyclohexane	19.7	21.9	7.8	83.1	49.1	46.1
% C balance closure	87.9	103.7	95.0	95.1	85.8	75.7

*Reduced *in situ* at 300°C; others reduced at 400°C

Conversion of anisole is equivalent over Pd/C catalysts reduced at 300°C, but, as expected, reduction of Pd/C (N) at 400°C has deleterious effect on conversion. Anisole HDO proceeds to completion over Pd/C, unlike guaiacol. Both Pd/C catalysts hydrogenate anisole to methoxycyclohexanol. Hydrogenolysis of anisole to phenol (and ring saturation to cyclohexanol) is also observed over Pd/C (E). Nonetheless, substantial HDO to benzene and cyclohexane proceeds over Pd/C. Pd/C is able to convert anisole to benzene through demethoxylation, i.e., benzene is a primary product from anisole HDO over Pd/C. Whereas Pd/C was selective to phenol and cyclohexanol in guaiacol HDO, it forms a relatively small amount of these products from anisole; thus, it is clear that Pd/C is not selective to demethylation of anisole to phenol. Gas yields for all anisole HDO experiments are lower than expected, but the sum of MeOH and CO selectivities are much higher than CH₄ selectivity for both Pd/C catalysts.

PdRe/C generates the highest yield of benzene and cyclohexane from anisole, as with guaiacol. In fact, both Re-containing catalysts come closest to the 45-degree line in Figure 13. Undesirable ring saturation is diminished over PdRe/C as compared to Pd/C and Ru/C catalysts. Re/C and PdRe/C are also highly selective to CH₄ among C₁ products, but any phenol formed by O-CH₃ bond hydrogenolysis of anisole must be rapidly deoxygenated, as phenol selectivity is negligible. Clearly, Re is able to convert phenol to benzene because this conversion step is required for complete deoxygenation of guaiacol.

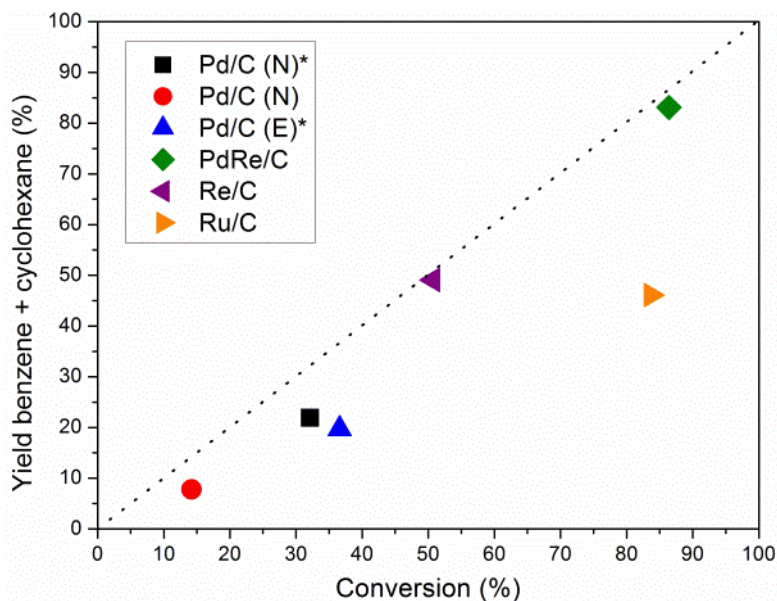


Figure 13. Conversion of anisole and yield fully deoxygenated compounds at 300°C, 1 h⁻¹ WHSV (* reduced *in situ* at 300°C; others reduced at 400 °C)

3.6 Guaiacol primary products and formation rates

Guaiacol HDO experiments were conducted at 300°C and higher WHSVs (4-28 h⁻¹) in order to achieve differential conversions (<10%) allowing the identification of primary products and determination of reaction rates. Several low conversion conditions were observed in order to construct first-order Delplots (Figure 14); by linearly extrapolating these plots to zero conversion, primary products could be determined [54]. Primary refers specifically to products formed on the catalyst surface following only one adsorption event; i.e., no intermediate products desorb and readsorb [54]. Phenol, anisole, 2-methoxycyclohexanol and catechol were determined to be primary products over all catalysts tested. Accordingly, these products occupy positions adjacent to guaiacol in the reaction network in Figure 15. RT9.718 was also a primary product over all catalysts except for

Re/C. Other products gave near-zero y-intercepts, and thus they were classified as be secondary (or higher-order) products.

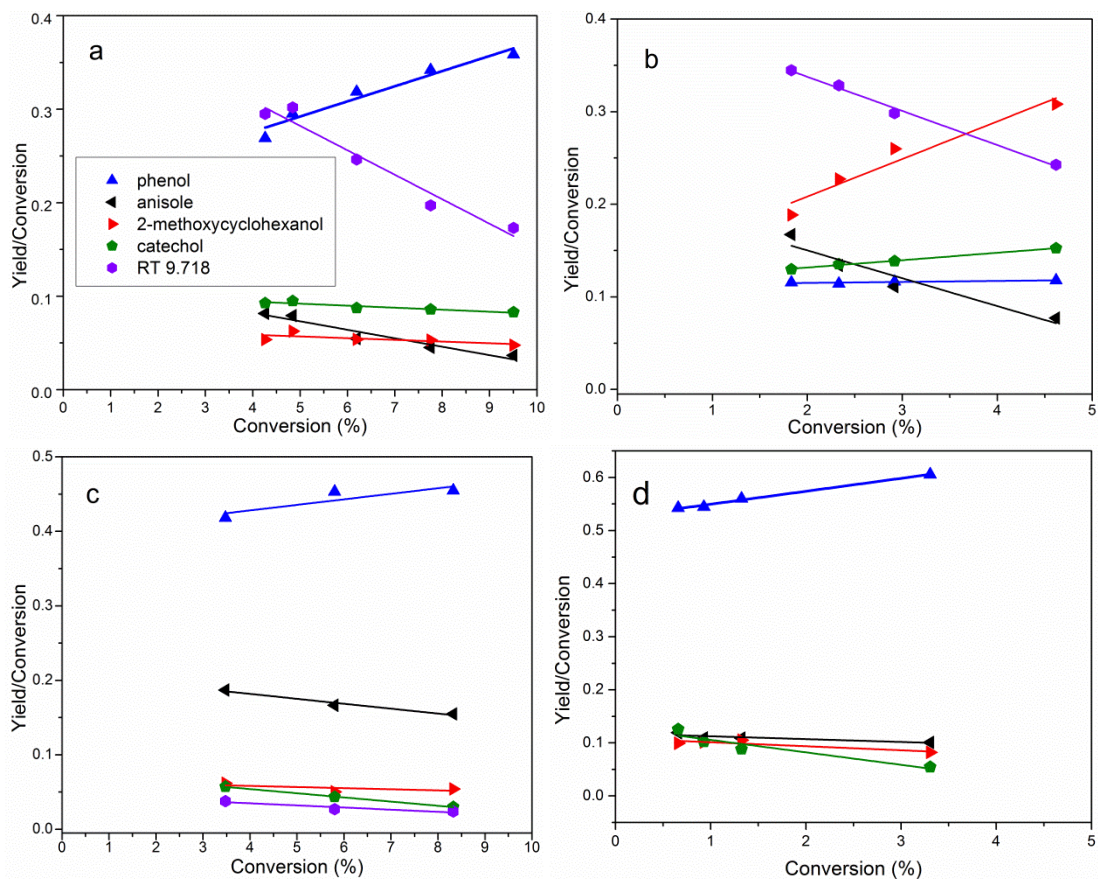


Figure 14. First-order delplots for a) Pd/C (E), b) Pd/C (N), c) PdRe/C and d) Re/C, showing primary products for each catalyst

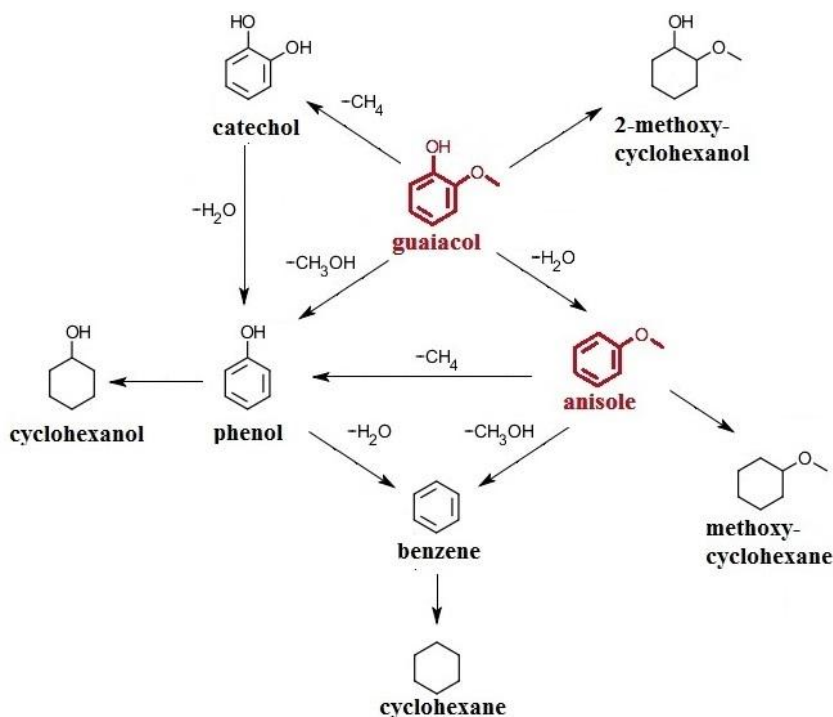


Figure 15. Reaction pathways for guaiacol and anisole over supported noble metal catalysts

Product formation rates were calculated from measured product concentrations assuming differential conversion (Table 6). Formation rates for higher order (non-primary) products are understood to be apparent rates. Corresponding turnover frequencies (TOF) were calculated using CO uptake from chemisorption experiments. Pd/C (E), PdRe/C and Re/C are considered, excluding Pd/C (N) due to its poor performance. Production rates are highest over PdRe/C for all products observed, except the putative hydrogenation product, RT9.718, over the commercial Pd/C catalyst. Unlike either Pd/C (E) or Re/C, PdRe/C exhibits significant production rates of benzene and cyclohexane. Furthermore, the production rates of phenol and anisole are substantially higher than the sum of the same rates over Pd/C (E) and Re/C, suggesting synergy of the two metals. Boosting the formation rates

of partially deoxygenated primary products leads to the observed efficacy PdRe/C has in full deoxygenation at higher conversion. Indeed, anisole was converted with nearly 100% selectivity to hydrocarbons over PdRe/C; thus, we infer that this pathway is important for benzene production from guaiacol.

Table 6. Product formation rates and turnover frequencies (TOF) at 300°C and ambient pressure based on rates and CO chemisorption uptake

Product	Rate (mol/g _{cat} /h) x 10 ³			TOF (#/site/h)		
	Pd/C (E)	PdRe/C	Re/C	Pd/C (E)	PdRe/C	Re/C
cyclohexane	0	0.34	0	0.0	1.5	0.0
benzene	0	1.5	0.10	0.0	6.7	0.4
phenol	2.16	5.20	1.20	55.1	23.2	5.4
cyclohexanol	0.38	1.14	0	9.7	5.1	0.0
anisole	0.37	1.51	0.18	9.4	6.7	0.8
2-MCH	0.34	0.59	0.16	8.6	2.6	0.7
catechol	0.62	0.25	0.14	0.0	0.3	0.0
RT 9.718	1.77	0.20	0.01	15.8	1.1	0.6
MeOH	1.96	4.40	0.30	45.1	0.9	0.1
CO	0.34	0.99	0.19	2.7	0.0	0.0
CH ₄	0.07	2.22	0.78	49.8	19.6	1.4

*Pd/C (E) reduced *in situ* at 300°C; others reduced at 400°C

For Pd/C (E) there is good correlation between the sum of phenol and cyclohexanol production rates and the sum of MeOH and CO production rates, suggesting simple scission of the phenyl-O bond. This finding supports the high conversion results showing Pd/C (E) selectivity to demethoxylation. Re/C produces more CH₄ than CO or MeOH, thus phenol should result from HDO of catechol, formed when CH₄ is cleaved from guaiacol. The correlation between catechol and CH₄ TOFs over Re/C is not as clear as for MeOH and phenol over Pd/C; although selectivity to CH₄ is higher, both pathways proceed over Re/C.

The reaction of guaiacol to catechol was suggested to be the most rapid of the reactions over Pt/Al₂O₃ [16]; however, rates of catechol formation are low as compared to CH₄. If phenol is produced as a primary product (through demethoxylation) and as a secondary product (through HDO of catechol), the observed rate of catechol formation would decrease. The Delplot for Re/C (Figs. S4c and d) shows that as conversion decreases, the selectivity to phenol decreases. Catechol is the only product for which selectivity increases approaching the y-axis over Re/C. Over PdRe/C, catechol and anisole increase with lower conversion while phenol decreases. This suggests that phenol is formed by several pathways over PdRe/C: demethoxylation of guaiacol, hydrogenolysis of anisole and HDO of catechol, thus all these pathways are represented in Figure 10. The bimetallic catalyst exhibits a higher combined rate of CO and MeOH than CH₄. This result again suggests that both pathways are active over this catalyst. Furthermore, production rates of C₁ products are substantially higher than the sum of the Pd/C and Re/C, lending PdRe/C its enhanced HDO activity.

3.7 Nature of the Active Sites

We propose that surface sites comprising Pd and Re metal are responsible for the high activity of PdRe/C for complete HDO of guaiacol to hydrocarbons. Because Pd/C is unable to convert guaiacol to benzene and cyclohexane, even at high conversion, Re must play an active role in guaiacol HDO, specifically enabling HDO of phenol. This hypothesis is supported by comparing the selectivities of phenol, benzene and cyclohexane in Table 4; Re/C is selective to phenol and benzene, but it lacks the hydrogenation activity to make cyclohexane; thus, benzene must have been hydrogenated by Pd in PdRe/C. Pd/C makes no benzene or cyclohexane; thus, Re must be responsible for full deoxygenation of phenol and

cyclohexanol in PdRe/C. Furthermore, it is clear from Re-Re and Re-O coordination numbers obtained from EXAFS spectra that metallic Re predominates in Re/C and PdRe/C after treatment. The Tomishige group suggests that ReO_x clusters that are in contact with metallic Pd or Rh particles are the active species in hydrogenation of carboxyl groups [20] and CO oxidation [24, 27]. The enhancement in benzene and cyclohexane yields that comes with 400°C instead of 300°C reduction temperature of Re/C and PdRe/C suggests that the active Re species is metallic. H_2 spillover from Pd in PdRe/C was established by TPR, and it is conceivable that the presence of excess H_2 on the metal surface prevents oxidation of active Re^0 . Spillover H_2 which keeps Re reduced explains the increased stability of PdRe/C as compared to Re/C.

4 Conclusions

The increased deoxygenation activity of PdRe/C and improved stability with time on stream result from the intimate contact of Re with the surface of Pd particles, as suggested by EXAFS spectra and STEM-EDX. However, the metals are mostly within homometallic particles, as evidenced by Pd-Pd and Re-Re coordination numbers determined from EXAFS spectra, and PdH_x formation. Metallic Re is proposed to be the active Re species owing to the increased activity of Re/C and PdRe/C after 400°C reduction.

PdRe/C was demonstrated to have enhanced deoxygenation activity, as compared to Pd/C and Ru/C, in the conversion of guaiacol and anisole to benzene and cyclohexane. Generally speaking, Re confers the ability to deoxygenate phenolics that Pd lacks. Pd and Re also have different selectivities to the two pathways for methoxy- group removal: Pd is

selective to phenyl C-O hydrogenolysis to make phenol and methanol; whereas, Re is selective to scission of the methyl C-O bond to make catechol and methane. The selectivity to these two pathways was first supposed based on matching rates of formation of methanol and phenol over Pd/C catalysts and then established using anisole.

5 Acknowledgements

This material is based upon work supported by the Department of Energy under Award Number DE-FG36-08GO88053. We are grateful to ExxonMobil for use of Beamline X10C and to the Naval Research Laboratory for use of Beamline X11A at the National Synchrotron Light Source, Brookhaven National Laboratory, supported by the Department of Energy. ICP-OES was performed at Eastman Chemical Company.

References

- [1] Y.C. Lin, G.W. Huber, *En. & Env. Sci.*, **2** (2009) 68-80.
- [2] A.V. Bridgwater, *App. Catal. A*, **116** (1994) 5-47.
- [3] E. Laurent, B. Delmon, *App. Catal. A*, **109** (1994) 97-115.
- [4] Q. Zhang, J. Chang, T.J. Wang, Y. Xu, *En. Convers. and Manage.*, **48** (2007) 87-92.
- [5] D.C. Elliott, A. Oasmaa, *Energy Fuels*, **5** (1991) 102-109.
- [6] E. Laurent, B. Delmon, *App. Catal. A*, **109** (1994) 77-96.
- [7] J. Wildschut, F.H. Mahfud, R.H. Venderbosch, H.J. Heeres, *Ind. Eng. Chem. Res.*, **48** (2009) 10324-10334.
- [8] Y.-C. Lin, C.-L. Li, H.-P. Wan, H.-T. Lee, C.-F. Liu, *Energy Fuels*, **25** (2011).
- [9] Z.Y. Luo, S. Wang, Y.F. Liao, J.S. Zhou, Y.L. Gu, K.F. Cen, *Biomass & Bioenergy*, **26** (2004) 455-462.
- [10] E. Furimsky, *App. Catal. A*, **199** (2000) 147-190.
- [11] J.H. Marsman, J. Wildschut, F. Mahfud, H.J. Heeres, *J. Chromatography A*, **1150** (2007) 21-27.
- [12] W.J. Song, Y.S. Liu, E. Barath, C. Zhao, J.A. Lercher, *Green Chemistry*, **17** (2015) 1204-1218.
- [13] J. Wildschut, M. Iqbal, F.H. Mahfud, I. Melian-Cabrera, R.H. Venderbosch, H.J. Heeres, *En. Env. Sci.*, **3** (2010) 962-970.
- [14] D.C. Elliott, T.R. Hart, G.G. Neuenschwander, L.J. Rotness, A.H. Zacher, *Env. Prog. Sus. Energy*, **28** (2009) 441-449.
- [15] A. Gutierrez, R.K. Kaila, M.L. Honkela, R. Slioor, A.O.I. Krause, *Catal. Today*, **147** (2009) 239-246.
- [16] R.C. Runnebaum, T. Nimmanwudipong, D.E. Block, B.C. Gates, *Catal. Sci. Tech.*, **2** (2012) 113-118.

- [17] T. Nimmanwudipong, R.C. Runnebaum, D.E. Block, B.C. Gates, *Catal. Lett.*, **141** (2011) 779-783.
- [18] D. Gao, C. Schweitzer, H.T. Hwang, A. Varma, *Ind. Eng. Chem. Res.*, **53** (2014) 18658-18667.
- [19] M.A. Gonzalez-Borja, D.E. Resasco, *Energy Fuels*, **25** (2011) 4155-4162.
- [20] J.M. Sun, A.M. Karim, H. Zhang, L. Kovarik, X.H.S. Li, A.J. Hensley, J.S. McEwen, Y. Wang, *J. Catal.*, **306** (2013) 47-57.
- [21] D.A. Simonetti, E.L. Kunkes, J.A. Dumesic, *J. Catal.*, **247** (2007) 298-306.
- [22] E.L. Kunkes, D.A. Simonetti, J.A. Dumesic, W.D. Pyrz, L.E. Murillo, J.G.G. Chen, D.J. Buttrey, *J. Catal.*, **260** (2008) 164-177.
- [23] O.M. Daniel, A. DeLaRiva, E.L. Kunkes, A.K. Datye, J.A. Dumesic, R.J. Davis, *Chemcatchem*, **2** (2010) 1107-1114.
- [24] S. Koso, H. Watanabe, K. Okumura, Y. Nakagawa, K. Tomishige, *J. Phys. Chem. C*, **116** (2012) 3079-3090.
- [25] Y. Takeda, Y. Nakagawa, K. Tomishige, *Catal. Sci. Tech.*, **2** (2012) 2221-2223.
- [26] A. Shimao, S. Koso, N. Ueda, Y. Shinmi, I. Furikado, K. Tomishige, *Chem. Lett.*, **38** (2009) 540-541.
- [27] T. Ebashi, Y. Ishida, Y. Nakagawa, S.-i. Ito, T. Kubota, K. Tomishige, *J. Phys. Chem. C*, **114** (2010).
- [28] S. Koso, I. Furikado, A. Shimao, T. Miyazawa, K. Kunimori, K. Tomishige, *Chem. Comm.*, **3** (2009) 2035-2037.
- [29] A. Malinowski, W. Juszczuk, M. Bonarowska, J. Pielaszek, Z. Karpinski, *J. Catal.*, **177** (1998) 153-163.
- [30] W. Juszczuk, Z. Karpinski, *App. Catal. A*, **206** (2001) 67-78.
- [31] M. Bonarowska, A. Malinowski, Z. Karpinski, *App. Catal. A*, **188** (1999) 145-154.
- [32] G. Meitzner, G.H. Via, F.W. Lytle, J.H. Sinfelt, *J. Chem. Phys.*, **87** (1987) 6354-6363.
- [33] S.B. Ziemecki, G.A. Jones, J.B. Michel, *J. Catal.*, **99** (1986) 207-217.

- [34] F.W.H. Kampers, T.M.J. Maas, J. Vangrondelle, P. Brinkgreve, D.C. Koningsberger, *Rev. Sci. Instr.*, **60** (1989) 2635-2638.
- [35] M. Newville, *J. Synch. Rad.*, **8** (2001) 322-324.
- [36] B. Ravel, M. Newville, *J. Synch. Rad.*, **12** (2005) 537-541.
- [37] B. Ravel, *J. Synch. Rad.*, **8** (2001) 314-316.
- [38] G.J. Kruger, E.C. Reynhardt, *Acta Crystal. B*, **34** (1978) 259-261.
- [39] C. Kittel, in, J. Wiley & Sons, Inc., 1996, pp. 23.
- [40] M. Boudart, H.S. Hwang, *J. Catal.*, **39** (1975) 44-52.
- [41] P.C. Aben, *J. Catal.*, **10** (1968) 224-234.
- [42] J.A. McCaulley, *J. Phys. Chem.*, **97** (1993) 10372-10379.
- [43] G. Fagherazzi, P. Canton, P. Riello, N. Pernicone, F. Pinna, A. Battagliarin, *Langmuir*, **16** (2000) 4539-4546.
- [44] R. Ducros, J. Fusy, J. Jupille, P. Pareja, S. Tatarenko, *App. Surf. Sci.*, **29** (1987) 179-193.
- [45] N.M. Gupta, V.P. Londhe, V.S. Kamble, *J.Catal.*, **169** (1997) 423-437.
- [46] R.W.G. Wyckoff, *Crystal Structures*, 2nd ed., Interscience Publishers, New York, NY, 1963.
- [47] G.H. Via, K.F. Drake, G. Meitzner, F.W. Lytle, J.H. Sinfelt, *Catal. Lett.*, **5** (1990) 25-33.
- [48] B. Predel, O.e. Madelung, in: *Landolt-Börnstein - Group IV Physical Chemistry*, SpringerMaterials.
- [49] Y. Matsumura, N. Tode, T. Yazawa, M. Haruta, *J.Mol. Catal.*, **99** (1995) 183-185.
- [50] W.J. Shen, Y. Matsumura, *J. Mol. Catal.*, **153** (2000) 165-168.
- [51] R. Ubago-Perez, F. Carrasco-Marin, C. Moreno-Castilla, *App. Catal. A*, **275** (2004) 119-126.

[52] J. Wildschut, I. Melian-Cabrera, H.J. Heeres, *App. Catal. B*, **99** (2010) 298-306.

[53] Y. Nakagawa, M. Ishikawa, M. Tamura, K. Tomishige, *Green Chemistry*, **16** (2014) 2197-2203.

[54] N.A. Bhore, M.T. Klein, K.B. Bischoff, *Ind. Eng. Chem. Res.*, **29** (1990) 313-316.

CHAPTER 2: PALLADIUM-RHENIUM CATALYSTS FOR SELECTIVE HYDROGENATION OF FURFURAL

Abstract

Pd-Re/Al₂O₃ catalysts are shown to possess superior activity and selectivity as compared to Pd/Al₂O₃ in selective hydrogenation of furfural to furfuryl alcohol (FAL). Three preparation methods were used for bimetallic catalysts, and of these, catalysts prepared by sequential impregnation (PdRe seq.) gave superior performance to catalysts prepared by co-impregnation (PdRe co.) or Re impregnation on a reduced and passivated Pd/Al₂O₃ catalyst (Re-Pd⁰ seq.). Greater suppression of H₂ chemisorption, as quantified by lower H_{ads}/CO_{ads} chemisorption ratios, correlates with higher furfural turnover frequency (TOF); however, below an H_{ads}/CO_{ads} threshold of ~0.2, catalyst activity drops precipitously. Pd-Re bonding is evident from fitting of extended x-ray absorption fine structure (EXAFS) spectra of the bimetallic catalysts. Substitutional alloying of Re in large Pd-rich particles is evident from strong suppression of β-PdH_x formation in the PdRe co. and Re-Pd⁰ seq. catalysts; however, Pd-Re bonding in PdRe seq. catalysts is primarily surface bonding of Re and Pd particles. This conclusions are supported by high-resolution scanning-transmission electron microscopy (STEM) with energy-dispersive x-ray (EDX) imaging.

1 Introduction

Catalytic production of fuels and chemicals from biomass has become an area of intense research in recent years. Pyrolysis of hemicellulose leads to furfural and related compounds. Selective hydrogenation of furfural to furfuryl alcohol (FAL) poses the challenge of selective aldehyde hydrogenation without decarbonylation to furan or ring opening to diols. Furfuryl alcohol is used as a monomer for resins used in many applications [1]. Resasco, et al., tested the activity of Cu-, Ni-, and Pd/SiO₂ catalysts towards furfural deoxygenation and hydrogenation [2-4]. They found that Pd was primarily active in decarbonylation of furfural to furan, but selectivity to FAL was increased with increased Cu loading in PdCu/SiO₂ catalysts [3]. Recently, Dumesic, et al., have studied hydrogenolysis and ring-opening of tetrahydrofurfuryl alcohol (THFAL) [5] and related compound, tetrahydropyran-2-methanol over RhRe/SiO₂ [6]. Coupled with DFT calculations, their results suggest that in aqueous reaction medium ReO_x species are hydroxylated and that due to the strength of the Re-O bond the proton can be donated, effectively acting as an acid site. Furthermore, Rh sites adjacent to the ReO-H acid sites add the hydrogenation/dehydrogenation function.

Until now, alumina-supported Pd-Re catalysts have only been studied by a handful of groups. Difficulty in adequate characterization arises primarily from the immiscibility of the two metals [7]. X-ray diffraction (XRD) data is only available for Pd-Re alloys is a composition of 88 at.% Pd-12 at.% Re [8]. The earliest work on PdRe/Al₂O₃ catalysts was performed contemporaneously by Meitzner, et al.[9] and Ziemecki, et al. [10, 11]. Meitzner, et al., found evidence for alloying in a 1:1 atomic ratio Pd-Re catalyst prepared by incipient

wetness co-impregnation of a solution of $\text{Pd}(\text{NO}_3)_2$ and HReO_4 . Extended x-ray absorption fine-structure (EXAFS) spectra of this catalyst indicated Pd-Re bonding. The presence of unreduced Re was not considered in fitting these spectra. Ziemecki, et al., made catalysts by a sequential method, wherein a solution of the Re precursor was added to a reduced and passivated $\text{Pd}/\text{Al}_2\text{O}_3$ catalyst [10]. Much of the patent literature on $\text{PdRe}/\text{Al}_2\text{O}_3$ and PdRe/C concerns this preparation method [12, 13]. Ziemecki, et al., observed decreased H/Pd ratios for $\beta\text{-PdH}_x$ formed during temperature-programmed reduction (TPR) after cooling in H_2 and repeating the ramp. The decreased desorption of H_2 was correlated to alloy formation in a $\text{PdRe}/\text{Al}_2\text{O}_3$ catalyst as well as bulk samples made by impregnation Pd black with Re_2O_7 and KReO_4 . *In situ* XRD spectra suggested that two PdRe solid solutions had formed [11]. Three papers by Karpinski, et al. [14-16], studied a series of compositions of $\text{PdRe}/\text{Al}_2\text{O}_3$ for dechlorination and alkane reforming activity. Their work likewise relied heavily on the suppression of hydride formation to characterize the nature of metal-metal interaction. Both Ziemecki and Karpinski suggest that the results of TPHD are a more reliable indication of alloying than TPR alone.

Recently, techniques aimed at fostering more direct metal-metal contact in PdRe bimetallics have been undertaken by Especel, et al. [17, 18], and Holles, et al. [19, 20]. The first approach is "catalytic reduction," whereby the Re precursor is reduced by H adsorbed on the surface of Pd particles, leading to its selective deposition on the surface of Pd particle. These catalysts were more effective at low Re loadings at selective hydrogenation of succinic acid to 1,4-butanediol [17]. The second technique, a so-called "overlayer" method, aims at the converse: selective deposition of Pd atoms on the surface of Re^0 particles using a

Pd(acac)₂ precursor. It was demonstrated that the H surface bond energy was diminished with respect to either Re or Pd alone via H₂ chemisorption [20], in accordance with DFT calculations for a pseudomorphic Pd layer on the Re(0001) surface [21, 22].

The nature of the active site in Re catalysts poses another challenge, as it is difficult to reduce fully to Re⁰. In many cases, Re metal coexists with ReO_x species, in particular Re⁴⁺ and Re⁷⁺ [23]. Tomishige, et al. have studied several Group VIII-Re bimetallic catalysts (Rh-Re [6, 24], Ir-Re [25], Pt-Re [26]), including PdRe/SiO₂ [27]. Using XAFS spectroscopy and X-ray photoelectron spectroscopy (XPS), they suggest in each case that the active site is at the interface of ReO_x clusters on the surface of the Group VIII metal; e.g., for selective hydrogenation of fatty acids to alcohols over PdRe/SiO₂ [27]. The strong interaction of Re and Al₂O₃ gives rise to additional complication. The formation of Re-O-Al bonds between Re⁷⁺ oxide species has been observed by Raman spectroscopy [28-32] and FTIR spectroscopy. Recently, an exhaustive study of a Re/MOR-Al₂O₃ catalyst by Bare, et al., used XAFS spectroscopy, STEM, XPS and TPR in conjunction with density functional theory (DFT) calculations to build a model of Re species (metal clusters, oxidic Re and monomeric Re on the support surface) in calcined and reduced catalysts [23].

In the current work, we compare the activity of Pd-Re catalysts prepared by co-impregnation and by sequential impregnation, wherein the Al₂O₃ support is first impregnated with Re, calcined, then impregnated with Pd, and calcined again. These are also compared to a catalyst prepared in the same manner as Ziemecki and Karpinski, wherein the Re precursor is added to a reduced and passivated Pd/Al₂O₃ catalyst. Catalysts made by sequential impregnation with an equimolar loading of Pd and Re exhibit significantly

increased rates of furfural conversion and higher selectivity to the desired product, FAL, as compared to the catalyst made by co-impregnation. The decarbonylation pathway is all but shut down in the bimetallic catalysts, whereas Pd/Al₂O₃ catalysts have nearly 40% selectivity to furan. The increased selectivity to hydrogenation is proposed to result from contact of Re metal particles with the surface of Pd metal particles, as evidenced by Pd-Re bonding in EXAFS spectroscopy and high-angle annular dark field-scanning transmission electron microscopy (HAADF-STEM) with energy-dispersive X-ray (EDX) spectroscopy. These techniques are used to explain the observations which had been made previously by TPR and TPHD regarding the extent of Pd-Re interaction. Furthermore, smaller Pd particles (<10 nm) and their even distribution across the support in sequential catalysts leads to increased Pd-Re contact, thereby adding more sites active for selective hydrogenation of furfural.

2 Experimental

2.1 Catalyst preparation

Catalysts were prepared by incipient wetness impregnation of γ -Al₂O₃ (183 m²/g BET surface area, 0.80 cm³/g total pore volume), purchased from Grace Davison (MI-309). Inductively-coupled plasma-optical emission spectrum (ICP-OES) analysis found low levels of alkali and alkaline earth metal impurities: 3.3 ppm Na, <0.3 ppm K, Ca and Mg. Two Pd precursors, [Pd(NH₃)₄(NO₃)₂] (tetraammine, TA) (10 wt% solution from Aldrich, 99%) and Pd(NO₃)₂ (nitrate, NO₃) (99.9% Pd basis, Strem), were used to make Pd/Al₂O₃ catalysts. The Pd (TA) catalyst was made using an impregnation solution of pH 10 by adjusting with NH₄OH (25 wt% NH₃, Fisher). Pd (NO₃) was made using a neutral solution due to the low

solubility of $\text{Pd}(\text{NO}_3)_2$ in water at high pH. In each case, the resultant paste was dried overnight at 110°C , then crushed and calcined at one of two conditions: 1 h at 350°C or 3 h at 400°C ($5^\circ\text{C}/\text{min}$ heating rate) in 0.6 L/min zero-grade air (National Welders) (Table 1).

Table 1. Catalyst preparation and metal content as determined by ICP-OES

Catalyst	Metal precursors	Pd loading (wt%)	Re loading (wt%)	Calcination conditions
Pd (NO_3)	$\text{Pd}(\text{NO}_3)_2$	3.04	---	350°C , 1 h
Pd (TA)	$\text{Pd}(\text{NH}_3)_4(\text{NO}_3)_2$	3.00	---	350°C , 1 h
PdRe co.	$\text{Pd}(\text{NO}_3)_2$ and HReO_4	3.02	5.00	350°C , 1 h
Re-Pd ⁰ seq.	$\text{Pd}(\text{NO}_3)_2$ and HReO_4	2.53	4.92	350°C , 1 h
PdRe seq. (350)	NH_4ReO_4 and $\text{Pd}(\text{NH}_3)_4(\text{NO}_3)_2$	2.84	4.55	350°C , 1 h
PdRe seq. (400)	NH_4ReO_4 and $\text{Pd}(\text{NH}_3)_4(\text{NO}_3)_2$	2.98	4.85	400°C , 3 h
PdRe (1:2) seq.	NH_4ReO_4 and $\text{Pd}(\text{NH}_3)_4(\text{NO}_3)_2$	3.02	9.21	350°C , 1 h
5% Re (H)	HReO_4	---	6.08	350°C , 1 h
10% Re (H)	HReO_4	---	9.61	350°C , 1 h
5% Re (N)	NH_4ReO_4	---	5.02	400°C , 3 h

$\text{PdRe}/\text{Al}_2\text{O}_3$ co. was prepared by incipient wetness co-impregnation using $\text{Pd}(\text{NO}_3)_2 \cdot \text{H}_2\text{O}$ and a 76.5 wt% solution of HReO_4 (99.99% Re, Acros Organics). A single aqueous solution with $\text{Pd}(\text{NO}_3)_2 \cdot \text{H}_2\text{O}$ and HReO_4 was added to Al_2O_3 to achieve incipient wetness. It should be noted that a co-impregnation catalyst prepared from $\text{Pd}(\text{NH}_3)_4(\text{NO}_3)_2$ and NH_4ReO_4 (or HReO_4) was not possible due to the precipitation of the double complex salt, $\text{Pd}(\text{NH}_3)_4(\text{ReO}_4)_2$.

$\text{PdRe}/\text{Al}_2\text{O}_3$ seq. catalysts were prepared using two incipient wetness impregnation cycles. First, 5% $\text{Re}/\text{Al}_2\text{O}_3$ was prepared by impregnating $\gamma\text{-Al}_2\text{O}_3$ with an aqueous solution

of NH_4ReO_4 (99+%, Alfa Aesar).. This powder was subsequently impregnated using an aqueous solution of $[\text{Pd}(\text{NH}_3)_4(\text{NO}_3)_2]$. The resultant paste was dried and calcined in the same manner as the previous cycle. This same procedure was used to make PdRe(1:2) seq., which has a nominal loading of 3 wt% Pd, 10 wt% Re, except that the 10% Re/ Al_2O_3 parent catalyst was made using HReO_4 .

Another sequentially prepared catalyst, referred to as Re-Pd⁰/ Al_2O_3 seq., was prepared by adding a solution of HReO_4 to reduced and passivated Pd/ Al_2O_3 prepared from $\text{Pd}(\text{NO}_3)_2$ as described above, similar to the preparation used by Ziemecki, et al. [10]. In this case, the parent Pd/ Al_2O_3 catalyst was reduced at 400°C for 1 h, cooled and then gradually exposed to air through loosened fittings. This catalyst was not calcined a second time after Re addition.

2.2 Furfural hydrogenation

Furfural hydrogenation was performed in a fixed-bed microreactor at 150°C and 1 atm under differential conversion conditions ($\leq 10\%$ conversion) in order to determine reaction rates. This apparatus was described previously (see Chapter 1 of this document). Liquid furfural was fed from a syringe pump (ISCO 260D) at 25-250 $\mu\text{L}/\text{min}$, evaporated in a stream of H_2 (UHP, National Welders), adjusted to maintain a constant molar H_2 :furfural ratio of 7.4, and passed over the catalyst bed. The catalyst bed was supported by a quartz wool plug and typically consisted of 100 mg catalyst with 1.25 g quartz chips to prevent channeling. An on-line GC-TCD (SRI 8610C) with a ShinCarbon ST100 (2 m x 1.0 mm ID) column (Restek) measured CO , CH_4 and CO_2 ; an on-line GC-FID (Shimadzu 2010) measured all other products. An EconoCap-1 column (30 m x 0.53 mm ID, Alltech) was

used in the latter. The GC-FID column program comprised a 5 min hold at 30°C, 20°C/min ramp to 220°C, where it was held for 2 min before cooling and repeating. Response factors were determined for all observed GC-FID products using high-purity standards; GC-TCD products were calibrated using a 5% H₂, 5% CO, 5% CO₂, 1% CH₄, balance He gas mixture (National Welders). The mass balance closure was >85% on a carbon basis. Turnover frequencies (TOF) were calculated using CO uptake values (mol/g_{cat}) as determined by volumetric chemisorption at 35°C.

2.3 N₂ Physisorption

The support surface area was measured using a Micromeritics 2020 ASAP surface area and porosimetry analyzer. Samples were degassed at 200°C for 2 h prior to measurement of adsorbed N₂ over a range of 0.06-0.26 atm at -196°C according to 5-pt Brunauer-Emmett-Teller (BET) analysis. These data are reported in Table 2.

Table 2. BET surface areas for Al₂O₃ supports and PdRe/Al₂O₃ catalysts

Sample	BET surface area (m²/g)
Al ₂ O ₃ – Grace (G)	183
Pd (TA)	183
PdRe co.	182
PdRe(1:1) seq. (350)	191
PdRe(1:2) seq.	172
Re (HReO ₄)	181

2.4 CO and H₂ Chemisorption

Volumetric chemisorption of CO and H₂ was performed in a Micromeritics ASAP 2020 surface area and porosimetry analyzer. Catalysts were reduced *in situ* at 400°C in 50

mL/min H₂ (Research grade, National Welders), followed by a 4 h evacuation at 400°C. Each sample was then evacuated for an hour at the analysis temperature following a leak test preceding analysis. Each analysis on the same sample was preceded by a 1 h evacuation at 300°C. Each catalyst sample was analyzed over the range of 100-450 Torr by H₂ (Research grade, National Welders) at 100°C, 70°C, and 35°C, and finally by CO (Research grade, National Welders) at 35°C. The H₂ was purified using an H₂O/O₂ trap (Oxilab DGP-125-R1).

CO pulse chemisorption was performed using a Micromeritics 2920 Autochem II. After *in situ* reduction at 400°C for 1 h in 5% H₂/Ar (certified, National Welders), the sample was cooled to 35°C and 0.5 mL pulses of 5% CO/He (certified, National Welders) were administered until the peak area did not change between consecutive pulses.

2.5 CO DRIFT Spectroscopy

DRIFT spectra were measured on a Bruker Vertex 70 FTIR with a liquid N₂-cooled MCT detector using a Harrick Praying Mantis cell with a high temperature *in situ* DRIFTS cell. In each case, 128 scans at a resolution of 4 cm⁻¹ were recorded. Samples were reduced at 400°C for 1 h in 40 sccm H₂ (Research grade, National Welders), and then purged in He at 40 sccm (UHP, National Welders) for 1 h before cooling to 20°C. Oxygen and water were removed from these gases using Alltech H₂ and He purifiers and an indicating oxygen trap for each. Pulses of 5% CO/He (certified, National Welders) were administered five at a time at 20°C until no further changes in spectra were observed. Scans of the reduced catalyst at 20°C in He were subtracted from scans following pulses of CO in order to subtract out signal from H₂O.

2.6 TPR and TPHD

TPR experiments were performed using a Micromeritics 2920 Autochem II equipped with a thermal conductivity detector (TCD) for monitoring H₂ uptake/desorption. Catalyst samples, in particular those containing Pd, were cooled to -50°C in He (UHP, National Welders), then the gas switched to 5% H₂/Ar (certified, Machine and Welding Supply). Both gases were purified using H₂O/O₂ traps (Oxilab). Once the TCD baseline was stable, the sample was heated at 10°C/min to 400°C and held for 1 h. Some samples, particularly Re/Al₂O₃ catalysts, were heated to 800°C. Hydride decomposition experiments were performed on Pd-containing samples by cooling to -50°C in H₂/Ar after 400°C reduction. A second ramp at 10°C/min to 400°C then proceeded to give TPHD profiles.

2.7 XAFS Spectroscopy

XAFS spectra were measured at the Advanced Photon Source at Argonne National Laboratory on beamline MR-CAT-10BM. Catalyst samples were reduced in a stream of 3.5% H₂/He (certified, Airgas), cooled to room temperature, and purged in He (UHP, Airgas). Pd foil (0.05 mm thick) and Re metal powder (350 mesh, 99.99% Re Strem) were used to calibrate the monochromator and served as references during experiments. Catalysts were measured in transmission mode after being pressed into a cylindrical cell as described in [33], made to enable simultaneous reduction of six samples and measurement at both Pd K- and Re L_{III}-edges. During scans at the Pd K-edge (24350 eV), the I₀ chamber was filled with a mixture of 40% N₂- 60% Ar and the I₁ chamber with 100% Ar; for the Re L_{III}-edge (10535 eV), mixtures of 95% N₂-5% Ar in I₀ and 30% N₂-70% Ar in I₁ were used.

The EXAFS signal was removed from the background using Athena data processing software [34]. Fourier transforms of the EXAFS were fit using Artemis [35] and FEFF references generated by ATOMS [36] and the appropriate lattice parameters for Re and Pd given in [37] and for NH_4ReO_4 [38]. A Pd-Re FEFF reference was generated by substituting 6 of the 12 nearest neighbors in an *fcc* lattice at the average Pd-Pd and Re-Re bond length (2.75 Å). The amplitude reduction factors, S_0^2 , 0.76 for Pd and 0.78 for Re, were determined using Pd foil and Re metal powder. The S_0^2 for Re agrees well with that used by [23]. The coordination number (N), bond length or interatomic distance (R), Debye-Waller factor (σ^2) and inner potential shift (ΔE_0) are reported for each path based on simultaneous k^n ($n=1-3$) fitting of the Fourier transform.

2.8 HR-STEM-EDX

An aberration-corrected FEI Titan 80-300 electron microscope was used for high-resolution scanning TEM. EDX spectra were captured using the microscope's high-angle annular dark field (HAADF) detector equipped with SuperX EDS system comprising four Bruker silicon drift detectors. The voltage was set to 200 kV. Samples were reduced *ex situ* at 400°C, transferred to a glove box in a N_2 -purged glove bag. Carbon-coated copper grids (Ted Pella) were dipped into the dry catalyst powder in the glove box under N_2 . Grids were briefly exposed to ambient air when putting the grid into the sample holder and inserting the holder into the microscope.

3 Results and Discussion

3.1 TPR

TPR profiles of all catalysts exhibit H₂ uptake features between 0-400°C (Figure). A small amount of H₂ uptake continues above 400°C on Re-containing catalysts due to Re, which interacts strongly with the Al₂O₃ support [23, 30]. The lowest temperature features in each profile beginning at ~0°C are clearly due to reduction of Pd, as seen in the profiles of Pd monometallic catalysts (Figure 2). For the most part, reduction of Pd in Pd (TA) and Pd (NO₃) is complete by 50°C. The inverse peak due to H₂ desorption which occurs at ~55°C in each of these profiles is due to the decomposition of β-PdH_x [10]. The position of the Re reduction peak for Re/Al₂O₃ catalysts depends on the loading and calcination temperature (Figure 1a). The maximum reduction of 5% Re (H) is at ~295°C, 60°C lower than for 10% Re (H), both of which were calcined at 350°C for 1 h. The maximum reduction temperature for Re/Al₂O₃ made from NH₄ReO₄ and calcined at 400°C for 3 h is 360°C, which is about 70°C higher than for 5% Re (H).

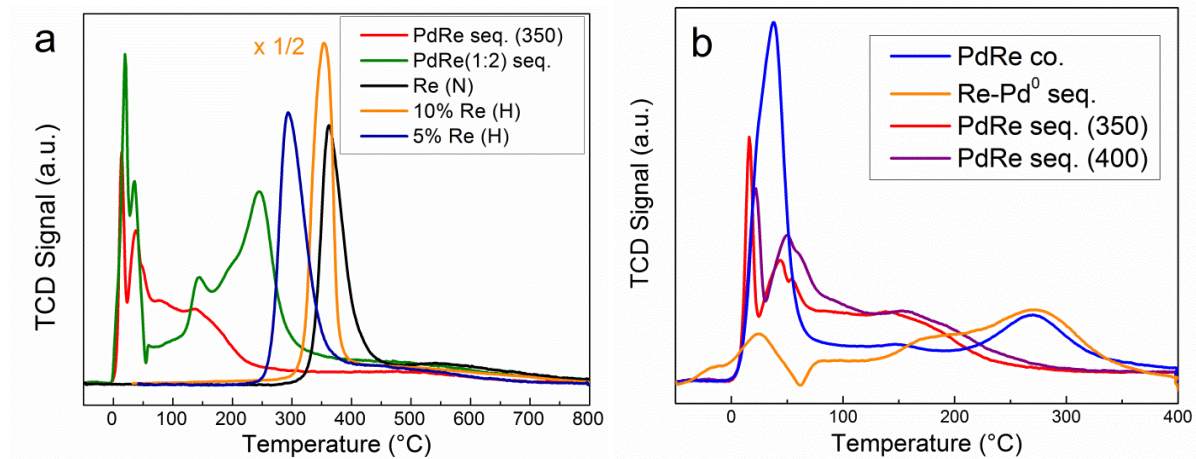


Figure 1. TPR profiles of a.) PdRe/Al₂O₃ seq. catalysts; b.) PdRe co. and monometallic catalysts up to 400°C and c.) PdRe seq. and Re catalysts reduced up to 800°C

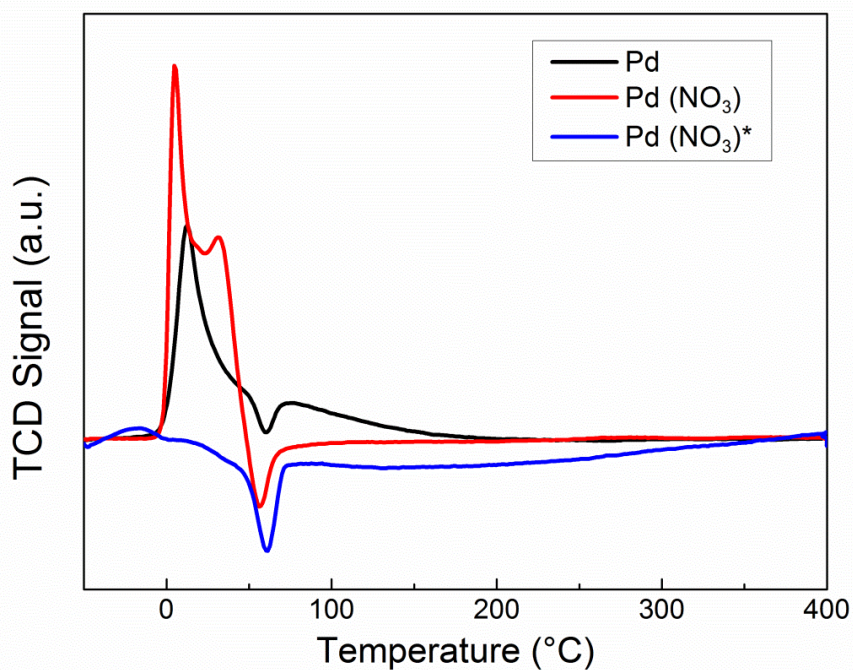


Figure 2. TPR profiles of Pd/Al₂O₃ catalysts (*reduced *ex situ* at 400°C; parent catalyst of Re on Pd/Al₂O₃)

The reduction of Re in the bimetallic catalysts takes place at lower temperatures than in any of the Re/Al₂O₃ catalysts. This effect has been observed previously for Pd-Re catalysts [10], and explained as facilitation of Re reduction by hydrogen spilled over from Pd particles. H₂ uptake on PdRe/Al₂O₃ catalysts begins at 0°C, as with Pd catalysts, but Re appears to be reduced at different temperatures in these catalysts, depending on the preparation method. This difference is taken to indicate the proximity and/or interaction (bonding) of Pd and Re. Clearly, some Re is reduced below 100°C, giving rise to, for example, the large feature in PdRe co. between 0 and 50°C, seen in Figure 1b. It can reasonably be assumed that Pd in the bimetallic catalysts is also reduced below 100°C (Figure 2), but the H/Pd ratio for the strong, sharp peaks below 75°C is >2.0 for all the catalysts, suggesting that a fraction of the Re is also reduced. In order for this portion of Re to be reduced >200°C lower than the monometallic catalyst, we infer that it is in intimate contact with Pd. H₂ uptake begins to decline at 175°C on the PdRe(1:1) seq. catalysts and is shifted to slightly higher temperatures on the catalyst calcined at 400°C as compared to 350°C. Re-Pd⁰ seq., PdRe co. and PdRe(1:2) seq. exhibit higher temperature peaks which corresponds to spatially segregated Re. Reduction of these more isolated Re species occurs at higher temperature than the rest because spilled-over H₂ must diffuse from Pd particles to them, or the ReO₄⁻ moieties must migrate to the Pd particles. These peaks are at 245°C in PdRe(1:2) seq. and 270°C in Re-Pd⁰ seq. and PdRe co. and are shifted to lower temperatures than the corresponding monometallic Re catalysts, 10% Re (H) and 5% Re (H), respectively. The similar TPR profiles of PdRe(1:2) seq. and 10% Re (H) above 400°C (i.e., relatively high H₂ uptake on this PdRe catalyst) suggest that there may be regions of the catalyst high in Re and

poor in Pd. On the contrary, the least-high-temperature Re reduction ($>400^{\circ}\text{C}$) is observed in PdRe seq. (350) (Figure 1a). This more facile reduction of Re in the bimetallic catalysts must be due to the catalytic effect of spillover H_2 from Pd.

3.2 CO and H_2 Chemisorption

CO and H_2 chemisorption uptakes ($\mu\text{mol}/\text{g}_{\text{cat}}$) and CO/H per metal atom basis are given in Table 3. There is a clear difference in Pd dispersion between the Pd (TA) and Pd (NO_3) catalysts, and the CO/Pd and H/Pd ratios are equivalent. Preparation of Pd/ Al_2O_3 using Pd(TA) results in smaller particles, probably due to the strong electrostatic adsorption effect [39]; i.e., the high pH of the impregnation solution compared to the point of zero charge of the Al_2O_3 support. The sequentially prepared catalysts, which were also made using $[\text{Pd}(\text{NH}_3)_4(\text{NO}_3)_2]$, similarly have higher CO uptake than the PdRe co. catalyst, also prepared from $\text{Pd}(\text{NO}_3)_2$. The CO/metal ratio for PdRe co. is similar to that of Pd (NO_3) and Re (H) catalysts, the monometallic analogues. CO/metal ratios for the 1:1 PdRe seq. catalysts fall between that of Pd (TA) and Re (N). The CO/metal ratio for PdRe(1:2) seq. is much closer to that of Re (N), a reflection of the high Re loading as compared to Pd. Volumetric CO uptake on Re/ Al_2O_3 catalysts is low, which might suggest large Re particles; however, we suspect this may result from oxidation of Re by hydroxyls on the Al_2O_3 support during 400°C evacuation preceding CO analysis in volumetric chemisorption [40, 41].

Table 3. Volumetric CO and H₂ chemisorption specific uptake ($\mu\text{mol}/\text{g}_{\text{cat}}$ CO or H₂) and molar CO (or H)/metal ratio as determined by ICP-OES

Catalyst	CO chemisorption		H ₂ chemisorption					
	CO uptake	CO/metal	35°C		70°C		100°C	
			H ₂ uptake	H/metal	H ₂ uptake	H/metal	H ₂ uptake	H/metal
Pd(NO ₃)	29.3	0.102	15.3	0.107	14.1	0.099	10.2	0.071
Pd (TA)	105	0.373	49.7	0.353	42.2	0.299	41.3	0.293
PdRe co.	45.5	0.082	12.3	0.045	12.3	0.045	11.6	0.042
Re-Pd ⁰ seq.	33.9	0.068	3.9	0.016	5.6	0.022	9.3	0.037
PdRe seq. (350)	87.7	0.172	14.3	0.056	16.0	0.063	21.6	0.084
PdRe seq. (400)	104	0.193	13.6	0.050	14.9	0.055	23.2	0.086
PdRe (1:2) seq.	96.5	0.124	6.3	0.016	15.2	0.039	26.9	0.069
Re (H)	28.9	0.098	1.4	0.010	4.1	0.028	5.9	0.040
Re (N)	37.1	0.138	3.2	0.024	10.0	0.074	10.2	0.076

For H₂ chemisorption at 35°C, the H/metal ratios are equivalent to CO/metal ratios on both Pd/Al₂O₃ catalysts. Uptake of H₂ decreases slightly on Pd/Al₂O₃ catalysts for analyses at higher temperatures. The H/metal ratio is much less than CO/metal ratio on Re/Al₂O₃ catalysts at 35°C, but increases at 70°C and 100°C, a reflection of the activated nature of H₂ dissociative chemisorption on Re [42]. Increasing H₂ uptake with increasing analysis temperature over PdRe and Re catalysts also reflects activated H₂ adsorption on Re. Strong suppression of H₂ uptake on PdRe catalysts suggests Re coverage of Pd particle surfaces. It is generally the case that alloys of early- and late transition metals exhibit suppressed H₂ chemisorption [43]. Moreover, DFT calculations predict that the surface bond energy of hydrogen is decreased on a mixed Pd(111)-Re surface [21]. The ratio of adsorbed H/CO in volumetric chemisorption at 35°C varies from 1 for Pd catalysts to ~0.1 for Re catalysts; bimetallic catalysts have intermediate H/CO chemisorption ratios.

3.3 Furfural hydrogenation activity testing

Furfural hydrogenation at 150°C and 1 atm was performed under differential conversion conditions in order to elucidate primary products using the Delplot method [44] and to determine reaction rates. Reaction pathways leading to all of the observed products were suggested by the Delplot results (Figure 3). No ring-opening products (e.g., butanol or pentanol) were observed under these conditions. Delplots for the two Pd catalysts (Figure 3a-b) show similar selectivity trends with furfural conversion. Furan, FAL, and THFAL appear to be primary products, and selectivities to furan and FAL are nearly equal. THF, 2-MF and 2-MTHF are secondary products. Over Re/Al₂O₃, 2-MF is a primary product in addition to the FAL, furan and THFAL. Selectivity to FAL over Re is suggested by its selectivity in the limit of zero conversion, i.e., the y-intercept of 65%, but, the comparatively low WHSVs make it clear that this catalyst possesses very low furfural hydrogenation activity. The differences between the PdRe/Al₂O₃ catalysts are subtle. Overall, they reflect the selectivity in the limit of zero conversion of Re, but exhibit far greater activity. The Delplots indicate that 2-MF is a primary product over all Re-containing catalysts.

Based on this analysis, furfural reaction pathways are proposed in Figure 4. Decarbonylation produces furan and CO (observed via GC-TCD); furan hydrogenation to THF is a secondary reaction that occurs over all catalysts. Selective hydrogenation of the aldehyde moiety to FAL is the desired pathway. FAL may be saturated to THFAL, and hydrogenation of FAL to THFAL can occur in competition with FAL desorption from the metal surface. Over PdRe co. and PdRe seq. (400), THFAL selectivity appears to be rising at higher conversion while FAL selectivity decreases. It is logical to infer that the furan ring

may be saturated in a secondary reaction, and that at higher conversion, more FAL will be converted to THFAL. The situation is similar for 2-MF. Although 2-MF appears to be a primary product, the selectivity of PdRe/Al₂O₃ catalysts to 2-MF increases at higher conversion, suggesting that some 2-MF may be formed from FAL via secondary reaction. Because of this uncertainty, 2-MF is shown both as being formed directly from furfural and by HDO of FAL. Ring saturation of 2-MF to form 2-MTHF is a secondary reaction, and scarcely any 2-MTHF is formed over these catalysts at 150°C and <10% conversion.

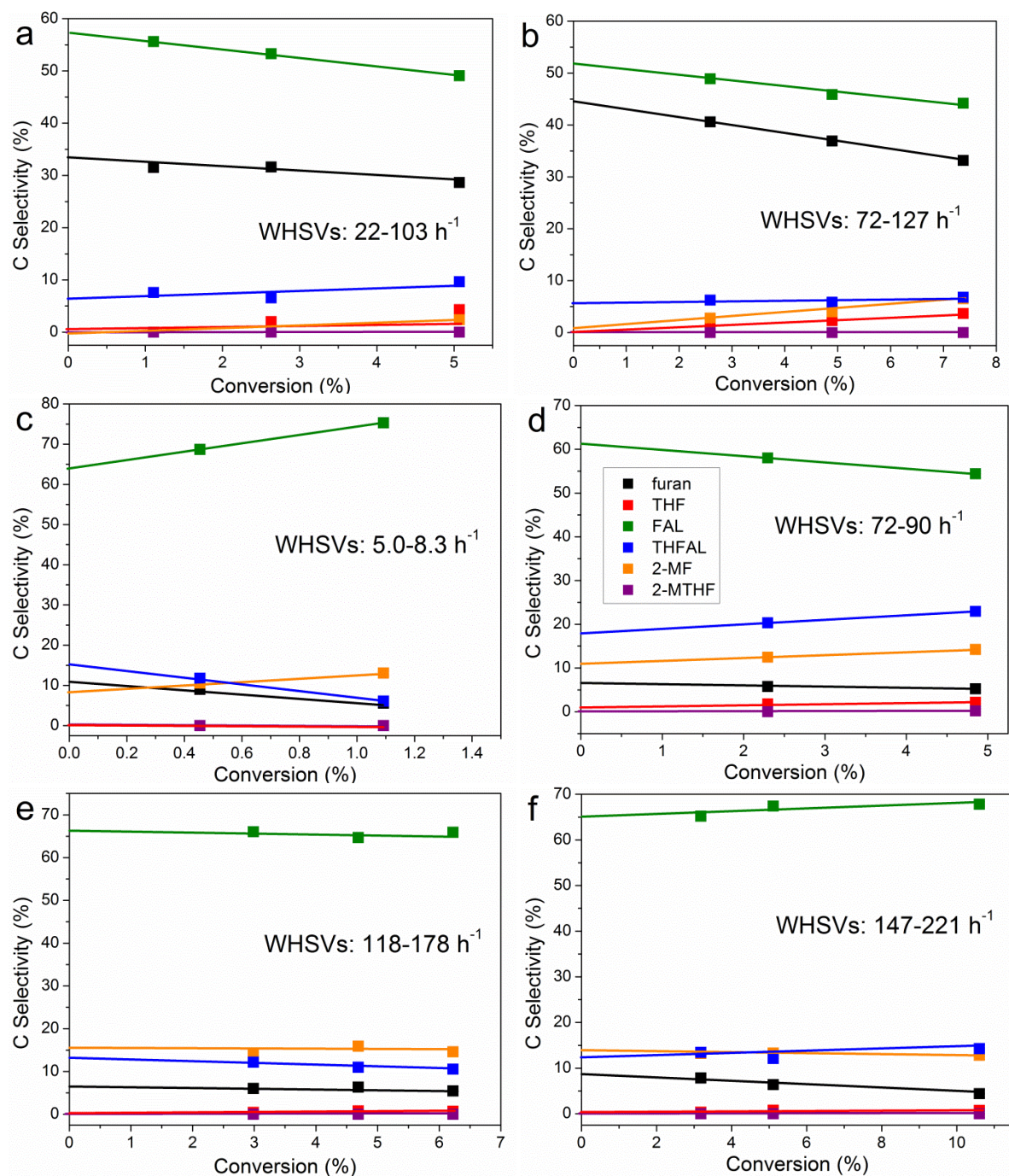


Figure 3. Delplots for furfural conversion at 150°C and 1 atm: a.) Pd (NO₃) b.) Pd (TA) c.) 5% Re (H) d.) PdRe co. e.) PdRe seq. (350) and f.) PdRe seq. (400); all on Al₂O₃ (A) support; WHSVs indicated

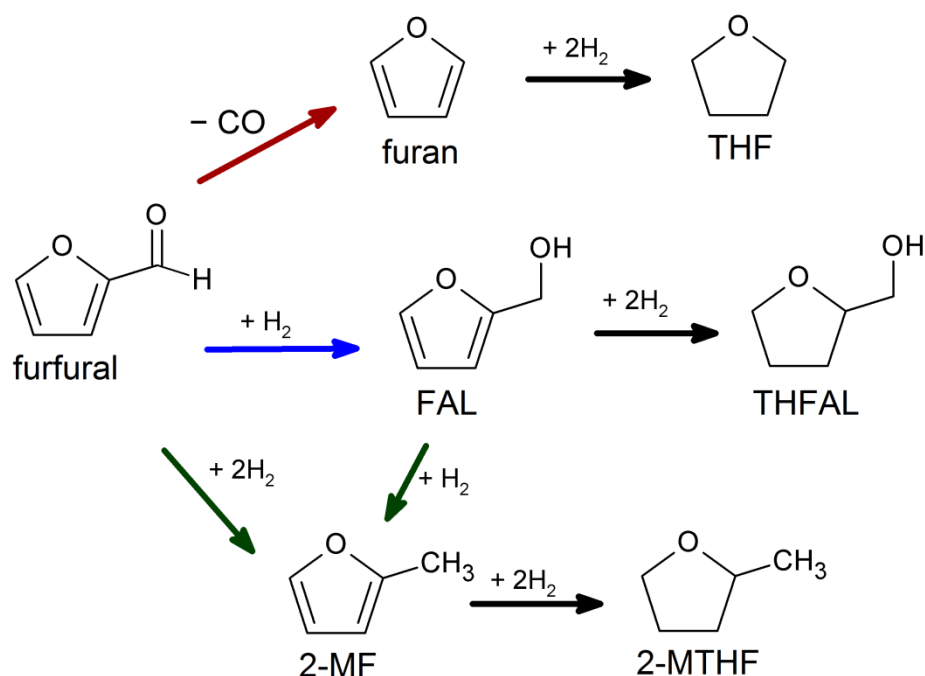


Figure 4. Furfural reaction pathways over PdRe/Al₂O₃ catalysts

Re/Al₂O₃ catalysts exhibit very low activity at 150°C requiring lower space velocities to achieve measurable conversion, whereas all Pd-containing are very active requiring weight hourly space velocities >70 h⁻¹ to achieve differential conversion. The rates of furfural consumption over Pd and PdRe catalysts are indicated by total bar heights in Figure 5. Pd/Al₂O₃ catalysts are less active than bimetallic catalysts made with the same precursor. The rate of furan production over Pd catalysts is ~40% of the total rate of furfural consumption, and Pd (TA) has the highest selectivity to furan. The furfural consumption rate is more than four times greater over the more highly-dispersed Pd (TA) catalyst as compared to Pd (NO₃). Turnover frequencies based on CO and H₂ chemisorption uptake (Table 4) demonstrate the equivalence in activity of surface Pd atoms in the two catalysts; all TOFs are very similar despite the difference in dispersion of the two catalysts.

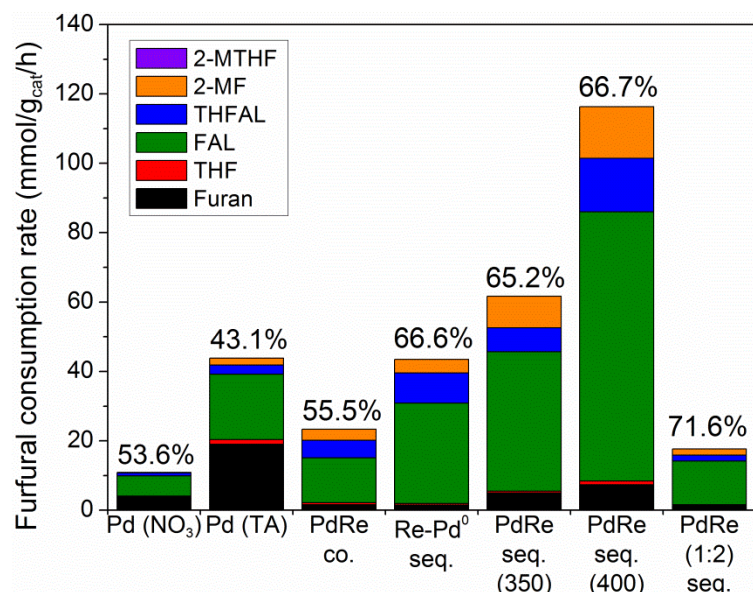


Figure 5. Product formation rates at 150°C and ambient pressure over PdRe/Al₂O₃, which sum to the furfural consumption rate; selectivity to FAL indicated

Table 4. TOFs (min⁻¹) at 150°C based on volumetric H and CO chemisorption uptake at 35°C

Basis	furfural		FAL		furan		2-MF		THFAL	
	CO	H	CO	H	CO	H	CO	H	CO	H
Pd (NO ₃)	6.2	5.7	3.3	3.1	2.2	2.1	0.0	0.0	0.5	0.5
Pd (TA)	6.9	7.3	3.0	3.2	3.0	3.2	0.3	0.3	0.4	0.4
PdRe co.	8.6	15.8	4.7	8.8	0.6	1.1	1.2	2.2	1.8	3.4
Re-Pd ⁰ seq.	21.4	92.0	14.2	61.2	0.7	3.2	1.9	8.3	4.3	18.3
PdRe seq. (350)	11.7	35.9	7.6	23.4	0.9	2.9	1.7	5.3	1.3	4.0
PdRe seq. (400)	18.6	71.2	12.4	47.5	1.2	4.5	2.4	9.1	2.5	9.4
PdRe(1:2) seq.	3.0	23.4	2.2	16.7	0.2	1.9	0.3	2.3	0.3	2.2

There is a marked decrease in furan production over the PdRe catalysts. Comparing Pd (NO₃) and PdRe co., made with the same Pd precursor, the rate of furfural consumption doubles, while furan selectivity is dramatically lower (Figure 5). The increase in FAL selectivity for PdRe co. is slight. Nevertheless, the THFAL production rate increases, and 2-

MF, which did not have a measurable rate over Pd (NO₃), is produced—both at the expense of furan production. TOFs (Table 4) reflect this change in selectivity; decarbonylation declines in favor of hydrogenation reactions, in particular to form FAL. Furfural consumption almost doubles again over Re-Pd⁰ seq. as compared to PdRe co., while FAL selectivity increases by >10%. The PdRe(1:1) seq. catalysts have much lower furan production rates than Pd (TA) indicating suppression of the decarbonylation pathway. Selectivity to FAL is equivalent for these two catalysts, but PdRe seq. (400) is nearly twice as active as PdRe seq. (350). Similar CO and H₂ chemisorption uptake over these two catalysts suggests that these two catalysts have nearly equal dispersions. Indeed, furfural TOFs (Table 4) reflect the difference in intrinsic activity of the two catalysts; the furfural TOF for PdRe seq. (400) is nearly double that of PdRe seq. (350). The PdRe(1:2) seq. catalyst has higher FAL selectivity than any of the PdRe (1:1) catalysts albeit lower activity.

The enhanced performance of the bimetallic catalysts in furfural conversion evidences synergy between Re and Pd. Re/Al₂O₃ has only slight activity compared to Pd/Al₂O₃ catalysts in furfural conversion; however, Re/Al₂O₃ has much higher FAL selectivity. Consequently, the active sites are expected to comprise Pd and Re atoms. Figure 6 shows furfural TOF (CO basis) and FAL selectivity plotted versus H/CO chemisorption ratio. The furfural TOF increases with decreasing H/CO ratio up to the maximum value at ~0.25 H/CO, corresponding to PdRe seq. (400) (Figure 6a). Below this ratio there is a precipitous decrease in furfural TOF, corresponding to PdRe(1:2) seq. FAL selectivity, on the other hand, appears to continue to decrease as the H/CO ratio decreases; furan selectivity decreases dramatically for H/CO < 1 (Figure 6b). Because H₂ chemisorption on Re at 35°C

is very low [42], suppression of H₂ chemisorption by the PdRe bimetallic catalysts is explained by the Re coverage of Pd nanoparticles. We infer that the H/CO chemisorption ratio characterizes the extent of Pd surface coverage by Re, and this correlates with activity and selectivity in furfural hydrogenation. Decarbonylation selectivity decreases dramatically for H/CO ratios < 1 and remains low as Re increasingly covers the Pd surface. FAL selectivity continuously improves with Re coverage of Pd because of greater intrinsic catalytic activity of PdRe sites for FAL formation. Furfural TOFs exhibit a maximum as Re coverage of Pd increases, since Re/Al₂O₃ is inactive in this reaction. For comparison, the H/CO ratio of 5% Re (H) is 0.10. CO or H₂ are useful as probe molecules because of the selectivity of H₂ chemisorption to Pd on the surface. A PdRe ratio of 1:2 evidently leads to greater suppression of H₂ than CO chemisorption ($H_{\text{ads}}/CO_{\text{ads}}=0.12$), suggesting that if Re covers too many of the Pd surface sites, the furfural consumption rate suffers, although a marginally higher selectivity to the desired product is obtained. These results for furfural hydrogenation motivate the use of further catalyst characterization to elucidate differences in surface structure and Pd-Re interaction which may correlate with catalytic activity.

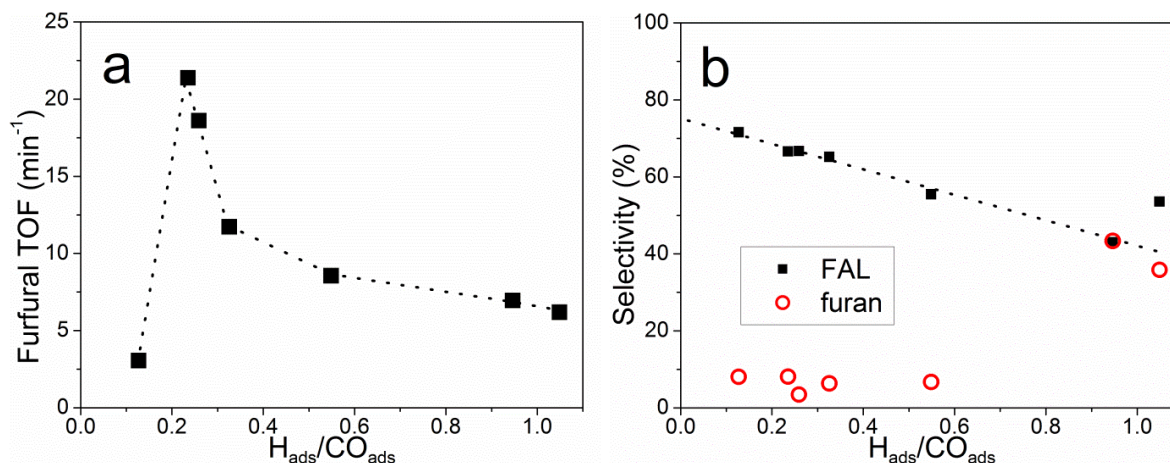


Figure 6. Furfural hydrogenation results at 150°C, 1 atm compared to the ratio of H to CO chemisorption uptake at 35°C: a.) furfural TOF (CO basis), b.) selectivity to FAL and furan

3.4 CO DRIFTS

Pd and PdRe/Al₂O₃ catalysts were reduced in situ at 400°C and purged with He at the reduction temperature. In contrast, the CO DRIFT spectrum of 5% Re represents a sample that was reduced in situ at 400°C and cooled in H₂ without a high temperature purge. Linear and bridging CO on Pd [45, 46] were observed over all Pd and PdRe catalysts (Figure 7). The ratio of linear CO on Pd (2086 cm⁻¹) to bridging CO on Pd (~1930 cm⁻¹) is much larger on Pd (TA) than Pd (NO₃), indicating that the former contains smaller Pd nanoparticles, in agreement with chemisorption data. Two doubly bridging species were also observed: one at 1991 cm⁻¹, which is very prominent in Pd (NO₃), but just a shoulder (1986 cm⁻¹) in Pd (TA), and a large broad peak at 1930 cm⁻¹ which also includes triply bridging CO. This suggests that there are some larger Pd particles present in Pd (TA) that have facets exposing low-index surface planes [46]. The CO DRIFT spectra of 5% Re and 10% Re are very similar. Linear

CO on Re (2042 cm^{-1}) dominates the spectrum of Re/ Al_2O_3 [40, 47]; only a small shoulder of bridging CO on Re/ Al_2O_3 is evident at $\sim 1940\text{ cm}^{-1}$.

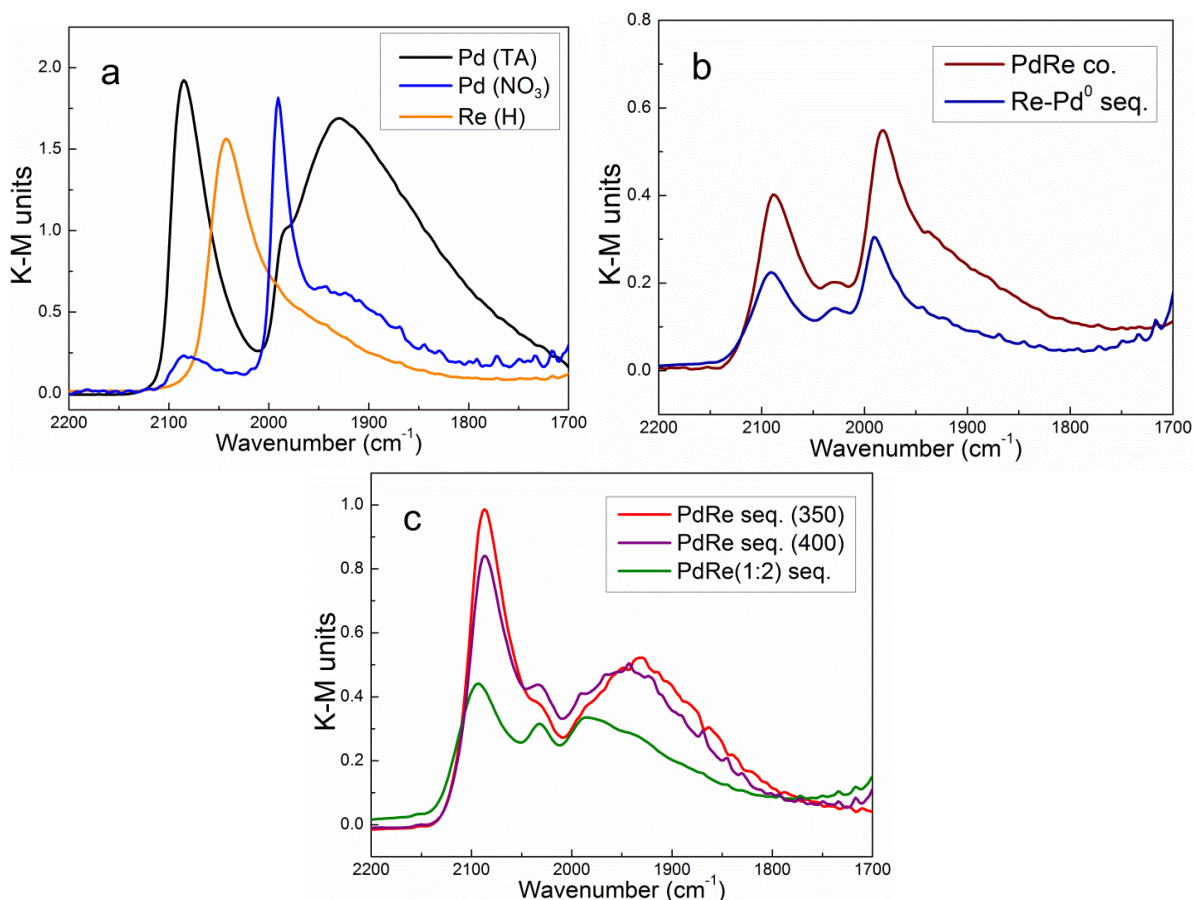


Figure 7. CO DRIFT spectra in Kubelka-Munk (K-M) transformation units on PdRe/ Al_2O_3 catalysts after 400°C reduction and 1 h purge in He (except for Re (H), which was not purged in He)

Infrared bands for CO adsorbed on PdRe/ Al_2O_3 catalysts (Figure 7b-c) appear at approximately same frequencies observed for the monometallic catalysts: linear and bridging CO on Pd and linear CO on Re. There are, however, important variations in the relative intensities of the peaks. The strong CO bridging peak at 1991 cm^{-1} on PdRe co. and Re- Pd^0

seq. is also present on Pd (NO₃), all of which were prepared from Pd(NO₃)₂ (Figure 7b). Analogously, the broad bridging CO peak on PdRe(1:1) seq. catalysts resembles that of Pd (TA), again, both made from the same precursor. The relative magnitude of bridging CO on Pd at ~1930 cm⁻¹ or 1990 cm⁻¹ is diminished with respect to linear CO on Pd on all bimetallic catalysts as compared to Pd/Al₂O₃ catalysts. The lowest bridging-to-linear ratio is for PdRe(1:2) seq. This ratio suggests that the surface of Pd particles may be interrupted by Re atoms, which would decrease the population of contiguous surface Pd atoms with the requisite geometry for bridging CO. The linear CO on Re peak is weak for all of these catalysts because all of the bimetallic catalysts were purged at high temperature in He. This peak is strongest relative to CO on Pd peaks for PdRe(1:2) seq., which contains twice as much Re as the other catalysts.

3.5 TPHD

A large H₂ desorption feature at 50-55°C in the TPHD profile of Pd (NO₃) is ascribed to β-PdH_x decomposition [10, 15] (Figure 8a). It has been shown that the maximum H/Pd ratio is dependent on the size of Pd particles [48-50] and that this ratio is diminished by alloying with a second metal [10]. The H/Pd ratios shown in Table 5 show that the H/Pd ratios of all catalysts *except* Pd (NO₃), are significantly below the bulk ratio of 0.65 for β-PdH_x. There is a stark difference in hydride formation for PdRe co., which has scarcely any hydride phase, and Pd (NO₃), which forms the most of all the catalysts (Figure 8a). Two low-temperature features evidencing the desorption of H₂ form in PdRe co., and there appears to be complete suppression of the more stable PdH_x phase characterized previously that decomposes at 40-55°C [11, 14, 48]. This latter PdH_x phase is present in Re-Pd⁰ seq.,

however, which was made by impregnating a catalyst with large, mostly reduced Pd particles (see Figure 2 for TPR profile of *ex situ* reduced Pd (NO₃) parent catalyst). Hydride formation is suppressed in this catalyst as compared to the Pd (NO₃) parent catalyst, suggesting some diffusion of Re into Pd particles during reduction, but to a lesser extent than in PdRe co. Desorption of H₂ at low temperature is suspected to result from decomposition of less stable PdH_x phases, i.e., α- or β-PdH_x forming in smaller particles or in alloyed particles which result in instability of the phase. Thermodynamic arguments support this assumption. The H/Pd ratio for peaks below 0°C are separated from those above 0°C in Table 4. In many profiles, there is a peak or a shoulder at 0-25°C. A distribution of different particle sizes and Re content could result in such a diversity of PdH_x stabilities.

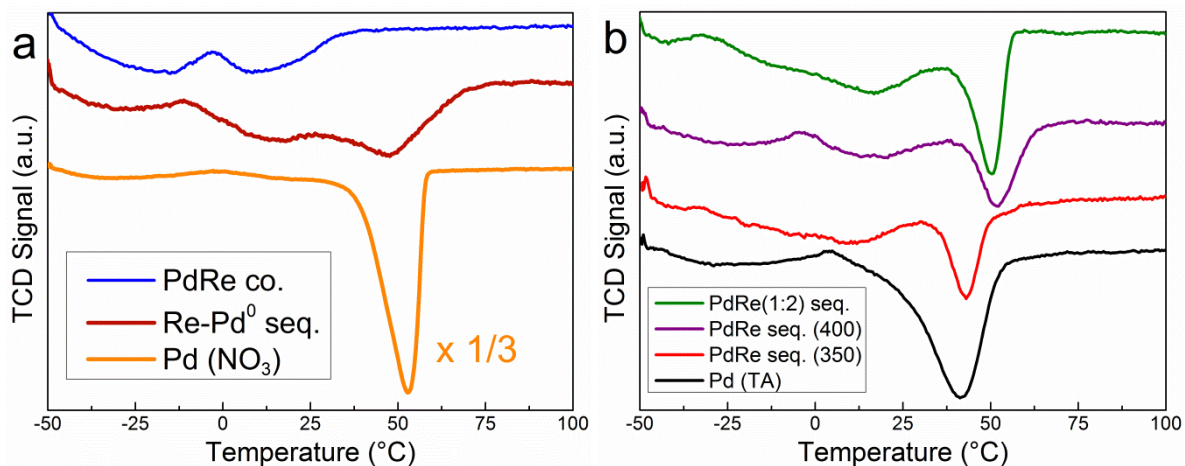


Figure 8. TPD profiles for PdRe/Al₂O₃ following 1 h reduction at 400°C and cooling in 5% H₂/Ar

Table 5. H/Pd ratios from H₂ desorbed during TPHD corresponding to Fig. 6; based on Pd loading as measured by ICP-OES

Catalyst	H/Pd		
	<0°C	>0°C	Total
Pd (NO ₃)	0.048	0.593	0.641
Pd (TA)	0.038	0.243	0.281
PdRe co.	0.070	0.065	0.135
Re-Pd ⁰ seq.	0.052	0.335	0.387
PdRe seq. (350)	0.000	0.186	0.186
PdRe seq. (400)	0.035	0.159	0.193
PdRe (1:2) seq.	0.017	0.344	0.361

Hydride formation in Pd (TA) is decreased and the hydride decomposes at a lower temperature (i.e., is less stable), which implies much smaller Pd particle size, as evidenced by CO and H₂ chemisorption and CO DRIFTS. The β -PdH_x decomposition feature at ~45°C (Figure 5b) is diminished even more in the PdRe seq. catalysts that were prepared using the same precursor. The PdRe(1:1) seq. catalysts have very similar features and H/Pd ratios, suggesting a similar Pd particle size and degree of Pd-Re interaction; however, there is a shift to higher temperatures for PdRe seq. (400) suggesting greater hydride stability. More H₂ evolves from PdRe(1:2) seq. at > 0°C than the other two sequentially prepared catalysts suggesting the formation of larger Pd particles and/or decreased Pd-Re alloying.

3.6 XAFS Spectroscopy

3.6.1 X-ray Absorption Near-Edge Structure (XANES) Spectroscopy

Intense white lines are observed just above the absorption threshold edge in the Re L_{III} XANES spectra of the catalysts (Figure 9a). These resonance features are due to *d* to *p* electronic transitions and provide qualitative evidence of increasing Re oxidation state from Re⁰ (Re metal powder) to Re⁷⁺ (PdRe seq. (350) "as is"); a larger white line signifies a

higher oxidation state. Re L_{III} x-ray absorption edge shifts were used to determine average Re oxidation states in the PdRe/ Al_2O_3 catalysts. Measurements of Re oxidation state from edge shifts are based on a calibration curve generated using several Re compounds: Re metal powder, ReO_2 , ReO_3 , Re_2O_7 and NH_4ReO_4 (Figure 9b). An edge shift of 4.0 eV was observed for Re^{7+} compounds, as well as for calcined PdRe/ Al_2O_3 catalysts; hence, all Re is present as ReO_4^- spread over the Al_2O_3 support following calcination, as observed in Re/ Al_2O_3 catalysts by several groups [23, 29, 41]. Following treatment in H_2 and purging in He at room temperature, the average Re oxidation state in 5% Re (H) was +2.6, equivalent to the average oxidation state estimated by H_2 uptake in TPR up to $400^\circ C$ of +2.4. Edge shifts for PdRe catalysts were less than Re/ Al_2O_3 , suggesting greater Re reduction either by direct interaction with Pd and/or hydrogen spillover. The average oxidation state determined for PdRe(1:2) seq. (+1.9) is slightly higher than that of PdRe seq. (350) and PdRe co. (+1.7). No difference in edge shifts for the latter two catalysts could be distinguished.

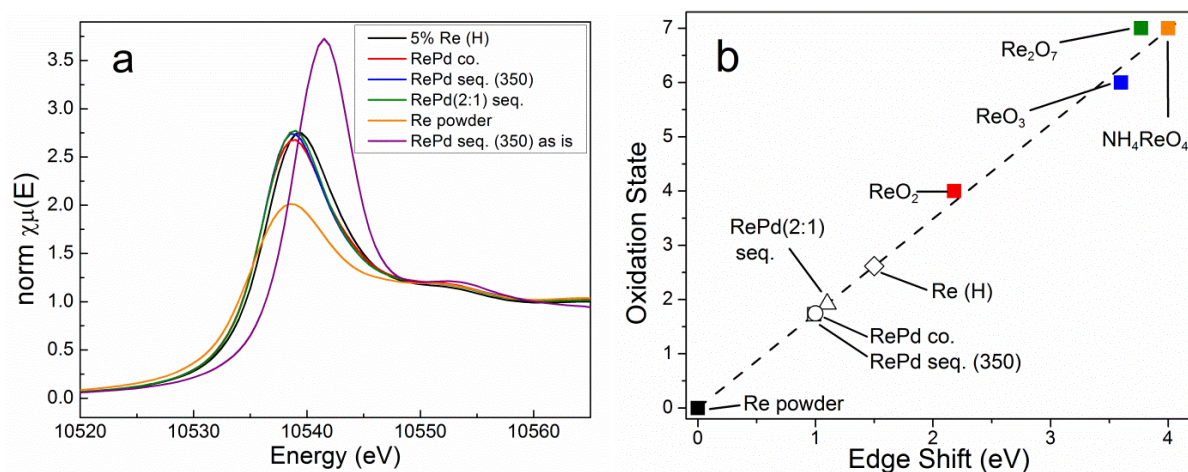


Figure 9. a.) Re L_{III} XANES of Re/ Al_2O_3 and RePd/ Al_2O_3 catalysts following *in situ* reduction (except RePd seq. "as is"); b.) XANES edge shift calibration with Re standards and PdRe/ Al_2O_3 catalysts following $400^\circ C$ reduction and He purge

3.6.2 EXAFS Spectroscopy

The k^2 -weighted EXAFS spectra and corresponding Fourier transforms (FT) of the PdRe/Al₂O₃ catalysts are displayed in Figure 10. EXAFS chi spectra ($k^2 \cdot \chi(k)$) and FTs (Figures 10a and 10c) at the Pd K edge exhibit very similar features. The most evident difference between the FTs are their magnitudes, in order PdRe(1:2) seq. > PdRe co. > PdRe seq. (350). At the Re L_{III} edge, on the other hand, significant features are observed, when compared to the EXAFS spectrum of 5% Re/Al₂O₃, that reflect differences in metal-metal bonding. Lower amplitude at high k may be attributed to a lower Re-Re coordination number, greater disorder, and/or to interference between Re-Re and Re-Pd backscattering. The latter also affects the magnitude and shape of the metal-metal peak at ~ 2.6 Å. Fourier transforms were generated using FEFF6 by replacing Re atoms with Pd atoms in the *fcc* first coordination shell at a weighted average bond distance. These are shown in Figure 11, and it is clear that the greatest interference results in the range of 3-6 Pd atoms within the 12-member first shell (Figure 11b). The analogous spectra generated at the Pd K-edge show that significant destructive interference exists for Re backscatterers about a Pd absorber at high Re:Pd ratios, i.e., 1:1 or greater (Figure 11a). A small fraction of Re about a Pd absorber only creates minimal destructive interference. Obviously, these are model calculations meant only to illustrate the phenomenon rather than provide detailed quantitative analysis.

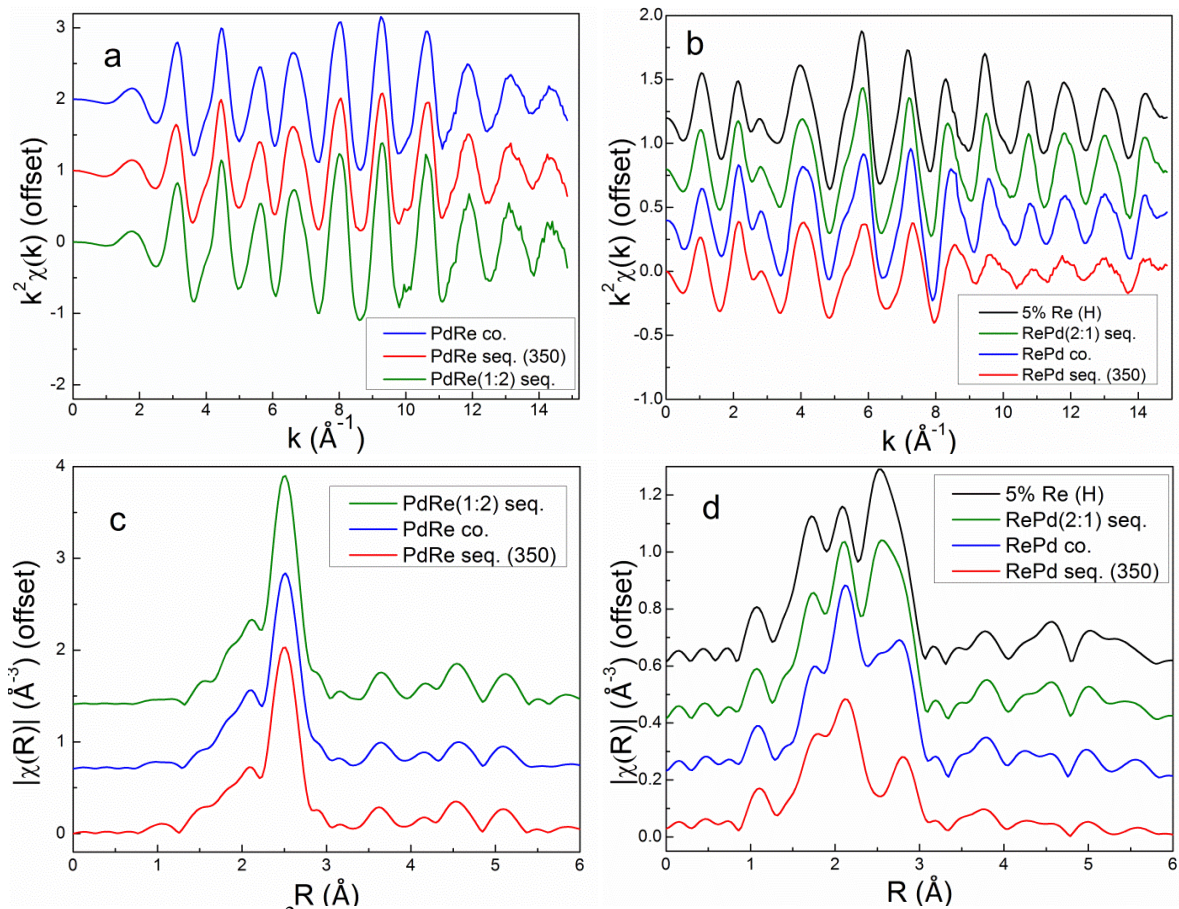


Figure 10. EXAFS (k^2 -weighting) of PdRe/Al₂O₃ catalysts at room temperature after 400°C reduction and He purge at a.) Pd K-edge and b.) Re L_{III}-edge EXAFS chi data c.) EXAFS Pd K FT magnitude (k -range: 2.5-14.1 \AA^{-1}), d.) Re L_{III} FT magnitude (k -range: 3.5-14.0 \AA^{-1}).

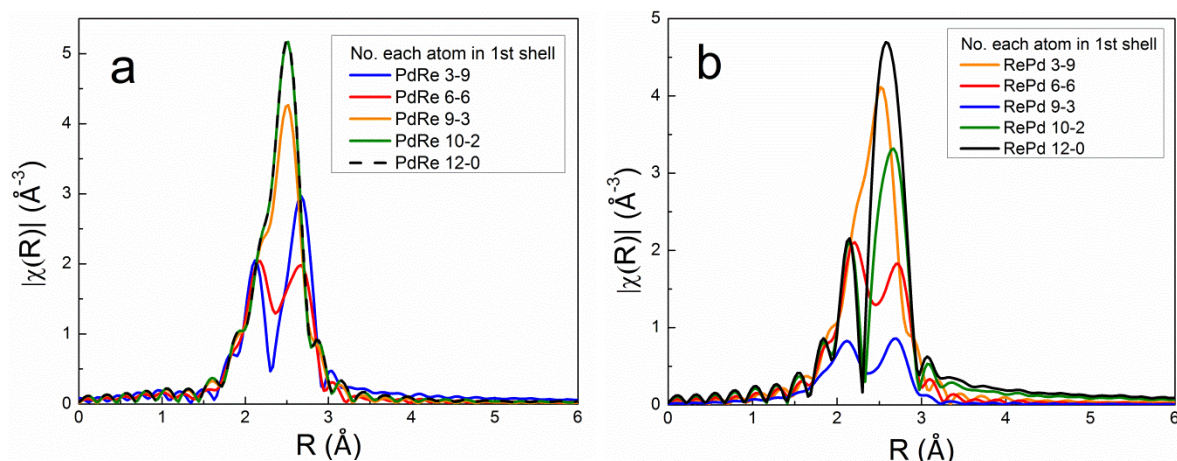


Figure 11. Fourier transforms of EXAFS spectra generated by substitution of one metal into the first coordination shell of the other a.) Re into Pd at the Pd K-edge and b.) Pd into Re at the Re L_{III}-edge. Each metal has twelve nearest neighboring atoms in its first coordination shell.

The Re L_{III} EXAFS spectra of the catalysts are complicated further by the presence of O backscatterers in the first coordination shell. The peak at $\sim 1.8 \text{ \AA}$ in the FT of 5% Re/Al₂O₃ is indicative of Re-O bonding, in agreement with the positive oxidation state evidenced by XANES. Qualitatively, the Re L_{III} FT EXAFS spectrum of RePd(2:1) seq. most closely resembles Re/Al₂O₃, consistent with the presence of segregated metallic Re species, as previously inferred from TPR/TPHD. The split between the peak at 2.2 \AA and the one at $2.8\text{-}2.9 \text{ \AA}$ widens and deepens in PdRe co. and even further in PdRe seq. (350). In addition, the latter peak is diminished relative to the former. The splitting is suggested to result from destructive interference as explained above. The estimated size of Re particles (or RePd particles), as judged by the magnitude of peaks resulting from higher coordination shells, i.e., features at $>3.5 \text{ \AA}$, are nearly the same for Re/Al₂O₃, RePd(1:2) seq. and RePd co. but smaller on average for RePd seq. (350).

Table 6. EXAFS fitting parameters following 400°C reduction and He purge (unless otherwise noted)

Path*	N	R (Å)	σ^2 (10^{-3} Å ²)	ΔE_0 (eV)	R-value
Re (H)					
Re-Re	7.2 ± 0.8	2.74 ± 0.01	8.0 ± 0.7	7.8 ± 1.5	0.027
Re-O	1.4 ± 0.2	2.01 ± 0.02	(5.0)	7.8 ± 1.5	
PdRe co.					
Pd-Pd	8.7 ± 0.4	2.73 ± 0.01	6.2 ± 0.3	2.3 ± 0.4	0.0053
Pd-Re	1.3 ± 0.2	2.71 ± 0.01	3.8 ± 0.9	2.3 ± 0.4	
Re-Re	6.5 ± 0.4	2.72 ± 0.01	6.6 ± 0.4	7.0 ± 0.8	0.0042
Re-Pd	1.3 ± 0.2	2.71 ± 0.01	3.8 ± 0.9	7.0 ± 0.8	
Re-O	0.7 ± 0.1	2.02 ± 0.01	(5.0)	7.0 ± 0.8	
RePd seq. (350) "as is"					
Re-O	4.0 ± 0.2	1.73 ± 0.01	(1.0)	9.3 ± 1.8	0.0094
PdRe seq. (350)					
Pd-Pd	8.3 ± 0.5	2.73 ± 0.01	6.4 ± 0.5	2.3 ± 0.4	0.0073
Pd-Re	0.8 ± 0.3	2.69 ± 0.02	3.5 ± 1.8	2.3 ± 0.4	
Re-Re	4.5 ± 1.0	2.71 ± 0.01	7.9 ± 1.5	8.0 ± 2.5	0.0022
Re-Pd	0.8 ± 0.3	2.69 ± 0.02	3.5 ± 1.8	8.0 ± 2.5	
Re-O	0.9 ± 0.3	2.03 ± 0.02	(5.0)	8.0 ± 2.5	
PdRe(1:2) seq.					
Pd-Pd	9.8 ± 1.2	2.73 ± 0.01	6.0 ± 0.8	2.6 ± 0.8	0.0048
Pd-Re	1.1 ± 0.6	2.70 ± 0.02	3.8 ± 3.0	2.6 ± 0.8	
Re-Re	6.8 ± 0.6	2.73 ± 0.01	6.9 ± 0.6	7.5 ± 1.1	0.017
Re-Pd	0.6 ± 0.3	2.70 ± 0.02	3.8 ± 3.0	7.5 ± 1.1	
Re-O	1.1 ± 0.2	2.01 ± 0.02	(5.0)	7.5 ± 1.1	

Pd K-edge fit range: k-space 2.7-14.0 Å⁻¹; R-space 1.0-3.0 Å

Re L_{III}-edge fit range: k-space 3.6-14.1 Å⁻¹; R-space 1.3-3.1 Å

*Values in parentheses were fixed

EXAFS fitting parameters are given in Table 6. The best-fit parameters for 5% Re/Al₂O₃ indicate a mixture of small metallic Re particles and ReO_x species. The average Re-O distance, 2.01 Å, suggests that Re⁴⁺ is most prevalent non-zero oxidation state after H₂ treatment at 400°C. Partial reduction of Re⁷⁺ to Re⁴⁺ has been observed in previous studies of Re/Al₂O₃ by electron spin resonance [51] and XPS [52]. A similar Re-O distance was also

found by Bare, et al. [23], and Chen, et al. [6]. Unlike the 0.7% Re/MOR-Al₂O₃ catalyst investigated by Bare, et al., adding a Re-O path with a bond distance corresponding to Re⁷⁺ (1.72 Å) did not substantially improve the statistics of the fit. TPR results indicate that the interaction of Re with the Al₂O₃ support becomes stronger at low Re loadings [28]. Far more of the H₂ uptake for 5% and 10% Re/Al₂O₃ catalysts occurs below 400°C than for the 1% Re/Al₂O₃ (Figure 12). This Re reduced at high temperature has been attributed to monatomic Re interacting strongly with the support, i.e., evidencing a Re-O-Al bond [23, 28].

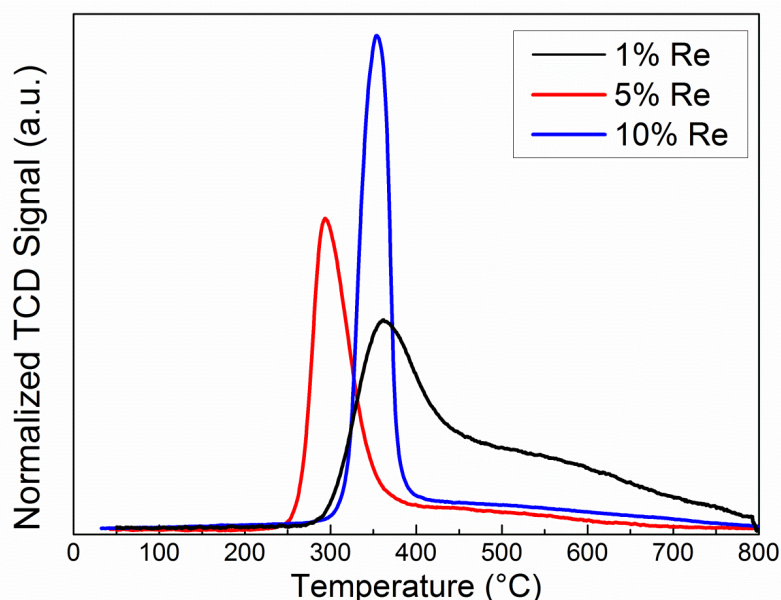


Figure 12. TPR profiles of Re/Al₂O₃ catalysts normalized by mol Re in sample to demonstrate inverse relationship between loading and amount of Re reduced >400°C. All catalysts were prepared using HReO₄ and calcining for 1 h at 350°C

Satisfactory simultaneous fits at the Pd K and Re L_{III} edges were obtained for the bimetallic catalysts using two homometallic backscattering paths (Pd-Pd and Re-Re), two heterometallic paths (Pd-Re and Re-Pd), and an Re-O path. Fits of the magnitude of the

Fourier transforms as well as their real portions and contributions from each FEFF path are shown in Figures 13-16. Debye-Waller factors were assigned for each homometallic bond and to the heterometallic bond. The D-W factor for Re-O was set to 0.005 \AA^2 . The Pd-Re CN was constrained to be equal to that of the Re-Pd CN multiplied by the molar ratio of Re to Pd in the catalyst, according to the Via criterion [53]. This ensures consistency in fitting the heterometallic bond from each edge.

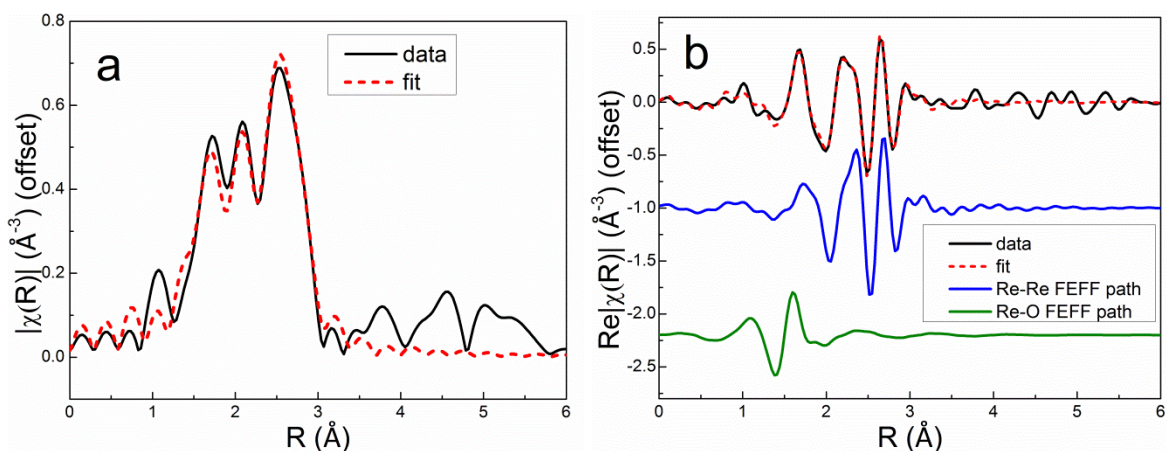


Figure 13. Data and fitting of 5% Re/Al₂O₃ (H) after reduction and He purge a.) Fourier transform magnitude and b.) Re L_{III}-edge real FT (offset)

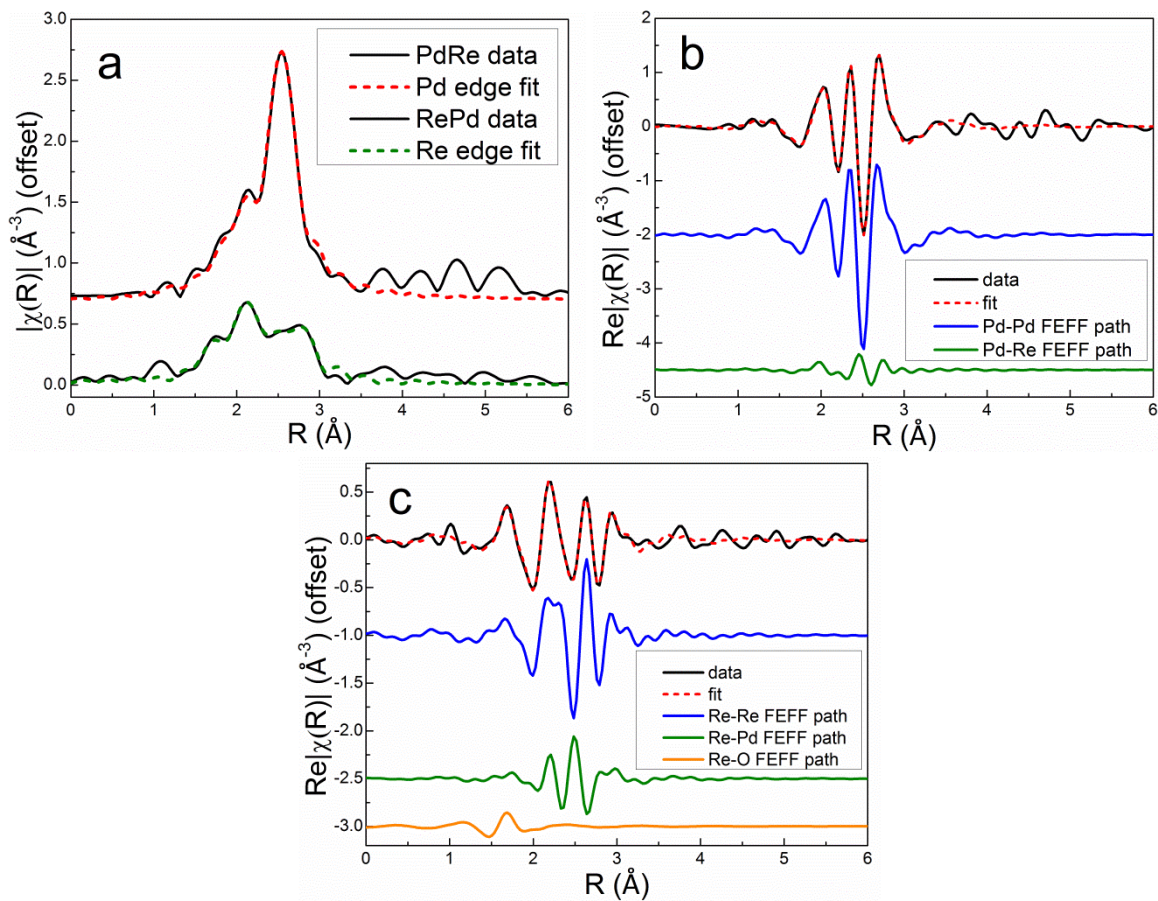


Figure 14. Data and fitting of PdRe/Al₂O₃ co. after reduction and He purge a.) Fourier transform magnitude, b.) Pd K-edge real FT, c.) Re L_{III}-edge real FT (offset)

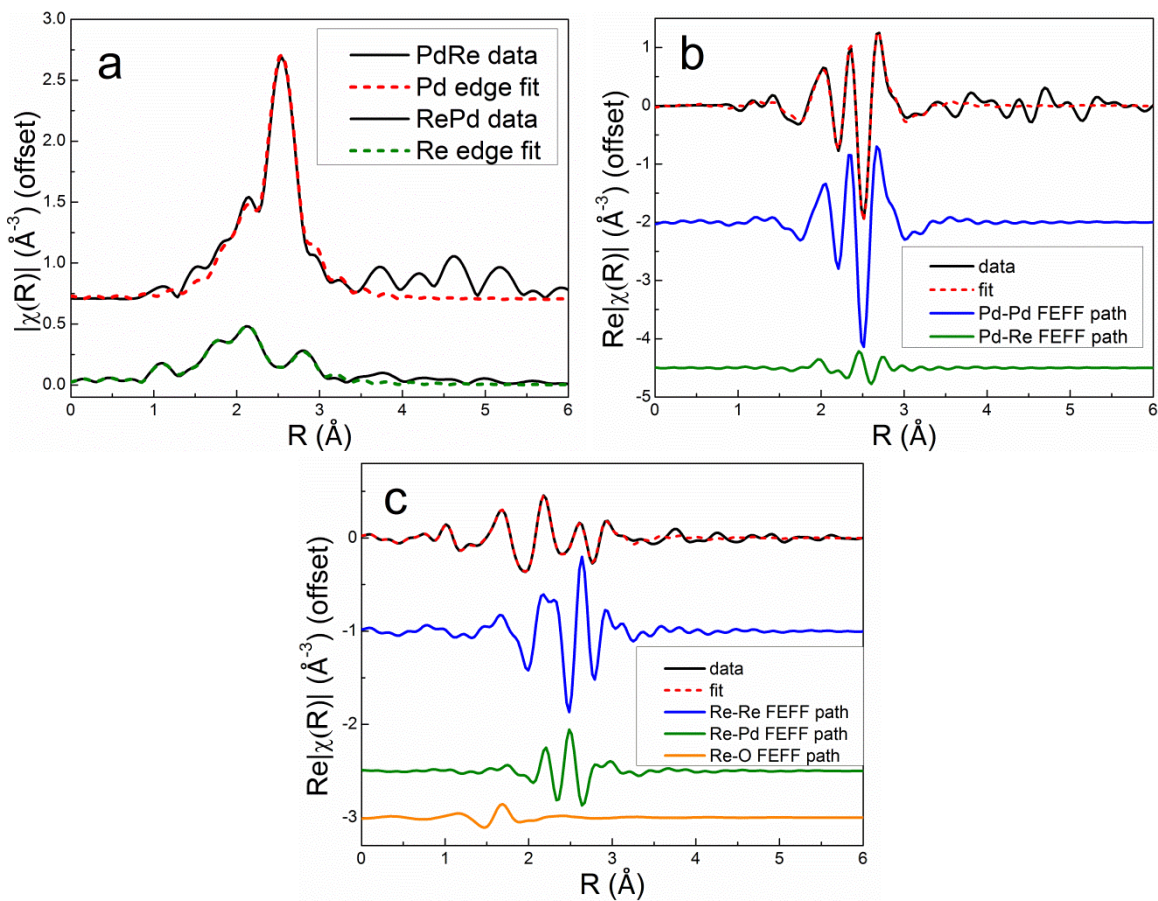


Figure 15. Data and fitting of PdRe/Al₂O₃ seq. (350) after reduction and He purge a.) Fourier transform magnitude and b.) Re L_{III}-edge real FT (offset)

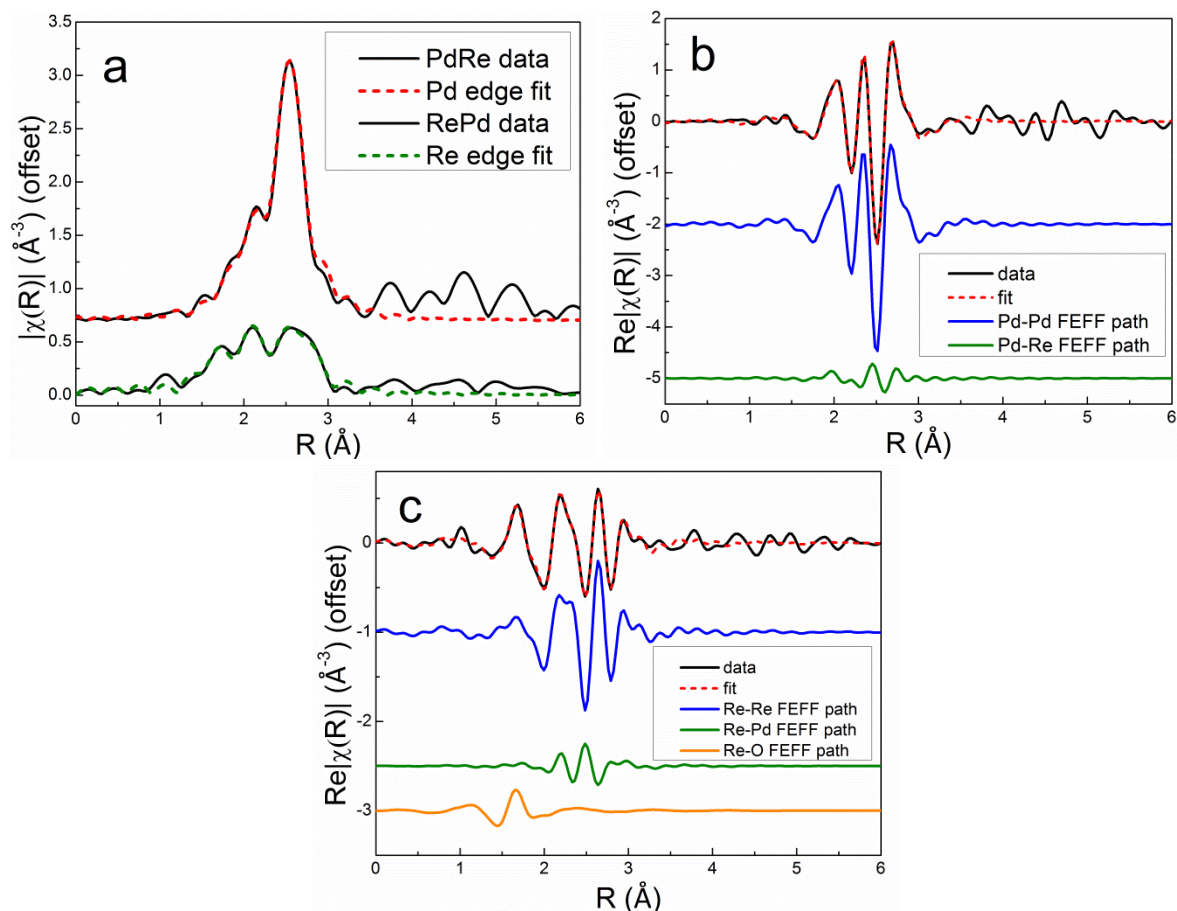


Figure 16. Data and fitting of PdRe(1:2)/Al₂O₃ seq. after reduction and He purge a.) Fourier transform magnitude, b.) Pd K-edge real FT, c.) Re L_{III}-edge real FT (offset)

Decreased metal particle size and increased Re-Pd destructive interference at the Re L_{III}-edge as described above is borne out in the fitting of the bimetallic catalysts. First, it should be noted that heterometallic CNs are less than homometallic CNs for all three catalysts, which implies the existence of segregated particles of each metal. Rhenium metal particles are largest in PdRe(1:2) seq., which has a total metal coordination number of 8.7, and smallest in PdRe seq. (350), 5.0. This contributes to the decreasing FT magnitudes in Figure 10d. The fit of PdRe(1:2) seq. suggests the least interference by the lowest ratio of

Re-Pd to Re-Re first shell coordination numbers, which is understood to contribute to the shape of the Fourier transforms, specifically the valley at ~ 2.6 Å. This ratio for the other two catalysts is double that of PdRe(1:2) seq. For all three PdRe catalysts, the metal-metal bond distances are reduced, in agreement with previous findings [9, 11]. Meitzner, et al. observed contraction of the Pd-Re and Re-Re bonds from their nominal value of 2.75 Å in both metals to 2.72 Å for Re-Re and 2.67 Å for Pd-Re [9]. Ziemecki, et al. used in situ XRD PdRe/Al₂O₃ during TPHD and observed two distinct alloy phases, both with contracted lattice parameters, 3.84 Å and 3.88 Å, as compared to 3.89 Å for the Pd fcc lattice [11]. These lattice parameters correspond to metal-metal bond distances of 2.71 and 2.73 Å, respectively, which are equivalent to the Pd-Re and Pd-Pd bond distances from EXAFS fitting. A short Pd-Re bond (relative to the metals) is also reported by Malinowski, et al. [15].

As evidenced by XANES, not all Re is reduced to metal, and this is reflected in the Re-O contributions. The bond length stays nearly constant at around 2.00 Å. As mentioned above for Re/Al₂O₃, adding a Re-O path with a bond length of 1.72 Å, which corresponds to the Re(VII) oxide bond length, did not improve the fit. A bond length of 2.00 Å is suggestive of the average of the nearest neighbor Re-O bond lengths in ReO₂ [54]. This Re-O bond length is similar to that used to fit Re L_{III}-edge spectra of RhRe-, PtRe-, and IrRe/SiO₂ catalysts [6, 25, 26]. If a second Re-O path is added and allowed to vary in bond length, the two bond lengths obtained are 1.91 Å and 2.08 Å, the Re-O distances in ReO₂. The Re-O CN varies according to the oxidation state suggested by XANES; Re (H) > PdRe(1:2) seq. > PdRe co. \approx PdRe seq. (350). A discrepancy arises, however, because of the bond length. Tetravalent Re has been described as a stable Re oxidation state for partially

reduced Re/Al₂O₃ catalysts [51]; however, the small CNs are insufficient to explain the putative oxidation state assigned by XANES. The electrostatic interaction of small Re particles with the support, i.e., cationic Re particles, has been posited by Bare, et al. [23], to explain higher-than-expected white line magnitudes in reduced Re/Al₂O₃-MOR. We infer that this interaction may explain the relatively high oxidation state suggested by XANES in spite of low coordination of Re with O in an ReO₂-like species.

Average Pd particle sizes based on palladium-metal CNs do not vary widely for these three catalysts. As expected based on chemisorption results, PdRe seq. (350) has the lowest Pd-metal coordination number (9.1), but this still implies an average particle size of >8 nm. The coordination number becomes much less sensitive above 10 for close-packed structures as the average particle size grows exponentially to the bulk value (12) [48]. Thus, for PdRe co. and PdRe(1:2) seq., which have Pd-metal CNs of 10.1 and 10.9, respectively, Pd particles are quite large on average.

3.7 HR-STEM-EDX Spectroscopy

The Pd particle sizes in the Pd (TA) and Pd (NO₃) catalysts, seen in STEM-HAADF images (Figure 17), conclusively demonstrate the large particles in Pd(NO₃). Figure 17a shows that there is a bimodal distribution of Pd particle sizes in Pd (TA), in agreement with the observation of two distinct peaks for bridging CO on Pd surface planes in CO DRIFTS. There are larger particles averaging 4-5 nm in size, and very small ~0.5 nm Pd particles all over the support, as indicated in the image. Palladium particles in Pd (NO₃) are primarily > 10 nm in diameter, with many larger (≥20 nm) particles visible (Figure 17b). Rhenium particles in 5% Re (H) exhibit a distribution of sizes similar to that of Pd particles in Pd

(TA). The largest particles observed are 3-4 nm in size (Figure 18). Much smaller particles are spread over the support, <1 nm in diameter. These small Re particles (also in Figure 18) are expected to be more influenced by interaction with the support; i.e., have induced charge from or bond directly to the Al_2O_3 support [23].

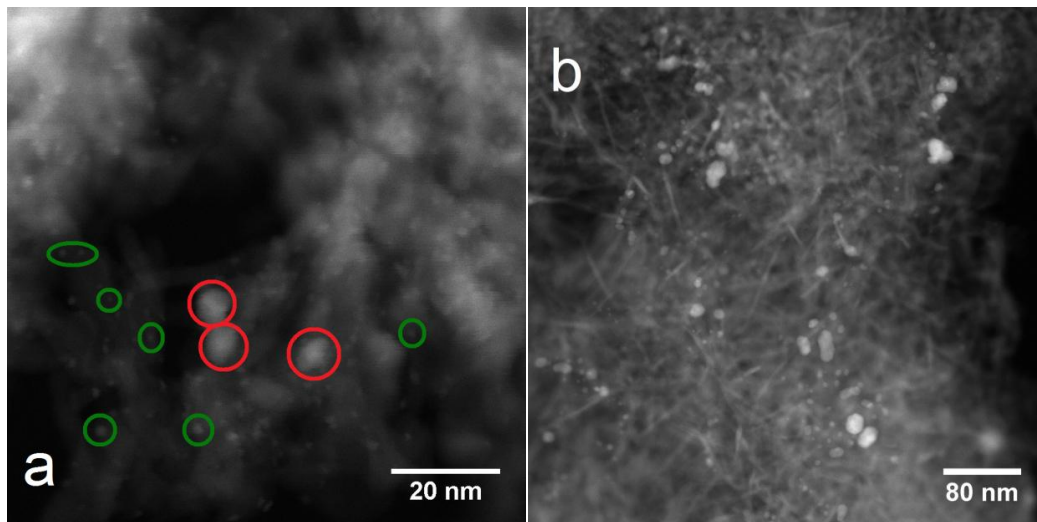


Figure 17. HAADF-STEM images of Pd/ Al_2O_3 a.) Pd (TA): larger particles outlined in red, smaller in green and b.) Pd (NO_3)

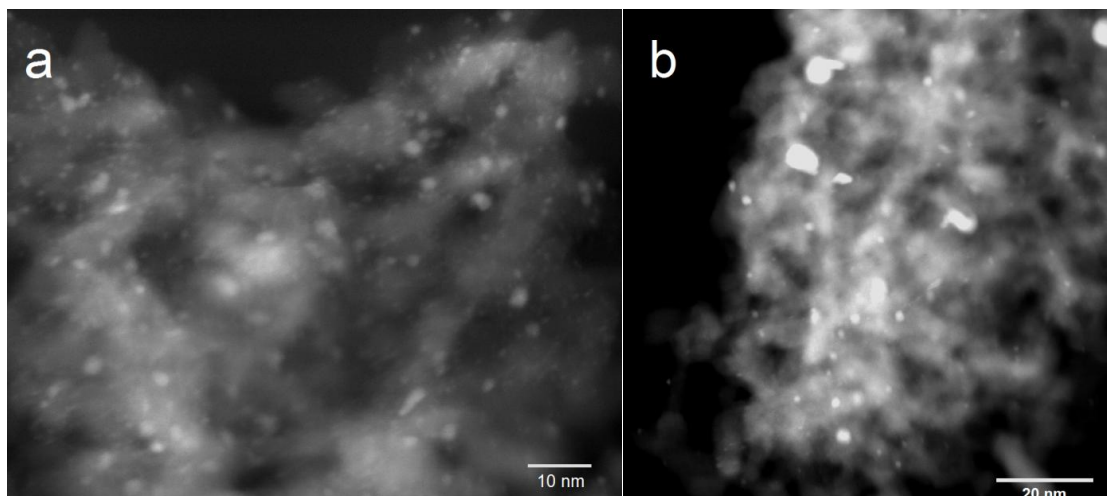


Figure 18. HAADF-STEM images of Re/ Al_2O_3 (H)

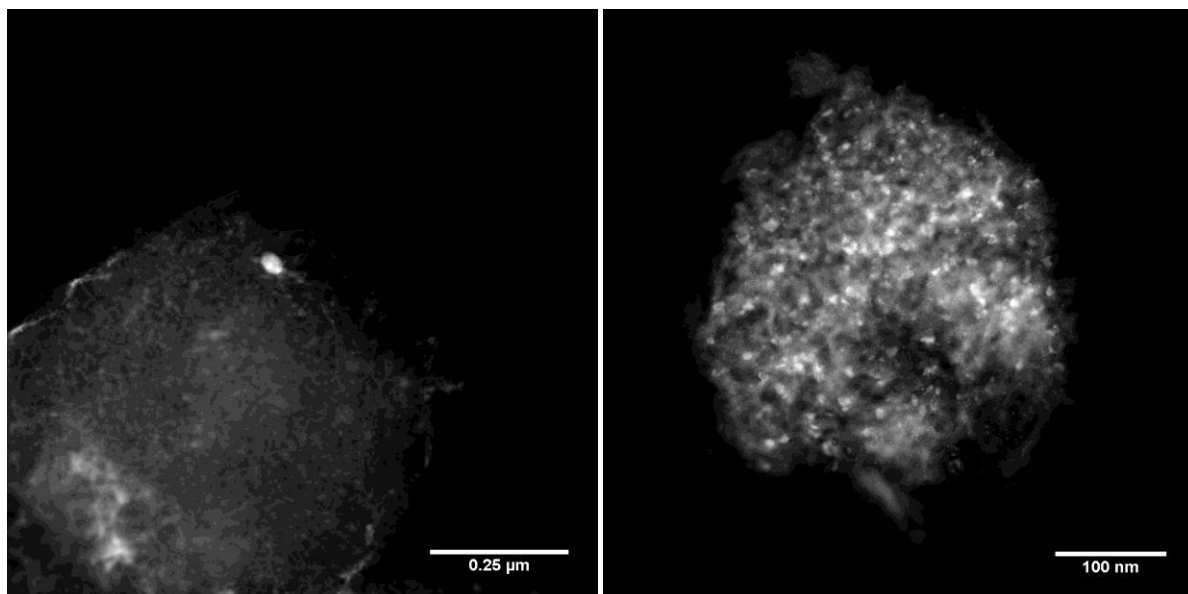


Figure 19. Low magnification HAADF-STEM comparison of PdRe/Al₂O₃ a.) typical Al₂O₃ particles of PdRe co. and b.) PdRe seq. (350)

The Pd-rich particles in 1:1 bimetallic catalysts vary in size based on the Pd precursor employed, i.e., PdRe co. and Re-Pd⁰ seq., both prepared with Pd(NO₃)₂ and PdRe seq. Figure 19a shows one large Pd particle and thick Pd formations around the edge of an Al₂O₃ particle in PdRe co. No such large metal particles are observed in PdRe seq. (350) in Figure 19b, but instead, there is an even distribution of smaller particles of both metals. High-resolution EDX spectroscopy images show Pd-Re contact in all bimetallic catalysts by the appearance of yellow pixels (superposition of green and red pixels), in agreement with the heterometallic contribution observed in EXAFS spectra (Figures 20-23). The contact appears to be primarily surface contact between small Re particles and Pd particles. We have observed this morphology previously in a PdRe/C catalyst prepared by co-impregnation (Chapter 1). The superposition of Pd and Re signals is most clear in Figures 20 and 21 for

the bimetallic catalysts prepared from $\text{Pd}(\text{NO}_3)_2$. In Figure 21, there appears to be a grouping of 10-20 nm Pd particles covered by Re. There are some distinguishable Re particles 3-5 nm in diameter, but a lot of it is more diffuse (Figures 20b and 21b). In particular, PdRe co. shows the highest yellow pixel density of any of the catalysts. This may indicate Re alloying in these Pd particles, as evidenced by the lack of a strong desorption feature at $\sim 50^\circ\text{C}$ in TPHD. For Re-Pd⁰ seq., there are certainly some Re particles making contact with the Pd particle. In fact, there is a clear Re particle outline of the large red Pd particle below and to the right of center of Figure 21c, similar to that illustrated by Tapin, et al. [18]. Palladium hydride formation is substantially suppressed in this catalyst as well, in agreement with Ziemecki's findings [10]. There is also a paucity of Re in between this Pd particle and the others in the top left and right of the image. A likely explanation for this morphology is migration of ReO_x species to Pd particles during reduction. Because this catalyst was not calcined following impregnation with perrhenic acid, the interaction of $[\text{ReO}_4]^-$ with Al_2O_3 should be minimized. The mobility of oxidic Re(VII) species across the support is greatest for catalysts which have not been dried at high temperature, and minimized for the calcined catalysts [10]. A more even distribution of Re is indeed observed for PdRe co., and particularly for the sequentially prepared catalysts in Figures 22 and 23.

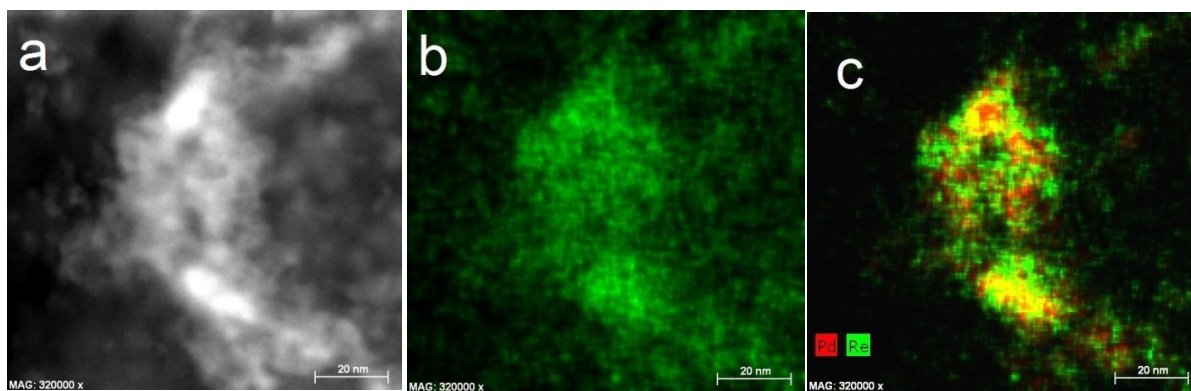


Figure 20. STEM images of PdRe/Al₂O₃ co. a-b.) HAADF-STEM and c.) STEM-EDX (20 nm scale bar); red – Pd, green – Re, yellow – superposition

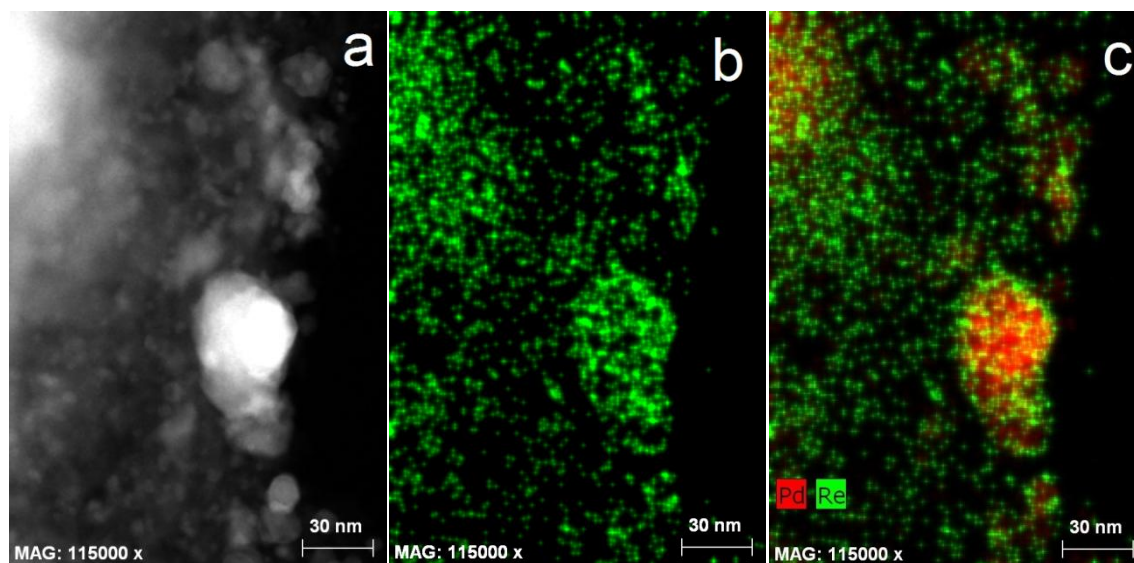


Figure 21. STEM-EDX images of Re-Pd⁰ seq. catalyst a.) HAADF-STEM, b.) Re STEM-EDX and c.) composite –EDX (30 nm scale bar); red – Pd, green – Re, yellow – superposition

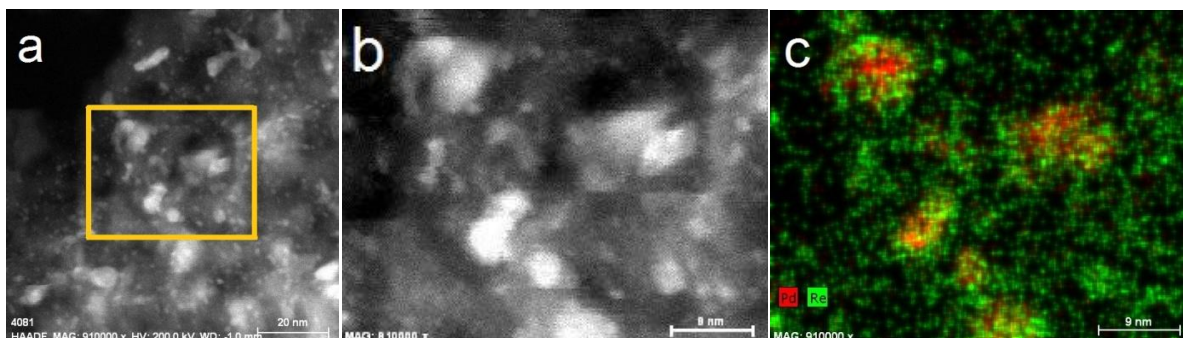


Figure 22. STEM images of PdRe/Al₂O₃ seq. (350) a-b.) HAADF-STEM and c.) STEM-EDX (9 nm scale bar); red – Pd, green – Re, yellow – superposition

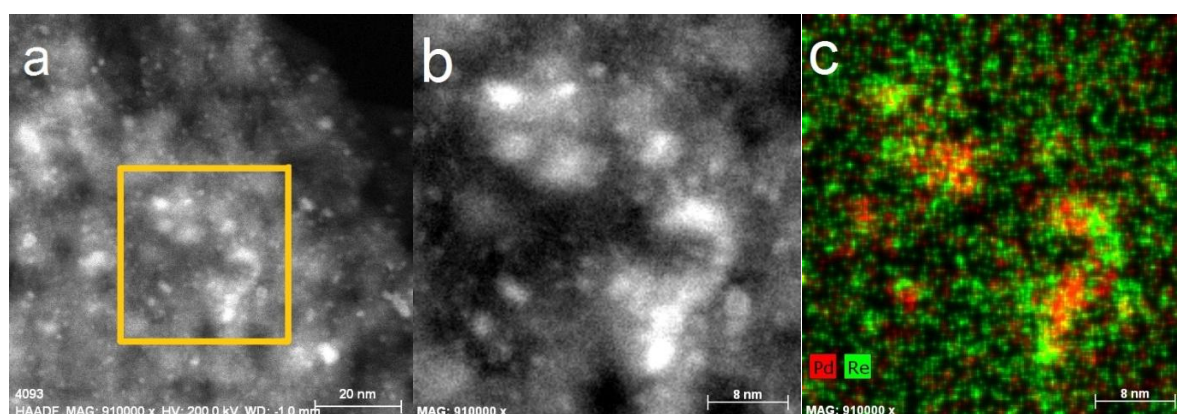


Figure 23. STEM images of PdRe/Al₂O₃ seq. (400) a-b.) HAADF-STEM and b.) STEM-EDX (8 nm scale bar); red – Pd, green – Re, yellow – superposition

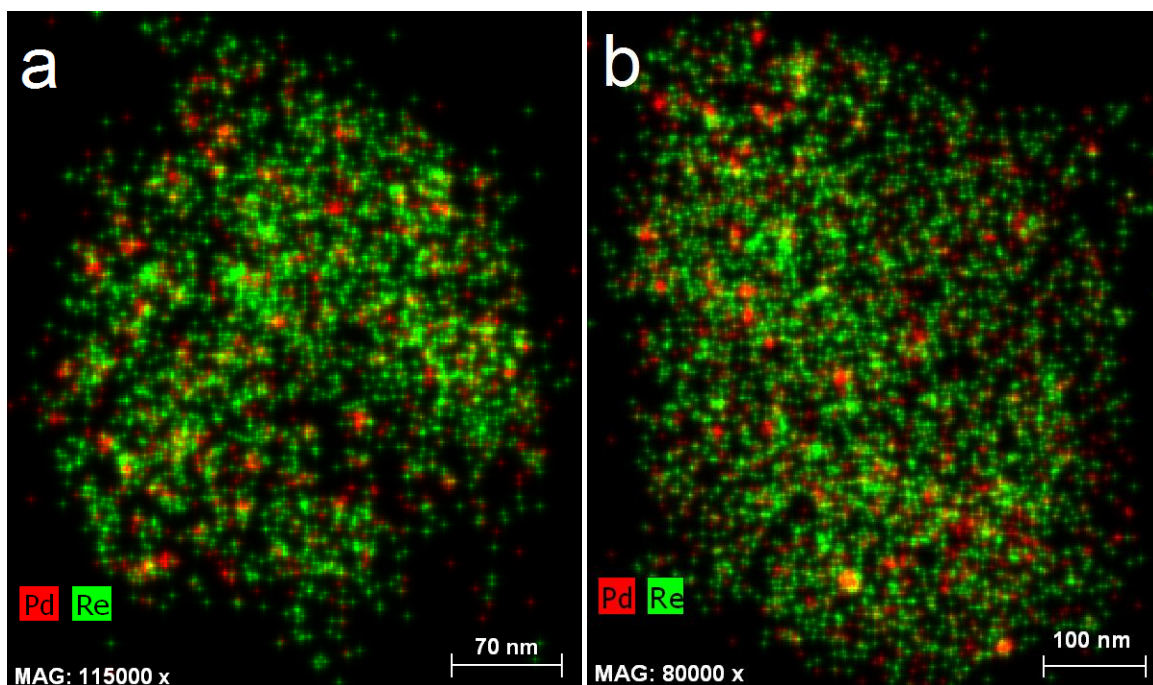


Figure 24. STEM-EDX images of a.)PdRe seq. (350) and b.) PdRe seq. (400); red – Pd, green – Re, yellow – superposition

PdRe seq. (350) and –(400) are nearly indistinguishable by STEM-EDX. The distribution of metal particles within typical Al_2O_3 particles is virtually the same (Figure 24). The high-resolution images both show ≤ 8 nm Pd particles in contact with Re with more diffuse signal from Re on the Al_2O_3 support, perhaps from smaller Re particles as observed in $\text{Re}/\text{Al}_2\text{O}_3$. The findings of H_2 and CO chemisorption, CO DRIFTS and TPR/TPHD all suggest the similarity of the PdRe(1:1) seq. catalysts. In the PdRe(1:2) seq. catalyst, a non-uniform distribution of large Pd particles is evident in the micrographs (not shown). There are Pd-rich regions with very large particles (20-50 nm), while Re, present in twice the molar quantity, evenly coats the Al_2O_3 support and Pd particles. The observed structure suggests that in spite of the $\text{Pd}(\text{NH}_3)_4(\text{NO}_3)_2$ precursor used to prepare it, large Pd particles form.

Because the Pd was added to calcined Re/Al₂O₃, using high pH during preparation may not impart charge to the Al₂O₃ to give rise to strong electrostatic adsorption and even Pd distribution. It has been demonstrated that ReO₄⁻ tetrahedra will spread to cover the Al₂O₃ surface during calcination. At this higher loading (10% Re), a high proportion of the Al₂O₃ is expected to be terminated by Al-O-(ReO₃) species [55].

4 Conclusions

- Hydrogenation chemoselectivity is improved by contact of small Re particles with the surface of Pd particles.
- Suppression of H₂ chemisorption at 35°C evidences Re coverage of Pd particles. The proximity of Re particles with the surface of Pd particles can be seen clearly by HR-STEM-EDX analysis.
- Alloy formation is supported by Pd-Re bonding observed in EXAFS spectroscopy and the suppression of β-PdH_x formation in TPHD.
- Catalysts with an equimolar Pd-Re ratio produced by sequential impregnation are the most active in furfural hydrogenation, superior to monometallic catalysts and to PdRe co.
- Increased Re content leads to higher Pd coverage and higher FAL selectivity, but results in the formation of large Pd particles, which is deleterious to the rate of furfural consumption over this catalyst.

5 Acknowledgements

This work was funded by Eastman Chemical Company for funding through the Center of Excellence. ICP-OES analysis was performed by Eastman Chemical Company. This research used resources of the Advanced Photon Source, a U.S. Department of Energy (DOE) Office of Science User Facility operated for the DOE Office of Science by Argonne National Laboratory under Contract No. DE-AC02-06CH11357. We gratefully acknowledge the loan of EXAFS equipment from Dr. Jeffrey Miller, and the assistance of Dr. Joshua Wright and Dr. John Katsoudas in operating beamline MR-CAT-10BM. The authors acknowledge the use of the Analytical Instrumentation Facility at NCSU, which is supported by the State of North Carolina and the National Science Foundation, and, in particular, Dr. Xiahan Sang for assistance with STEM-EDX.

References

- [1] N.E. Raymond, P.I. Angelo, in: Masonite Corporation, United States Patent 2538302, 1951.
- [2] S. Sitthisa, D.E. Resasco, *Catal. Lett.*, **141** (2011) 784-791.
- [3] S. Sitthisa, T. Pham, T. Prasomsri, T. Sooknoi, R.G. Mallinson, D.E. Resasco, *J. Catal.*, **280** (2011) 17-27.
- [4] S. Sitthisa, T. Sooknoi, Y.G. Ma, P.B. Balbuena, D.E. Resasco, *J. Catal.*, **277** (2011) 1-13.
- [5] M. Chia, Y.J. Pagan-Torres, D. Hibbitts, Q.H. Tan, H.N. Pham, A.K. Datye, M. Neurock, R.J. Davis, J.A. Dumesic, *J. Am. Chem. Soc.*, **133** (2011) 12675-12689.
- [6] K.Y. Chen, S. Koso, T. Kubota, Y. Nakagawa, K. Tomishige, *Chemcatchem*, **2** (2010) 547-555.
- [7] B. Predel, O.E. Madelung, in: Landolt-Börnstein - Group IV Physical Chemistry, SpringerMaterials.
- [8] E.M. Savitskii, V.P. Tsyganova, M.A. Tylkina, *Izv. Akad. Nauk SSSR, Neorg. Mater.*, **7** (1962) 1917.
- [9] G. Meitzner, G.H. Via, F.W. Lytle, J.H. Sinfelt, *J. Chem. Phys.*, **87** (1987) 6354-6363.
- [10] S.B. Ziemecki, G.A. Jones, J.B. Michel, *J. Catal.*, **99** (1986) 207-217.
- [11] S.B. Ziemecki, J.B. Michel, G.A. Jones, *React. Solid.*, **2** (1986) 187-202.
- [12] M. Kitson, P.S. Williams, in: U.S.P. Office (Ed.), The British Petroleum Company, United States Patent 5149680, 1992.
- [13] M.A. Mabry, W.W. Prichard, S.B. Ziemecki, in: U.S.P. Office (Ed.), E. I. du Pont de Nemours and Company, United States Patent 4550185, 1985.
- [14] M. Bonarowska, A. Malinowski, Z. Karpinski, *App. Catal. A*, **188** (1999) 145-154.
- [15] A. Malinowski, W. Juszczuk, M. Bonarowska, J. Pielaszek, Z. Karpinski, *J. Catal.*, **177** (1998) 153-163.
- [16] W. Juszczuk, Z. Karpinski, *App. Catal. A*, **206** (2001) 67-78.

- [17] B.K. Ly, D.P. Minh, C. Pinel, M. Besson, B. Tapin, F. Epron, C. Especel, *Top. Catal.*, **55** (2012) 466-473.
- [18] B. Tapin, F. Epron, C. Especel, B.K. Ly, C. Pinel, M. Besson, *Catal. Today*, **235** (2014) 127-133.
- [19] M.P. Latusek, B.P. Spigarelli, R.M. Heimerl, J.H. Holles, *J. Catal.*, **263** (2009) 306-314.
- [20] M.D. Skoglund, J.H. Holles, *Catal. Lett.*, **143** (2013) 966-974.
- [21] V. Pallassana, M. Neurock, L.B. Hansen, B. Hammer, J.K. Norskov, *Phys. Rev. B*, **60** (1999) 6146-6154.
- [22] V. Pallassana, M. Neurock, L.B. Hansen, J.K. Norskov, *J. Chem. Phys.*, **112** (2000) 5435-5439.
- [23] S.R. Bare, S.D. Kelly, F.D. Vila, E. Boldingh, E. Karapetrova, J. Kas, G.E. Mickelson, F.S. Modica, N. Yang, J.J. Rehr, *J. Phys. Chem. C*, **115** (2011) 5740-5755.
- [24] S. Koso, H. Watanabe, K. Okumura, Y. Nakagawa, K. Tomishige, *J. Phys. Chem. C*, **116** (2012) 3079-3090.
- [25] Y. Amada, H. Watanabe, M. Tamura, Y. Nakagawa, K. Okumura, K. Tomishige, *J. Phys. Chem. C*, **116** (2012) 23503-23514.
- [26] T. Ebashi, Y. Ishida, Y. Nakagawa, S.-i. Ito, T. Kubota, K. Tomishige, *J. Phys. Chem. C*, **114** (2010).
- [27] Y. Takeda, Y. Nakagawa, K. Tomishige, *Catal. Sci. Tech.*, **2** (2012) 2221-2223.
- [28] F.D. Hardcastle, I.E. Wachs, J.A. Horsley, G.H. Via, *J. Mol. Catal.*, **46** (1988) 15-36.
- [29] D.S. Kim, I.E. Wachs, *J. Catal.*, **141** (1993) 419-429.
- [30] B. Mitra, X.T. Gao, I.E. Wachs, A.M. Hirt, G. Deo, *Phys. Chem. Chem. Phys.*, **3** (2001) 1144-1152.
- [31] M.A. Vuurman, I.E. Wachs, *J. Phys. Chem.*, **96** (1992) 5008-5016.
- [32] J. Okal, *App. Catal. A*, **287** (2005) 214-220.
- [33] E. Bus, J.T. Miller, A.J. Kropf, R. Prins, J.A. van Bokhoven, *Phys. Chem. Chem. Phys.*, **8** (2006) 3248-3258.
- [34] M. Newville, *J. Synch. Rad.*, **8** (2001) 322-324.

- [35] B. Ravel, M. Newville, *J. Synch. Rad.*, **12** (2005) 537-541.
- [36] B. Ravel, *J. Synch. Rad.*, **8** (2001) 314-316.
- [37] C. Kittel, Introduction to Solid State Physics, J. Wiley & Sons, Inc., 5th ed., 1996, pp. 23.
- [38] G.J. Kruger, E.C. Reynhardt, *Acta Crystall.*, **34** (1978) 259-261.
- [39] L. Jiao, J.R. Regalbuto, *J. Catal.*, **260** (2008) 329-341.
- [40] F. Solymosi, T. Bansagi, *J. Phys. Chem.*, **96** (1992) 1349-1355.
- [41] J. Okal, L. Kepinski, L. Krajczyk, W. Tylus, *J. Catal.*, **219** (2003) 362-371.
- [42] G.W. Chadzynski, H. Kubicka, *Thermochim. Acta*, **158** (1990) 353-367.
- [43] O.S. Alexeev, B.C. Gates, *Ind. Eng. Chem. Res.*, **42** (2003) 1571-1587.
- [44] N.A. Bhole, M.T. Klein, K.B. Bischoff, *Ind. Eng. Chem. Res.*, **29** (1990) 313-316.
- [45] G. Agostini, R. Pellegrini, G. Leofanti, L. Bertinetti, S. Bertarione, E. Groppo, A. Zecchina, C. Lamberti, *J. Phys. Chem. C*, **113** (2009) 10485-10492.
- [46] T. Lear, R. Marshall, J.A. Lopez-Sanchez, S.D. Jackson, T.M. Klapotke, M. Baumer, G. Rupprechter, H.J. Freund, D. Lennon, *J. Chem. Phys.*, **123** (2005) 13.
- [47] W. Daniell, T. Weingand, H. Knozinger, *J. Mol. Catal. A*, **204** (2003) 519-526.
- [48] J.A. McCaulley, *J. Phys. Chem.*, **97** (1993) 10372-10379.
- [49] G. Fagherazzi, A. Benedetti, S. Polizzi, A. Dimario, F. Pinna, M. Signoretto, *Catal. Lett.*, **32** (1995) 293-303.
- [50] M. Boudart, H.S. Hwang, *J. Catal.*, **39** (1975) 44-52.
- [51] M.S. Nacheff, L.S. Kraus, M. Ichikawa, B.M. Hoffman, J.B. Butt, W.M.H. Sachtler, *J. Phys. Chem. C*, **106** (1987) 263-272.
- [52] J. Okal, W. Tylus, L. Kepinski, *J. Catal.*, **225** (2004) 498-509.
- [53] G.H. Via, K.F. Drake, G. Meitzner, F.W. Lytle, J.H. Sinfelt, *Catal. Lett.*, **5** (1990) 25-33.

[54] A. Magneli, *Acta Chem. Scand.*, **11** (1957) 28-33.

[55] J.A. Moulijn, J.C. Mol, *J. Mol. Catal.*, **46** (1988) 1-14.

CHAPTER 3: PREPARATION OF PdRe/Al₂O₃ CATALYSTS: CHARACTERIZATION BY RAMAN, TPR, XAFS AND STEM-EDX

Abstract

PdRe/Al₂O₃ catalyst morphology depends strongly on the Pd precursor and the mode of metal addition to the Al₂O₃ support. Catalysts were prepared by co-impregnation (PdRe co.), Re addition to reduced and passivated Pd/Al₂O₃ (Re-Pd⁰ seq.) and sequential impregnation with calcination after each impregnation step (PdRe seq.). Raman spectra of the as-prepared catalysts (calcined and/or before final reduction) evidence large PdO particles in catalysts derived from Pd(NO₃)₂; smaller PdO crystallites are observed in catalysts prepared from Pd(NH₃)₄(NO₃)₂. Large PdO particles give rise to sharp H₂ uptake at low temperature. Because of the uneven distribution of Pd⁰, spillover hydrogen must diffuse further to Re, and Re is not reduced until higher temperatures. Small PdO particles, which are more well-distributed, are reduced more gradually and do not sinter significantly. These Pd⁰ particles facilitate Re reduction in bimetallics (shift of ~300°C compared to Re/Al₂O₃). Both T_d [ReO₄]⁻ and C_{3v} [ReO₄]⁻ symmetries are observed in bimetallic catalysts, in spite of exposure to ambient moisture, which is inferred to arise from PdO-[ReO₄] interaction. Following reduction at 400°C, Pd particles in Pd(NO₃)₂-derived catalysts are predominantly large (>10 nm), as evidenced by extended x-ray absorption fine structure (EXAFS) spectroscopy, scanning-transmission electron microscopy (STEM) with energy-dispersive x-ray (EDX) imaging and CO diffuse reflectance infrared Fourier transform spectroscopy

(DRIFTS). The surface contact of Re and Pd-rich particles in all three catalysts leads to suppression of H₂ chemisorption. Interaction between Pd and Re on the surface of smaller Pd particles in PdRe seq. and Re-Pd⁰ seq. results in increased furfural and furfuryl alcohol (FAL) turnover frequencies (TOF).

1 Introduction

Rhenium has been employed for decades in PtRe/Al₂O₃ catalysts for naphtha reforming [1-3], and initial interest in PdRe catalysts appears to have evolved from contemporaneous studies of PtRe/Al₂O₃ [4]. Recently, Re has gained significant attention in combination with other Group VIII metals such as Rh [5-8], Ru [9, 10] and Pd [11] to improve selectivity in hydrogenation and hydrogenolysis of oxygenated organic compounds. Tomishige, et al., have extensively studied SiO₂- and C-supported bimetallics for reactions such as ester hydrogenolysis [6], ring-opening of cyclic ethers [5, 8], hydrogenation of fatty acids to alcohols [11], and glycerol hydrogenolysis [12]. In each case, Re addition boosts activity and selectivity towards the desired product, e.g., 1,5-pentanediol from ring-opening of tetrahydrofurfuryl alcohol [8]. As mentioned, addition of Re to Pd/SiO₂ increased selectivity to fatty alcohols from fatty acids [11]. PdRe bimetallic catalysts have also been used to promote water-gas shift activity [13, 14], selective hydrogenation of dicarboxylic acids [15-17], dechlorination [18-21], and reforming reactions [22]. Extended x-ray absorption fine structure (EXAFS) spectra of RhRe/SiO₂ evidence Re coordination to O, Rh and Re. The suppression of CO chemisorption compared to Rh/SiO₂ and the modification of catalytic activity suggest surface interaction of Re species with pre-formed Rh particles. In

conjunction with results from x-ray photoelectron spectroscopy (XPS), x-ray diffraction, scanning transmission electron microscopy with energy-dispersive x-ray analysis (STEM-EDX) and EXAFS, they conclude that low valence ReO_x species covering the surface of Rh particles are responsible for catalytic activity [8, 23]. Dumesic, et al., have also investigated Re-promoted noble metal catalysts, including PtRe/C for glycerol hydrogenolysis [24-26] and RhRe/C for cyclic ether hydrogenolysis [7, 27]. Their findings suggest bimetallic particle formation, in particular evidence of mixed Pt-Re surfaces, which leads to enhancement of water-gas shift activity in PtRe/C [24, 25]. It was concluded that the acidity of Re-O-H species was responsible for the promotional effect on RhRe/C in cyclic ether hydrogenolysis in an aqueous reaction environment [7].

By comparison, the study of PdRe catalysts, in particular their structures, has been limited. The inferred PdRe catalyst morphology has varied widely depending on the catalyst preparation method and catalyst loading. The methods, precursors and nominal metal loadings of some PdRe catalysts described in the literature are given in Table 1. Meitzner, et al., demonstrated that Pd-Re alloying was evident from EXAFS spectra of a 0.6% Pd-1% Re/ Al_2O_3 catalyst prepared by incipient wetness (IW) co-impregnation [4]. Many of the other PdRe catalysts were prepared by sequential impregnation, where the two metal precursors are added separately, sometimes with intervening calcination and/or reduction of the first supported metal. Ziemecki, et al., published several papers and patents describing PdRe/ Al_2O_3 [28, 29] and PdRe/C [16] catalysts prepared by depositing a Pd salt, calcining, reducing and passivating, and then adding the Re precursor. These patents claim that the presence of a Group I or IIa metal, such as Na, has a beneficial effect on catalytic activity

[16]. Investigation by temperature-programmed reduction (TPR) and temperature-programmed hydride decomposition (TPHD), in particular with in situ XRD, demonstrated that substitutional alloying of Re in Pd-rich particles was responsible for the suppression of PdH_x formation. Several papers by Karpinski, et al. [18, 19, 22], based on a similar catalyst preparation method, report similar results to those found by Ziemecki with regards to PdH_x suppression. The addition of small amounts of Re to Pd/Al₂O₃ suppresses hydroisomerization activity and chemisorption of CO; thus, they conclude that most Re occupies the surface of Pd-rich particles [19]. More recently, attempts at encouraging surface contact of the two metals using catalytic reduction [15] to deposit Re selectively on Pd particles, and an "overlayer" approach involving acetylacetonate ions for selectively depositing Pd on Re particles has been reported [30, 31].

Table 1. Summary of supported PdRe catalyst preparation from the literature

Preparation method	Pd precursor	Re precursor	Pd loading (wt%)	Re loading (wt%)	Source
Co-impregnation					
IW co-impregnation, calcined 500°C for 3 h	Pd(NO ₃) ₂	HReO ₄	0.6	1	[4]
Sequential IW					
Re added to passivated Pd ⁰ /Al ₂ O ₃	H ₂ PdCl ₄	Re ₂ O ₇	3	3	[28]
	Pd(NO ₃) ₂	NH ₄ ReO ₄	2	0.2-9.5	[18]
IW with Pd, calcined 500°C 3 h, IW with Re, then repeat calcination	PdCl ₂	NH ₄ ReO ₄	1	14	[11]
IW of TiO ₂ with Re, dry, IW with Pd and calcine 500°C 1 h	Pd(NO ₃) ₂	NH ₄ ReO ₄	1	10	[13]
Selective Deposition					
Catalytic reduction – Re solution added to Pd ⁰ /TiO ₂ in inert atmosphere	H ₂ PdCl ₄	NH ₄ ReO ₄ + HCl	2	0.9	[15]
Pd(acac) ₂ added to Re ⁰ /Al ₂ O ₃ in toluene; calcined 400°C 4 h	Pd(acac) ₂	NH ₄ ReO ₄	0.1	2-7	[31]

Our previous results show that there are substantial differences in catalyst behavior depending on the method of preparation, precursors, and Pd:Re ratio (see Chapter 2). We observed that there was strong correlation between suppression of H₂ chemisorption and furfural hydrogenation activity, and we attributed the suppression of H₂ chemisorption to Re coverage of Pd particles. A 1:2 molar ratio sequentially prepared catalyst with large Pd particles exhibits the greatest degree of H₂ chemisorption suppression but also very low activity. This may suggest that there is an optimum in Re coverage of Pd, and if too much Pd surface area is blocked by Re, then the catalytic activity suffers. The current work seeks to explain the observed activity in furfural hydrogenation based on catalyst structure, i.e., metal-

metal interaction and particle size, suggested by CO and H₂ chemisorption, CO diffuse reflectance infrared Fourier transform spectroscopy (DRIFTS), EXAFS and STEM-EDX. Furthermore, we seek to understand the role of metal precursors, calcination conditions and metal-Al₂O₃ interaction throughout the course of three preparation methods, all using a nominal 1:1 Pd:Re molar ratio. In particular, we take advantage of the strong Raman bands of the perrhenate ion, [ReO₄]⁻, and PdO in order to characterize calcined or "as prepared" catalysts.

There has been extensive study of Re/Al₂O₃ catalysts by Raman spectroscopy, in particular by Wachs, et al. [32-34]. The perrhenate ion, ReO₄⁻, has a very strong Raman band, the symmetric Re-O stretch, $\nu_3(\text{Re-O})$. Furthermore, its local chemical environment changes the position of the band, from a tetrahedral (T_d) geometry in solution to a lower symmetry C_{3v} geometry when one oxygen forms a bridge with the Al₂O₃ support [32, 34]. Because of the opacity of PdO to visible light, few groups have characterized supported catalysts using Raman spectroscopy [35]. Otto, et al., successfully measured a series of Pd/Al₂O₃ catalysts and Pd black/Al₂O₃ and learned that there is a linear relationship between the intensity of the main signal in PdO (B_{1g} lattice vibration) and catalyst loading up to 2.5% Pd/Al₂O₃ [36]. Baylet, et al. [37], and Su, et al. [38], used *in situ* Raman spectroscopy during temperature-programmed reactions (reduction, decomposition, oxidation) to investigate the dynamics of Pd/Al₂O₃ and Pd/ZrO₂ oxidation catalysts, respectively. Mamede, et al., performed similar experiments during NO and CO reactions over Pd/Al₂O₃ [39]. To our knowledge, there are no reports of the characterization of PdRe/Al₂O₃ catalysts using Raman spectroscopy.

2 Experimental

2.1 Catalyst Preparation

The catalysts were supported on γ -Al₂O₃, which was purchased from Strem, and is referred to as Al₂O₃ (A). Analogues of several catalysts were prepared on another γ -Al₂O₃ support (Grace Davison MI-209), referred to as Al₂O₃ (B). The Al₂O₃ surface areas, specific pore volumes and alkali and alkaline earth metal impurity contents are given in Table 2. The precursors, metal loadings and calcination conditions for these catalyst prepared on these supports are listed in Table 3. Briefly, co-impregnation was accomplished by IW impregnation with a single solution of HReO₄ and Pd(NO₃)₂. The first sequential method involved IW impregnation of reduced and passivated Pd/Al₂O₃ [made from tetraamminepalladium nitrate, denoted (TA)] with a solution of HReO₄ and use without subsequent calcination. An analogue of this catalyst was made on γ -Al₂O₃ (B), denoted as Re-Pd⁰ seq. (B) in figures and the text. The second sequential method involves IW impregnation of calcined Re/Al₂O₃ with a solution of Pd(NH₃)₄(NO₃)₂ and a second calcination. These catalysts are referred to as Pd(TA)Re seq. and distinguished by calcination temperature. One analogue was impregnated with Pd(NO₃)₂ instead of the tetraammine, and is denoted as Pd(NO₃)Re seq. Each catalyst was dried at 110°C overnight and stored in a desiccator jar until use. Monometallic catalysts are denoted by the corresponding precursor: Pd (NO₃) for Pd(NO₃)₂, Pd (TA) for Pd(NH₃)₄(NO₃)₂, Re (H) for HReO₄ and Re(N) for NH₄ReO₄. The tetraammine precursor impregnation solution was pH 10 under all circumstances; Pd(NO₃)₂ was impregnated in neutral solution, except in the single solution of Pd(NO₃)₂ and HReO₄ used for PdRe co., which was pH 1.

Table 2. Characterization of γ -Al₂O₃ support by N₂ physisorption and ICP-OES

	γ -Al ₂ O ₃ (A)	γ -Al ₂ O ₃ (B)
BET surface area (m²/g)	217	180
Total specific pore volume (cm³/g)	0.47	0.80
Metal	Content (ppm)	
Na	213	3.32
Mg	24.0	<0.3
K	8.32	<0.3
Ca	132	<0.3

Table 3. Catalyst preparation and metal content as determined by ICP-OES

Catalyst	Metal precursors	Pd loading (wt%)	Re loading (wt%)	Calcination conditions
1% Pd (NO ₃)	Pd(NO ₃) ₂	0.91	---	400°C, 3h
3% Pd (NO ₃)	Pd(NO ₃) ₂	2.66	---	400°C, 3h
Pd (TA)	Pd(NH ₃) ₄ (NO ₃) ₂	2.34	---	400°C, 3h
PdRe co.	Pd(NO ₃) ₂ and HReO ₄	2.43	4.41	400°C, 3h
Re-Pd ⁰ seq.	HReO ₄ and Pd(NH ₃) ₄ (NO ₃) ₂	2.80	4.63	400°C, 3h
Re-Pd ⁰ seq.(B)	HReO ₄ and Pd(NH ₃) ₄ (NO ₃) ₂	2.87	5.36	350°C, 1h
Pd(NO ₃)Re seq.	Pd(NO ₃) ₂ and HReO ₄	2.15	5.73	400°C, 3h
Pd(TA)Re seq.	NH ₄ ReO ₄ and Pd(NH ₃) ₄ (NO ₃) ₂	2.27	4.24	400°C, 3h
Re (H)	HReO ₄	---	5.29	400°C, 3h
Re (N)	NH ₄ ReO ₄	---	4.54	400°C, 3h

2.2 CO and H₂ Chemisorption

Volumetric chemisorption of H₂ and CO were performed using a Micromeritics ASAP 2020 surface area and porosimetry analyzer. Each sample was reduced in situ at 400C for 1 h, evacuated at 400C for 2 h, then cooled to 100°C for analysis by H₂. The H₂ analysis

was repeated at 70°C and 35°C, in order, and the sample was evacuated at 300°C for 1 h between each analysis. Finally, CO analysis was performed at 35°C.

2.3 CO DRIFTS

DRIFT spectra of adsorbed CO were measured on a Bruker Vertex 70 FTIR with a liquid N₂-cooled MCT detector using a Harrick Praying Mantis cell. Prior to measurement, samples were reduced in a high temperature *in situ* DRIFTS cell at 400°C for 1 h in 40 sccm H₂ (Research grade, National Welders), then purged in He at 40 sccm (UHP, National Welders) for 1 h before cooling to 20°C. Pulses of 5% CO/He (certified, National Welders) were administered five at a time at 20°C until no further changes in spectra were observed. Scans of the reduced catalyst (128 scans at 4 cm⁻¹ resolution) at 20°C in He were subtracted from scans following pulses of CO in order to subtract out signal from H₂O.

2.4 Raman Spectroscopy

Raman spectra of the powder samples were recorded on a Horiba Jobin-Yvon LabRAM HR VIS high-resolution confocal Raman microscope using a He-Ne laser (632 nm) excitation source and 100X objective. The laser power was 20 mW, and the confocal hole size was 800 μm. The instrument was calibrated using a Si wafer at 520.7 cm⁻¹. The exposure time was 15 s at a resolution of 0.1 cm⁻¹. The samples were scanned at room temperature in air. No degradation of the samples were observed during collection of spectra, i.e., attenuation of bands over time. Raman bands due to the Al₂O₃ support have been removed by taking the difference between the sample spectrum and appropriate multiples of the Al₂O₃ spectrum.

2.5 XAFS Spectroscopy

XAFS spectra were measured at the Advanced Photon Source at Argonne National Laboratory on beamline MR-CAT-10BM. A mixture of 3.5% H₂/He (certified, Airgas) was used to reduce the catalysts. After a 1 h hold at 400°C, samples were cooled to room temperature, and purged in He for 30 minutes (UHP, Airgas). Calibration of the monochromator, comprising two Si(111) crystals, was performed using Pd foil (0.05 mm thick) and Re metal powder (350 mesh, 99.99% Re Strem). The RePd⁰ seq. catalysts were measured in a cylindrical sample holder with Kapton windows [40]; PdRe co. and Pd (TA)* were measured in an *in situ* XAFS cell with Be windows [41]. Gas mixtures used in the ionization chambers for the Pd K-edge (24350 eV) were: 40% N₂- 60% Ar for I₀ and 100% Ar for I_t; for the Re L_{III}-edge (10535 eV): 95% N₂-5% Ar for I₀ and 30% N₂-70% Ar for I_t.

The EXAFS data was processed using Athena [42], and the Fourier transforms were fit using Artemis [43] and FEFF references described elsewhere (see Chapter 2). The Pd-Re FEFF reference was the same as described in Chapters 1 and 2. The same amplitude reduction factors, S_0^2 , 0.76 for Pd and 0.78 for Re, were used as in previous chapters. The reported fitting parameters for each path are coordination number (N), interatomic distance (R), Debye-Waller factor (σ^2) and inner potential shift (ΔE_0) based on simultaneous k^n ($n=1-3$) fits of the Fourier transform.

2.6 HAADF-STEM- EDX

High-resolution STEM imaging was performed on an aberration-corrected FEI Titan 80-300 electron microscope. The microscope is equipped with a high-angle annular dark field (HAADF) detector and SuperX EDS system comprising four Bruker silicon drift

detectors. Samples were reduced *ex situ* at 400°C, and handled under N₂, except for brief exposure during insertion into the microscope. The powder was supported on carbon-coated copper grids (Ted Pella).

2.7 Furfural hydrogenation testing

Furfural hydrogenation activity was tested in a continuous flow packed-bed reactor system at 150°C and atmospheric pressure. A schematic of this reactor system is available elsewhere (see Chapter 1). The catalyst bed comprised 50-250 mg catalyst powder and 1.25 g quartz chips and was supported by quartz wool in a 0.5" stainless steel tube. Catalyst bed temperature was measured by a Type-K thermocouple (Omega) in contact with the catalyst inside the tube. Furfural was fed by a syringe pump, vaporized in a stream of 100% H₂, and passed over the catalyst bed. The effluent was monitored by on-line gas chromatographs (GC): GC-TCD (SRI 8610C) with a ShinCarbon ST100 (2 m x 1.0 mm ID) column (Restek), which measured CO, CH₄ and CO₂; a GC-FID (Shimadzu 2010) with an EconoCap-1 column (30 m x 0.53 mm ID, Alltech) measured all other products.

3 Results and Discussion

3.1 As-Prepared Catalysts

3.1.1 Pd/Al₂O₃ Catalysts

The main feature in the Raman spectra of Pd/Al₂O₃ catalysts (Figure 1a) at 640 cm⁻¹ corresponds to the B_{1g} lattice vibration of PdO crystallites [35]. This Raman band has been observed between 626-651 cm⁻¹ in other investigations of supported catalysts and thin films [36-39, 44]. Arai, et al., found that the peak moved between 626 cm⁻¹ at 600°C and 647 cm⁻¹

at room temperature in sputtered PdO films [44]. Another band observed in Pd (NO₃) at 445 cm⁻¹ is assigned to an E_g lattice vibration by McBride, et al. [35]; however, the authors note that the E_g band is very weak when using a 632.8 nm (He-Ne laser) excitation source, as in the current work. McBride, et al., also observe the peak at ~290 cm⁻¹ and attribute it to a second-order scattering process [35]. It is apparent that these bands are stronger in 3% Pd (NO₃) than in 3% Pd (TA), indicating that PdO particles formed during calcination are larger in the former. The decreased PdO particle size in Pd (TA) can be explained by the so-called strong electrostatic adsorption effect [45]. The high pH of the Pd (TA) impregnation solution is well above the point of zero charge (PZC) of Al₂O₃, thus there is a net negative charge on the Al₂O₃. Specifically, surface hydroxyls are deprotonated, leaving surface O⁻ atoms which attract the [Pd(NH₃)₄]²⁺ cation. Features attributed to PdO lattice vibrations do not appear in the Raman spectrum of 1% Pd (NO₃) catalyst. Lower loading would diminish Raman scattering, but this may also be attributed to the absence of PdO crystallites. Otto, et al. [36], suggest that PdO crystallites smaller than 1.5 nm (i.e., including fewer than 50 metal atoms) constitute a "dispersed phase" interacting with the Al₂O₃ support, indiscernible to Raman spectroscopy.

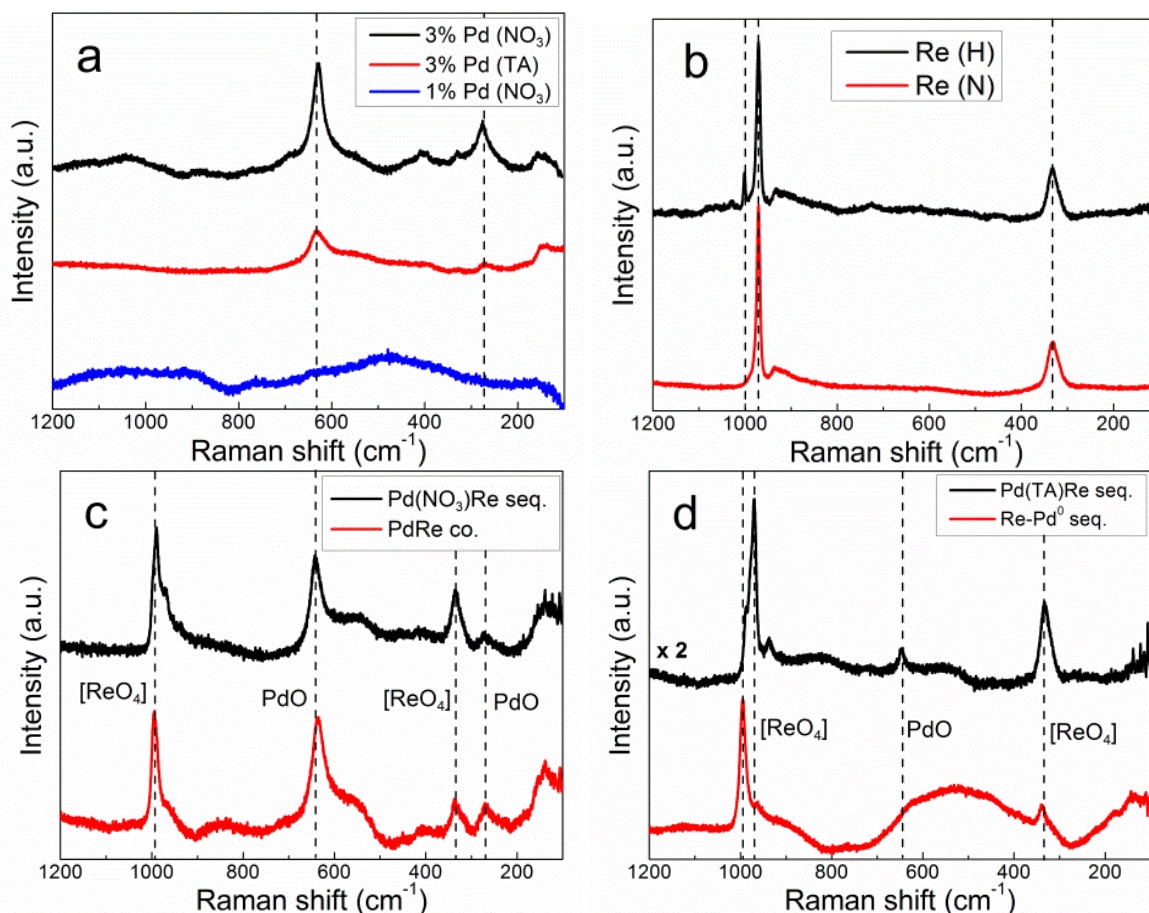


Figure 1. Raman spectra of calcined catalysts after exposure to ambient air: (a) Pd/Al₂O₃, (b) Re/Al₂O₃, c) and d) PdRe/Al₂O₃

There are significant differences in TPR profiles of Pd/AlO₃ catalysts that can be attributed to the Pd precursor (Figure 2a). Reduction of larger PdO particles in 3% Pd (NO₃) occurs very suddenly below room temperature, resulting in a very strong, sharp H₂ uptake peak. This may suggest that the reduction of these particles is autocatalytic, i.e., heat released from metal reduction causes more metal to be reduced. Consequently, Pd nanoparticles are formed at low temperature, and the decomposition of β -PdH_x is evident at ~55°C with H₂ evolution. The H₂ uptake above room temperature may be explained by

smaller PdO particles which interact more strongly with the support. The profile for 3% Pd (TA) (A) is broader and reduction occurs at higher temperature, which is associated with the reduction of smaller PdO crystallites which are more strongly interacting with the Al₂O₃ support. This contradicts the findings of Baylet, et al. [37], who suggest that small PdO particles <5 nm are reduced at room temperature and large PdO particles are not reduced until 100-150°C. There is also a feature a small feature at 290°C due to the reduction of impurity metal carbonates, i.e., Na and Ca, as evidenced by a peaks in m/z 16 and 15 in on-line QMS during reduction and implied by Sumner and Burchett [46]. Most H₂ uptake during TPR of 3% Pd (TA) (B) occurs <50°C. The presence of large Pd particles in this catalyst was demonstrated via CO DRIFTS and STEM (Chapter 2), supporting the assignment of low temperature Pd reduction to large PdO particles. As a result of large Pd⁰ particles reduced at low temperature, H₂ is evolved at 55°C (an inverse peak) due to β-PdH_x decomposition [47]. Some uptake continues to ~100°C which again is attributed to the reduction of smaller PdO particles. The absence of an H₂ uptake feature at 290°C is expected, because Al₂O₃ (B) lacks the Na and Ca impurities of Al₂O₃ (A).

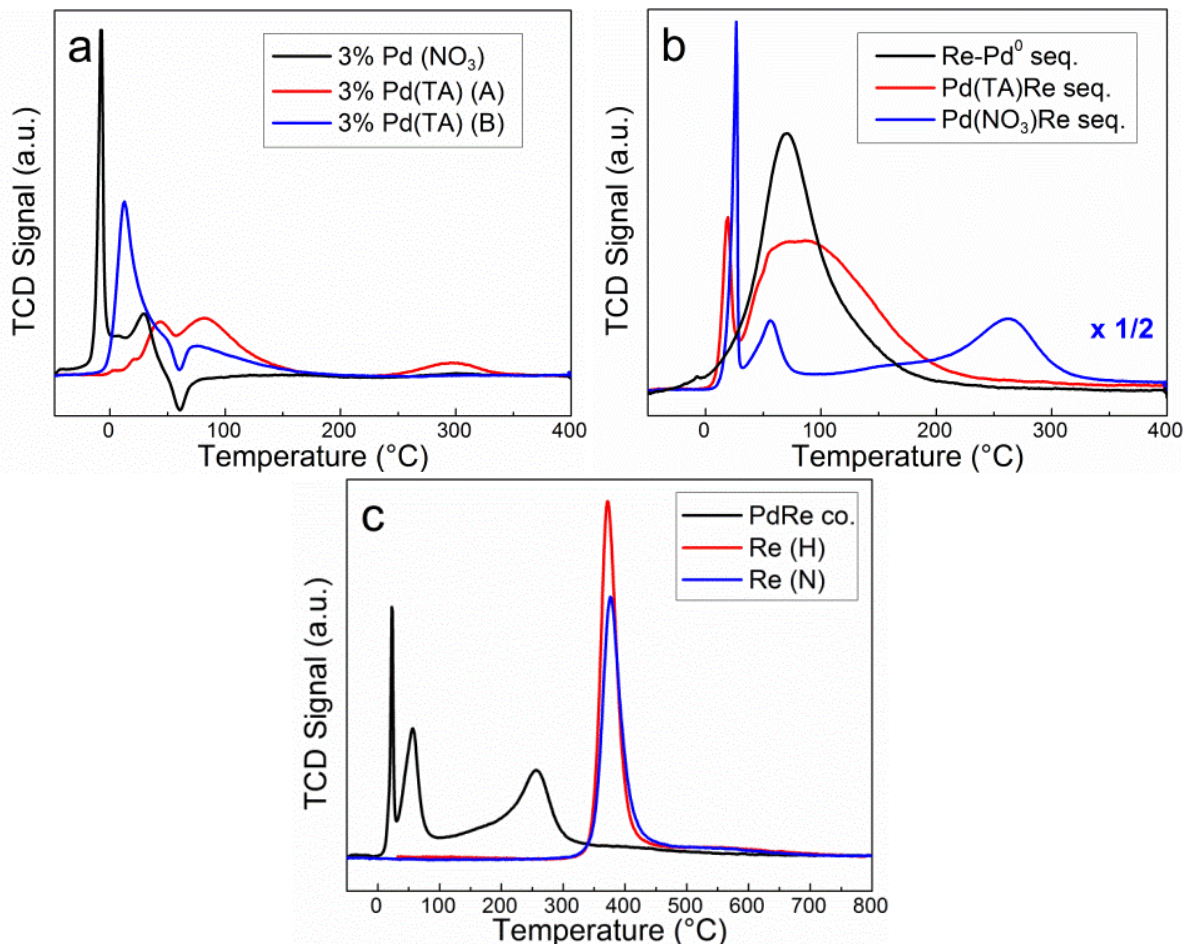


Figure 2. TPR profiles of PdRe/Al₂O₃ catalysts during 10°C/min ramp in 5% H₂/Ar; TCD signal normalized to sample weight

3.1.1 Re/Al₂O₃ Catalysts

Raman spectra of Re/Al₂O₃ catalysts after calcination (Figure 1b) evidence several features corresponding to metal-oxygen stretching and bending modes. The most prominent feature at 970 cm⁻¹ is due to the $\nu_s(\text{Re}=\text{O})$ mode of T_d [ReO₄]⁻ species. The position of this peak corresponds to ReO₄⁻ (perrhenate ion) in solution, which is expected after exposure to ambient moisture after calcination [32]. This peak is shifted to ~1000 cm⁻¹ in the case of [ReO₄]_{ads}, a C_{3v} species with three identical Re=O bonds and presumably a fourth oxygen as

a Re-O-Al bridge to the support [32, 48]. Weaker bands at 920 cm^{-1} and 335 cm^{-1} are assigned to $\nu_{\text{as}}(\text{Re}=\text{O})$ and $\delta(\text{Re-O-Re})$ modes, respectively. There is a small peak at 1000 cm^{-1} in the spectrum of Re (H) that may result from interaction of $[\text{ReO}_4]^-$ with alkali and alkaline earth metal ions. Mitra, et al. [49], showed that presence of Na_2O causes expansion of the Re-O bond length, but this interaction reduced the Raman shift of the Re-O band at 1000 cm^{-1} because their catalysts were scanned after dehydration.

The average Re oxidation state in as-prepared Re (H) and Re (N) was +7. This is the oxidation corresponding to an Re L_{III} edge shift of 4 eV according to the calibration curve shown in Chapter 2. The Re/ Al_2O_3 catalysts were also analyzed by EXAFS spectroscopy in air following calcination (*vide infra*). Fits are compared to experimental data in Figure 3. Both catalysts are fit well with the T_d model of perrhenate ion taken from NH_4ReO_4 XRD data [50]: the Re-O coordination numbers and bond distances were within error of the expected values of 4 and 1.73 \AA , respectively. The low D-W factor, suggestive of a well-ordered structure, was set to improve the error of the fit, and it agrees well with fitting of Re/C following air exposure and consequent re-oxidation to Re^{7+} (see Chapter 1). This structure equates to the $T_d[\text{ReO}_4]^-$ species observed for these catalysts in Raman spectroscopy. The two Re precursors result in equivalent TPR profiles, as shown in Figure 2a. The peak reduction temperature is 390°C in both cases, with the apparent difference in peak height due to a small difference in loading. Some H_2 uptake continues out of 800°C for each catalyst.

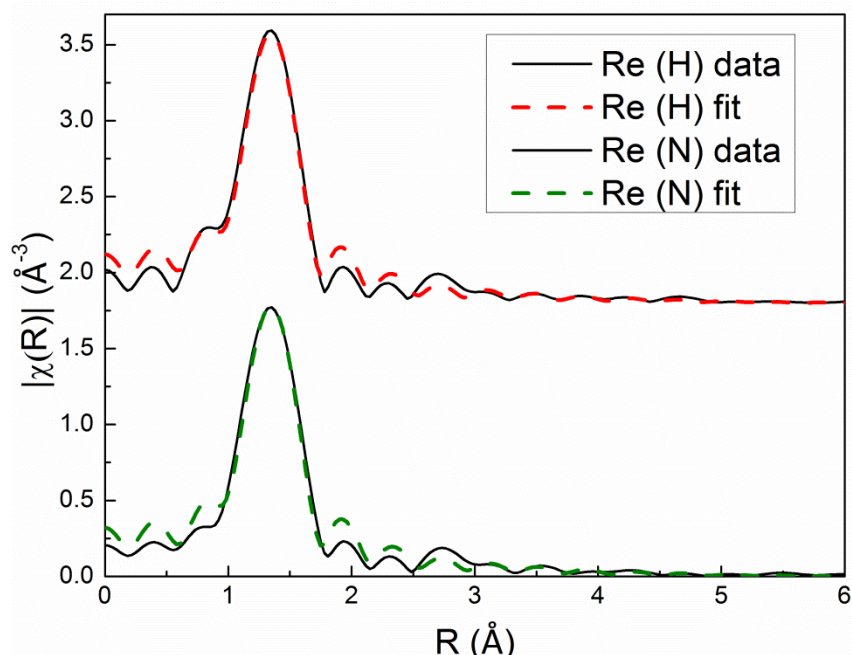


Figure 3. EXAFS FT magnitudes and fits (k^2 -weighting) of "as prepared" Re/Al₂O₃ catalysts

3.1.3 PdRe/Al₂O₃ Co-Impregnation

The intensity of the main PdO band (B_{1g} mode) in the Raman spectrum of PdRe co. suggests that there are large PdO particles present following calcination (Figure 1c). The $\nu_s(\text{Re-O})$ band is found at $\sim 1000 \text{ cm}^{-1}$ in this spectrum, which suggests a lower symmetry C_{3v} geometry of $[\text{ReO}_4]^-$ in PdRe co. This indicates that this sample was less hydrated than the Re/Al₂O₃ catalysts, but it should be emphasized that these samples were all prepared and handled similarly before and during Raman spectroscopy experiments, i.e., all the catalysts had been stored in a desiccator prior to exposure to ambient moisture during data collection. Thus, the presence of PdO modifies prevents hydration of the $[\text{ReO}_4]^-$ in this catalyst.

A strong peak attributed to reduction of large PdO crystallites resulting from calcination of Pd(NO₃)₂ is apparent at $\sim 10^\circ\text{C}$ in the TPR profile (Figure 2c) of PdRe co.;

therefore, features occurring at higher temperatures, must be due primarily to Re reduction. Most H₂ uptake occurs below 300°C, more than 100°C below the peak reduction temperature of Re/Al₂O₃ catalysts. This has been ascribed to hydrogen spillover from Pd and/or Re₂O₇-like species migrating on the Al₂O₃ support in the presence of H₂O to Pd particles to be reduced [29]. The temperature at which Re reduction features are observed has been explained elsewhere as being due to a distribution of Re and Pd across the support. A nonuniform distribution of PdO on the support in the calcined catalyst, i.e., in large, widely-spaced particles, leads to a lag in Re reduction due to diffusion of H₂ or [ReO₄]⁻ across the support.

3.1.4 Re-Pd⁰/Al₂O₃ Sequential

The PdO peak at 650 cm⁻¹ is absent from the Raman spectrum of Re-Pd⁰ seq. (Figure 1d). Instead, there is a large, broad feature at 300-700 cm⁻¹ due to fluorescence from the Al₂O₃ support [36]. Otto, et al. observed that fluorescence in this region is quenched by PdO-support interaction [36]. In this work, fluorescence is suppressed for all samples except Re-Pd⁰ seq., which is the only catalyst reduced and passivated prior to measurement. Suppression of fluorescence can be explained in conjunction with the TPR profile for Re-Pd⁰ seq. The absence of a low-temperature reduction feature attributed to PdO reduction (Figure 2c) indicates that a substantial portion of the Pd remains reduced in Re-Pd⁰ seq., and so it is likely that the PdO is present as a layer on the outside of metallic Pd particles, consistent with the oxidation mechanism proposed by Su, et al. [38]. This PdO layer would, therefore, have insufficient volume to be observed by Raman for the same reason that very small PdO particles would not be. The EXAFS spectrum of Re-Pd⁰ seq. (B) at the Pd K-edge is

displayed in Figure 4a; the Fourier transforms (FTs) magnitude is displayed in Figure 4b. The Pd (TA) parent catalyst, reduced *ex situ* at 400°C, then passivated and handled in air, has a substantial lobe at 1.6 Å in the FT of this catalyst due to Pd-O bonding. The Pd-Pd bond evidences that oxidation of Pd particles was not complete after air exposure.

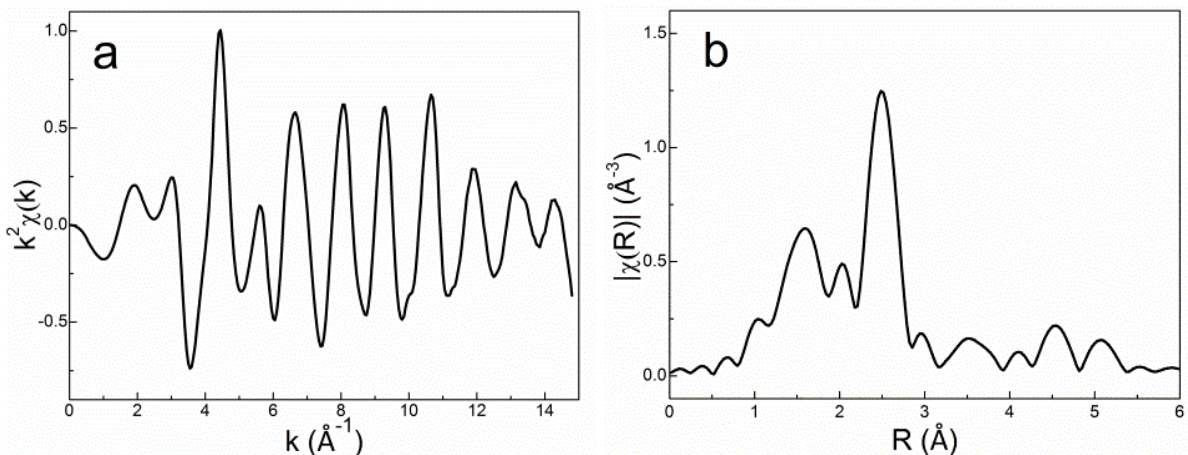


Figure 4. EXAFS (k^2 -weighting) of Pd⁰/Al₂O₃ (B) at room temperature after 400°C reduction and He purge a.) EXAFS signal and b.) Fourier transform magnitude (k-range: 3.0-13.9 Å⁻¹)

The difference in the point group symmetry of the [ReO₄] species in the Raman spectrum of Re-Pd⁰ seq. is also clear (Figure 1d). The [ReO₄] in Re (H) is hydrated by air exposure and consequently assumes a solution T_d point group symmetry, whereas all of the [ReO₄] in Re-Pd⁰ seq. is in a C_{3v} symmetry. The TPR profile exhibits a single symmetric peak with a maximum at ~80°C. This is very similar to the TPR profile reported by Ziemecki, et al. for a similarly prepared Re-Pd⁰ seq. catalyst; however, they point out that extensive dehydration of the catalyst prior to TPR causes reduction to take place at much higher temperatures [29]. Ziemecki implies that the mobility of Re₂O₇ is arrested by

dehydration, as observed in Re-O-Al bonding in Raman spectra [34, 48]. For the current Re-Pd⁰ seq. catalyst, which must be hydrated based on exposure to ambient air and the TPR profile in Figure 2c.

3.1.5 PdRe/Al₂O₃ Sequential Impregnation

The Raman spectrum of Pd(NO₃)Re seq. is displayed in Figure 1c for ease of comparison with PdRe co., the other catalyst prepared from Pd(NO₃)₂. The intensity of the PdO B_{1g} mode is very similar to that of the $\nu_s(\text{Re}=\text{O})$ mode in Pd(NO₃)Re seq., evidencing large PdO particles as with PdRe co. The TPR profile of Pd(NO₃)Re seq. is also similar to PdRe co. (Figure 2b): there is an intense peak at ~20°C due to the reduction of large PdO particles. A peak at 60°C is coincident with the main reduction feature of Re-Pd⁰ seq.; thus, we infer that this is due to the reduction of Re in proximity to Pd⁰ particles produced by PdO reduction at 20°C. As with PdRe co., H₂ uptake continues to increase with temperature until it peaks at ~260°C. We infer that this peak is due to reduction of perrhenate ions that are isolated from Pd on the Al₂O₃ support. The $\nu_s(\text{Re}=\text{O})$ band is split between 1000 cm⁻¹ and 970 cm⁻¹.

The PdO B_{1g} mode is much weaker than the $\nu_s(\text{Re}=\text{O})$ mode for Pd(TA)Re seq. and more similar to that of 3% Pd (TA)/Al₂O₃ indicating that smaller PdO particles (and/or isolated PdO_x complexes) are formed during calcination (Figure 1d). The band at 970 cm⁻¹, assigned to $\nu_s(\text{Re}=\text{O})$ is strong in Pd(TA)Re seq., though there is a shoulder at 1000 cm⁻¹. Thus, [ReO₄]⁻ is more easily solvated by ambient moisture in this catalyst, more similar to Re/Al₂O₃ catalysts. The TPR profile of Pd(TA)Re seq. comprises a small, sharp Pd reduction feature at ~10°C and a broad Re reduction peak at 30-200°C. We infer that more

facile Re reduction in this catalyst is due to more even distribution of Pd, consistent with the small PdO particles evidenced by Raman spectroscopy. The large PdO particles formed in Pd(NO₃)Re seq. demonstrate the importance of the Pd precursor in controlling the Pd distribution, since Pd(NO₃)Re seq. and Pd(TA)Re seq. were prepared in the same manner, differing only in the Pd precursor. These results suggest that the size and distribution of PdO after calcination is affected more strongly by the metal precursor than by the method of preparation. Now, having considered catalyst morphology in the "as-prepared" catalysts and understanding the trends in reduction up to 400C, we consider the catalyst morphology following H₂ treatment.

3.2 Catalysts after In Situ Reduction at 400°C

3.2.1 Pd/Al₂O₃ Catalysts

The significant increase in chemisorbed CO on Pd (TA) as compared to 3% Pd (NO₃) indicates smaller Pd particles, i.e., higher metal dispersion, that can be attributed to the strong electrostatic adsorption effect [45] (Table 4). The CO/metal ratio for 1% Pd (NO₃) is triple that of 3% Pd (NO₃), consistent with ~2 nm and ~4 nm Pd particles, respectively; the CO/metal uptake on Pd (TA) suggests ~1 nm Pd particles on average. The H/Pd ratio measured by H₂ chemisorption at 35°C is equivalent to CO/Pd on Pd (NO₃) catalysts, and decreases, albeit slightly, at 70°C and 100°C, as expected. The H/Pd ratio is lower than CO/Pd on 3% Pd (TA).

Table 4. CO and H₂ chemisorption results: specific uptake ($\mu\text{mol}/\text{g}_{\text{cat}}$ CO or H₂) and molar CO (or H)/metal ratio as determined by ICP-OES

Catalyst	CO chemisorption		H ₂ chemisorption					
	CO uptake	CO/metal	35°C		70°C		100°C	
			H ₂ uptake	H/metal	H ₂ uptake	H/metal	H ₂ uptake	H/metal
1% Pd (NO ₃)	28.5	0.333	12.7	0.297	12.1	0.283	8.8	0.204
3% Pd(NO ₃)	32.4	0.130	16.7	0.133	12.1	0.105	12.4	0.100
Pd (TA)	103	0.469	45.0	0.320	13.1	0.252	34.1	0.242
PdRe co.	59.0	0.127	26.7	0.115	28.3	0.122	32.9	0.142
Re-Pd ⁰ seq.	80.5	0.157	17.9	0.070	15.7	0.061	21.6	0.084
Re-Pd ⁰ seq. (B)	74.1	0.133	16.6	0.060	18.9	0.068	27.4	0.098
Pd(NO ₃)Re seq.	50.5	0.099	---	---	---	---	---	---
Pd(TA)Re seq.	92.6	0.210	20.3	0.092	14.4	0.065	21.1	0.096
Re (H)	21.0	0.084	---	---	---	---	---	---
Re (N)	20.4	0.074	2.3	0.019	4.5	0.037	14.5	0.119

The relative intensities (in K-M units) for CO DRIFT spectra in Figure 5 are indicative of differences in the quantity of CO chemisorption uptake: CO peaks on Pd(TA)-prepared catalysts in Figure 3a are much more intense than those on Pd(NO₃)-prepared catalysts in Figure 5b, in agreement with the higher CO uptake ($\text{quantity}/\text{g}_{\text{cat}}$) on these catalysts. The linear (atop) peak ($\sim 2080\text{ cm}^{-1}$) is much more intense than the bridging peak (broad peak $\sim 1930\text{ cm}^{-1}$) in Figure 5a. Small metal particles have edge and corner sites that preferentially adsorb CO in the atop configuration [51]. This spectrum also includes a low-frequency tail associated with triply bridging CO [52].

There are two bridging CO bands evident for 3% Pd (NO₃). The more prominent bridging CO peak at 1990 cm^{-1} corresponds to low-index surface planes, e.g., (100), (111), which are preferentially exposed on larger particles ($>10\text{ nm}$) [52, 53]. The bridging CO peak on Pd(111) planes at 1930 cm^{-1} is only a shoulder in 3% Pd (NO₃), meaning that some

smaller Pd particles are present, but the average particle size is >10 nm. On the other hand, the bridging CO peak at 1930 cm^{-1} is more prominent for 1% Pd (NO_3), whereas there is only a small shoulder at 1990 cm^{-1} , meaning that the average Pd particle size is <10 nm, though some larger Pd particles are present. The chemisorption CO/metal ratio of 1% Pd (NO_3) is three times greater than 3% Pd (NO_3), which suggests higher dispersion of Pd in the former, in agreement with this interpretation of CO DRIFT spectra.

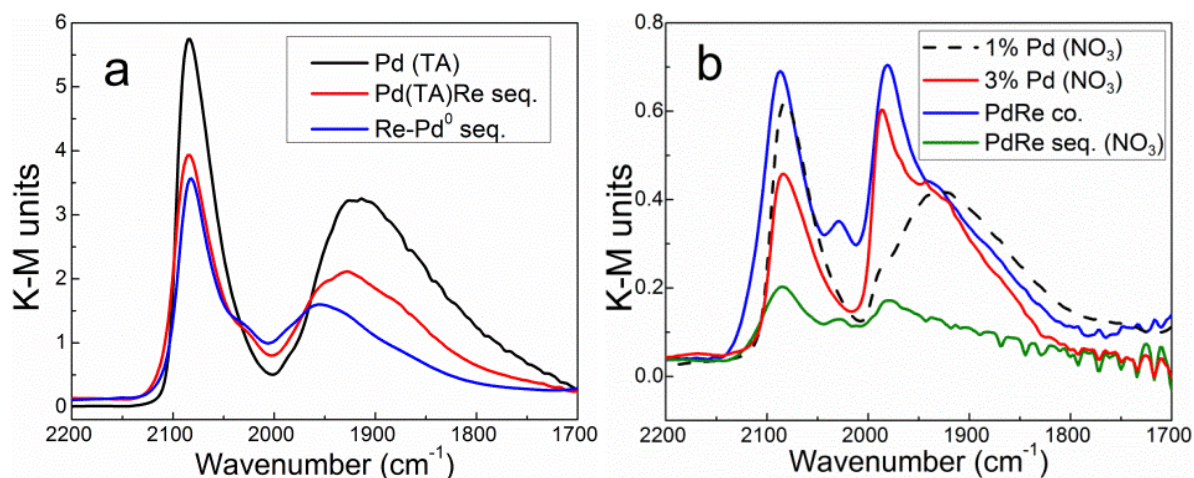


Figure 5. CO DRIFT spectra on PdRe/ Al_2O_3 catalysts after 400°C reduction and 1 h purge in He

3.2.2 Re/ Al_2O_3 Catalysts

The CO/Re ratios for Re(H) and Re(N) from volumetric chemisorption (Table 4) are comparable to one another, suggesting that there is not a significant precursor effect, consistent with the EXAFS and Raman spectra and TPR profiles. This has been observed previously, and is explained by the strong tendency of Re_2O_7 or $[\text{ReO}_4]^-$ species to wet the Al_2O_3 surface during calcination [54]. Dissociative chemisorption of H_2 on Re/ Al_2O_3 has

been reported to be activated [55]. Consequently, at 35°C the H/Re ratio for Re (N) is only a quarter of the CO/Re ratio, and H₂ uptake increases with increasing analysis temperature, although a higher analysis temperature (300°C) is necessary for accurate Re metal surface area measurements [55].

Note that an analogous 5% Re(H) catalyst on Al₂O₃ (B) was characterized by CO DRIFTS, EXAFS spectroscopy and STEM-EDX in Chapter 2. It is useful to summarize those findings here. Atop bonding of CO on Re, manifest as a peak at 2040 cm⁻¹ [56], predominates in the CO DRIFT spectra of Re/Al₂O₃. X-ray absorption near-edge spectroscopy (XANES) evidenced an average Re oxidation state of +2.5 following treatment at 400°C. HAADF-STEM images showed all Re particles were <4 nm in diameter, with well-distributed particles <1 nm.

3.2.3 PdRe/Al₂O₃ Co-Impregnation

The CO/metal ratio for PdRe co. is equivalent to that of 3% Pd (NO₃) (Table 4). The DRIFT spectrum of this catalyst contains two strong peaks at 2080 and 1990 cm⁻¹ assigned to linear and doubly bridging CO on Pd and a medium-intensity peak at ~2040 cm⁻¹ assigned to linear CO on Re [56] (Figure 5b). The linear-to-bridging ratio for CO on Pd is enhanced as compared to 3% Pd (NO₃). We infer that coverage of Pd particles by Re (or alloying) results in fewer adjacent Pd atoms exposed, thereby increasing the linear-to-bridge ratio. The bridging CO on Pd band is observed at a wavenumber corresponding to CO on low-index surface planes, as with 3% Pd (NO₃); however, the peak is red-shifted by ~10 cm⁻¹. The decrease in $\tilde{\nu}(\text{CO})$ indicates increased back-bonding of the CO 2 π^* anti-bonding orbital [57],

and this could be an effect of an alloyed surface, as Pd-Re bonding affects the *d* band of Pd [58].

Hydrogen chemisorption is only slightly suppressed as compared to Pd/Al₂O₃, ($H_{\text{ads}}/CO_{\text{ads}} \sim 1$) (Table 4). Suppression of H₂ chemisorption on PdRe/Al₂O₃ catalysts is expected due to Re coverage of Pd particles since Re does not dissociatively adsorb H₂ at 35°C [55]. The H-surface bond energy is also predicted to be lower on a PdRe alloy surface [58, 59]. This decreased bond energy would lead to more H₂ being desorbed by evacuation during chemisorption experiments and reduce the amount of strongly bound H₂, which is reported in Table 4.

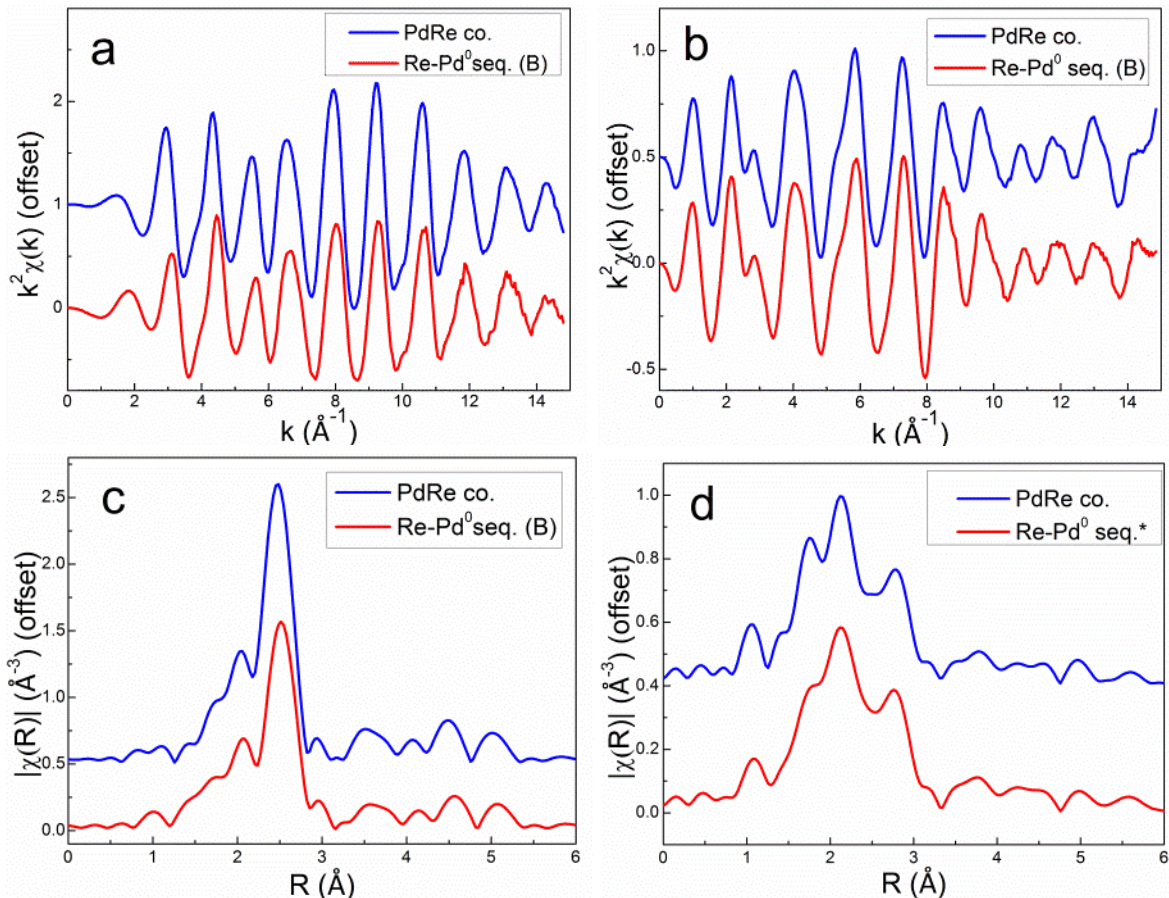


Figure 6. EXAFS (k^2 -weighting) of PdRe/ Al_2O_3 catalysts at room temperature after 400°C reduction and He purge at a.) Pd K-edge and b.) Re L_{III} -edge c.) magnitude Pd K FT (k-range: $2.5\text{-}14.1 \text{ \AA}^{-1}$), d.) magnitude Re L_{III} FT (k-range: $3.5\text{-}14.0 \text{ \AA}^{-1}$)

EXAFS spectra of PdRe co. at the Pd K edge and Re L_{III} edge are shown in Figure 6. The main feature in the Pd K Fourier transform at $\sim 2.6 \text{ \AA}$ is consistent with Pd-Pd (or Re) bond. At the Re L_{III} edge, significant damping of the EXAFS signal is observed above 10 \AA^{-1} (Figure 6b). Destructive interference between Pd and Re backscatters has been suggested as the reason for this attenuation and to the distorted metal-metal peaks in corresponding Fourier transform (Figure 6c) (see Chapter 2). This interference, manifests as a minimum at 2.5 \AA in the FT spectrum. The relative heights of the peaks on either side at 2.1

and 2.8 Å is affected by Re particle size and the ratio of Re-Pd coordination number (CN) to Re-Re CN (Chapter 2).

Table 5. EXAFS fitting parameters for PdRe/Al₂O₃ catalysts

Path*	N	R (Å)	σ^2 (10 ⁻³ Å ²)	ΔE_0 (eV)	R-value
Re (H)					
Re-O	3.9 ± 0.3	1.73 ± 0.01	(1.0)	6.9 ± 2.6	0.009
Re (N)					
Re-O	3.9 ± 0.5	1.73 ± 0.01	(1.0)	7.7 ± 4.3	0.017
PdRe co.					
Pd-Pd	8.8 ± 0.5	2.73 ± 0.01	6.1 ± 0.4	-6.6 ± 0.4	0.006
Pd-Re	1.3 ± 0.3	2.71 ± 0.01	4.2 ± 1.2	-6.6 ± 0.4	
Re-Re	5.7 ± 0.4	2.73 ± 0.01	(7.0)	8.5 ± 1.6	0.021
Re-Pd	1.3 ± 0.3	2.71 ± 0.01	4.2 ± 1.2	8.5 ± 1.6	
Re-O	0.7 ± 0.2	2.02 ± 0.02	(5.0)	8.5 ± 1.6	
Re-Pd⁰ seq. (B)					
Pd-Pd	7.0 ± 0.8	2.73 ± 0.01	6.5 ± 0.8	2.0 ± 0.7	0.015
Pd-Re	0.9 ± 0.3	2.70 ± 0.02	2.6 ± 1.6	2.0 ± 0.7	
Re-Re	5.6 ± 0.5	2.70 ± 0.01	(7.0)	6.8 ± 2.0	0.005
Re-Pd	0.9 ± 0.3	2.70 ± 0.02	2.6 ± 1.6	6.8 ± 2.0	
Re-O	1.0 ± 0.3	2.02 ± 0.02	(5.0)	6.8 ± 2.0	

*first atom is absorber; second, backscatterer

Pd K-edge fit range: k-space 2.7-14.0 Å⁻¹; R-space 1.0-3.0 Å

Re L_{III}-edge fit range: k-space 3.8-14.2 Å⁻¹; R-space 1.3-3.2 Å

Satisfactory fitting of these data was accomplished using Pd-Pd and Pd-Re paths at the Pd K-edge; Re-Re, Re-Pd and Re-O paths were necessary for fitting of Re L_{III}-edge data (Table 5). The Re-O contribution signifies incomplete reduction of Re following 400°C treatment in H₂, which is typical of Re/Al₂O₃ catalysts [23, 60]. After 400°C reduction and He purge, fitting parameters of PdRe co. evidence relatively large Pd particles and Pd-Re bonding. The total first-shell coordination number about Pd, 10.1, suggests particles of 10

nm or greater. A small change in coordination number will lead to an exponential increase in particle size to the bulk number of 12 for an *fcc* metal, which makes it difficult to accurately determine particle size by EXAFS alone as the coordination number approaches 12 [47]. The Pd-Re bond is contracted compared to the Pd-Pd and average Re-Re distances in the metals (2.75 Å), as observed with other PdRe/Al₂O₃ and PdRe/C catalysts (see Chapters 1 and 2). Shorter heterometallic than homometallic bonds have been observed previously via EXAFS [4] and XRD [18, 28] for PdRe alloys. The metallic portion of the first coordination shells about Pd and Re have compositions of 87% and 18.5% Pd, respectively. The highest concentration of Re possible in a solid solution of Pd is 10% Re-90% Pd, according to the binary phase diagram [61], although bulk thermodynamics are not strictly applicable to small particles [62]. This data, in conjunction with TPHD results indicating suppression of PdH_x formation (analogous Al₂O₃ (B) catalyst, Chapter 2), suggests alloy formation in this catalyst and agrees with Meitzner's analysis of PdRe(1:1)/Al₂O₃ prepared by the same method (though with a lower metal loading) [4]. The average Re-O coordination number, 0.7, indicates that reduction is incomplete after heating to 400°C in 5% H₂ although it is a modest contribution assuming that the oxide is ReO₂, as suggested by the average Re-O bond distance, 2.02 Å. This interatomic distance is nearly equal to the average Re-O bond in β-ReO₂, in which the coordination of Re is octahedral, with 4 O atoms at a distance of 1.94 Å, and 2 at a distance of 2.11 Å [63], and suggests the remaining oxidic Re exists as Re⁴⁺. The coexistence of Re⁰ and Re⁴⁺ in treated Re/Al₂O₃ and PtRe/Al₂O₃ has been suggested previously based on electron spin resonance [64] and XPS [65]. Adding a Re-O backscattering path with an interatomic distance of 1.72 Å, corresponding to [ReO₄] [50],

did not significantly improve the fit; hence, the peak at 1.1 Å in the Re L_{III} FTs (Figure 6d) is part of the background, rather than a contribution for a separate oxygen shell.

Low-magnification HAADF-STEM images of this catalyst show large Pd particles, seen as bright white patches around the edge of the Al₂O₃ particle in Figure 7b. This is consistent with large particles evidenced by the high Pd-metal CN in EXAFS, relatively low CO and H₂ chemisorption uptake, and the position of bridging CO on Pd in CO DRIFTS. Figure 8a displays a high resolution HAADF-STEM image of this catalyst showing small particles (<4 nm) distributed across the support. The composite STEM-EDX image (Figure 8c) makes it clear that these are Re particles, whereas the two much larger particles (>20 nm diameter) are Pd. Significant metal-metal contact is suggested by the intense yellow pixels particles associated with the Pd particles that result from the superposition of red and green pixels. Although this image offers no depth resolution, it is clear that some small Re particles are superimposed on the Pd particle, likely making surface contact; the more diffuse Re associated with the Pd-rich particles could be substitutionally alloyed in the Pd *fcc* matrix. It is clear from the EDX images (Figures 8a-c) corresponding to each metal that the large Pd particles have a halo of Re in addition to the larger Re particles. It is probable, based on TPHD results for a similar PdRe co. catalyst on Al₂O₃ (B) (see Chapter 2), that a portion of Re is alloyed with the Pd particle, thereby preventing PdH_x formation. There is also clearly a Re-poor area to the right of the Pd particles, suggesting that Re may have migrated to the Pd particles to be reduced [29]. The uneven distribution of Pd on the PdRe co. catalysts was expected based on TPR profiles of these catalysts. The Re that is in most intimate contact

with Pd is reduced at low temperature, and then spillover H_2 must diffuse to Re, which is further away from large, unevenly distributed Pd particles.

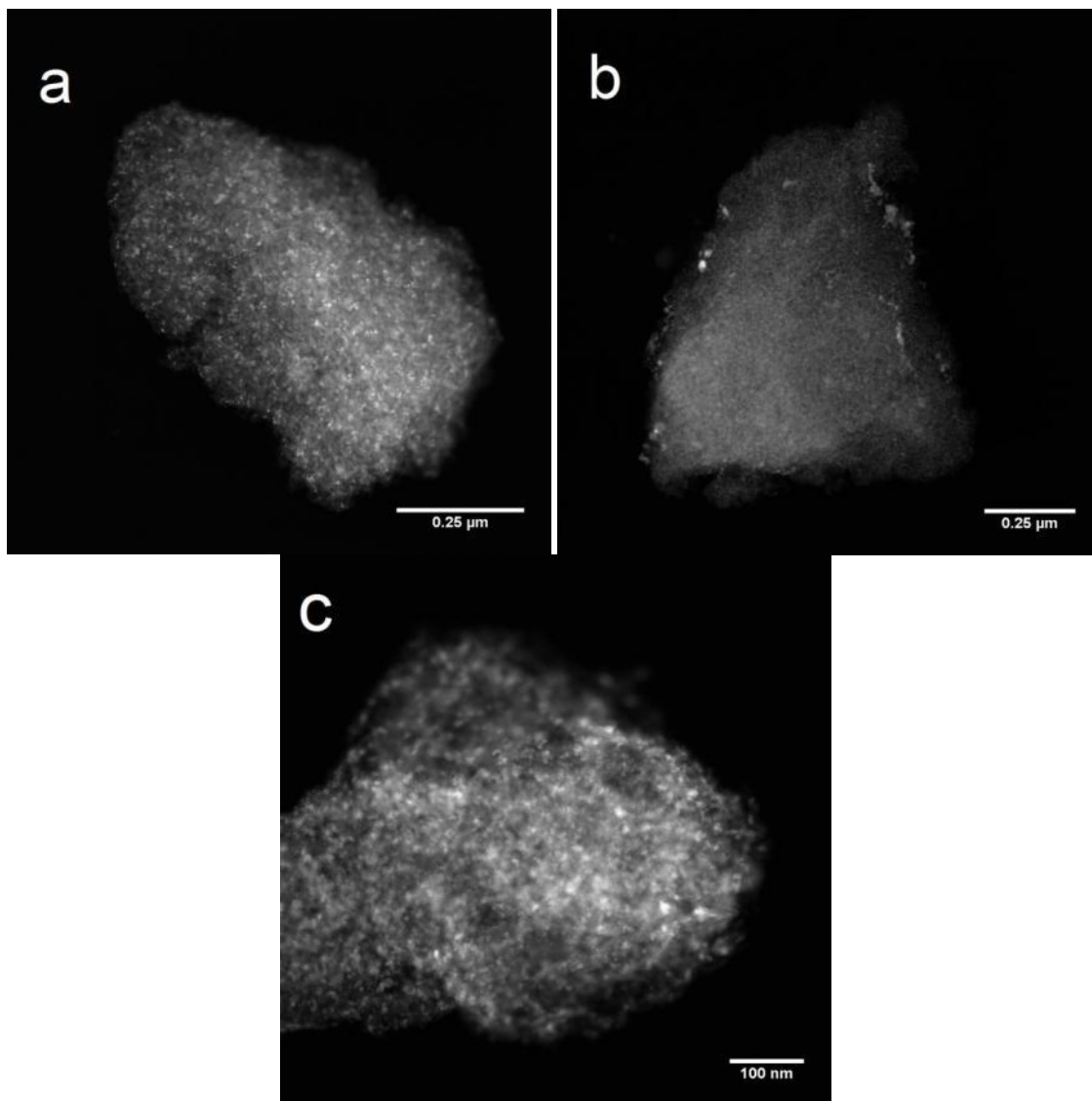


Figure 7. Low-magnification HAADF-STEM images of Pd(TA)Re seq. , b.) PdRe co. and c.) Re-Pd⁰ seq. (B)

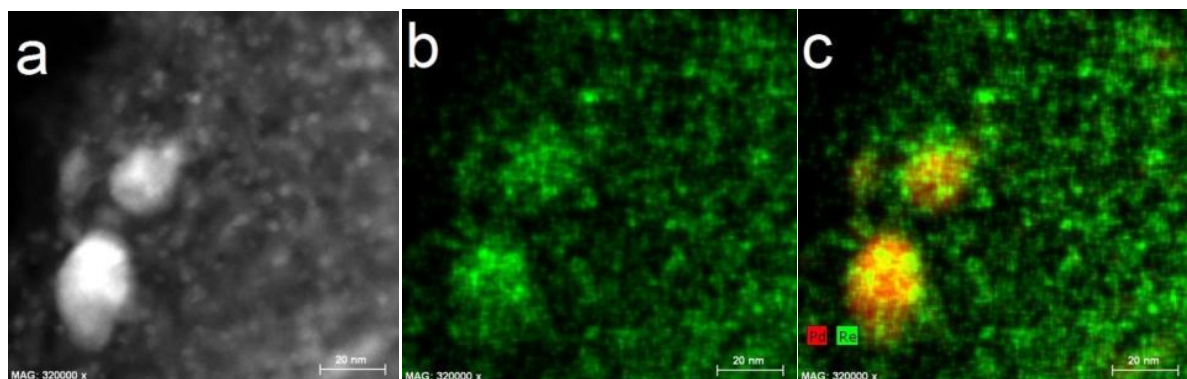


Figure 8. STEM images of PdRe co. a.) HAADF-STEM, b.) Re STEM-EDX and c.) composite STEM-EDX (20 nm scale bar); red – Pd, green – Re, yellow – superposition

3.2.4 Re-Pd⁰ Sequential Catalysts

The two Re-Pd⁰ seq. catalysts that were prepared using Pd(TA) have lower CO uptake and CO/metal ratios than the Pd (TA) catalyst, suggesting lower metal surface areas [19]. We have pointed out previously, however, that during the 400°C evacuation, some Re is re-oxidized by interaction with the Al₂O₃ support. Thus, lower CO/metal ratios for Re-Pd⁰ seq. catalysts than for the Pd (TA) catalyst may not be indicative of large metal particles. In fact, the CO DRIFT spectrum of Re-Pd⁰ seq. (A) suggests a significant enhancement of the linear-to-bridging ratio for CO adsorbed on Pd (Figure 5a). In conjunction with its large magnitude relative to PdRe co. and the lack of a pronounced bridging CO on Pd peak at 1990 cm⁻¹, this suggests relatively small Pd particles. H₂ chemisorption is more strongly suppressed on these catalysts than on PdRe co. suggesting that this preparation method may result in greater Re coverage of Pd and metal-metal interaction (see Chapter 2).

The Pd-metal peak at ~2.6 Å in the FT is somewhat smaller in RePd⁰ seq. (B) than PdRe co., consistent with smaller metal particles (Figure 6d). The total Pd-metal CN of Re-

Pd⁰ seq. (B), prepared from a reduced and passivated Pd (TA) catalyst, is 7.9, evidencing that Pd particles are smaller than in PdRe co. The ratio of Pd:Re coordination numbers at the Pd- and Re edges in Re-Pd⁰ seq. are 89% and 14%, respectively. These compositions are very similar to the first-shell compositions of PdRe co. This composition seems to be an upper limit to all the catalysts tested, including PdRe/Al₂O₃ catalysts in Chapter 2. The total Re-metal CN is nearly equivalent to that of PdRe co.; therefore, the size of Re particles are similar to the Re particles in PdRe co. The heterometallic bond distance is also nearly equivalent in PdRe co. and Re-Pd⁰ seq. The Re-Re bond distance is smaller in RePd⁰ seq., 2.70 Å, as compared to 2.73 Å in PdRe co. and 2.75 Å on average in Re *hcp* metal. The Re-O contribution is 1.0, slightly larger than in PdRe co. The structural information gleaned from EXAFS analysis is helpful, but because it averages over all of the Pd and Re in the catalysts, and a distribution of species is evident from TPR, it must be complemented by other characterization techniques.

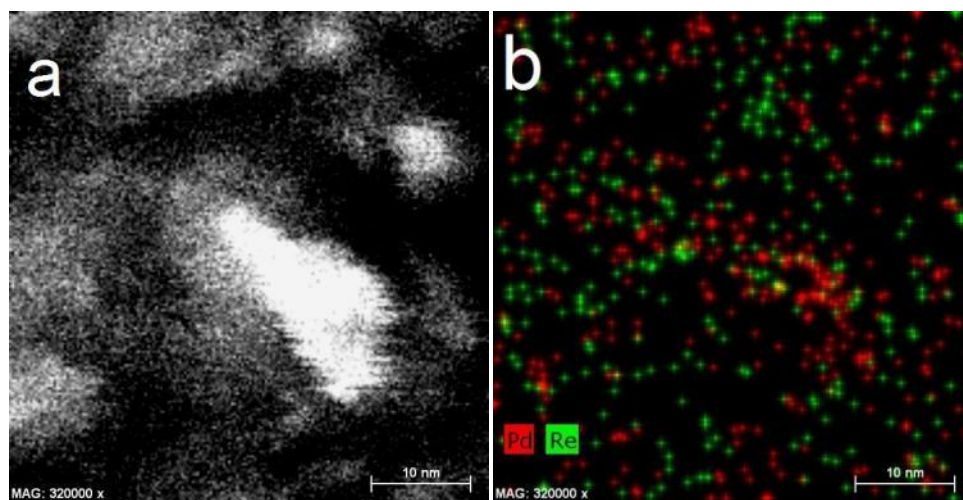


Figure 9. STEM of Re-Pd⁰ seq. (B) a.) HAADF-STEM and b.) STEM-EDX (10 nm scale bar); red – Pd, green – Re, yellow – superposition

It is difficult to distinguish the small metal particles from thick areas of Al_2O_3 in the low-magnification HAADF-STEM image of Re-Pd⁰ seq. (B) (Figure 7c), but all metal particles appear to be <10 nm in diameter. The large, overexposed particle in the middle of the high-magnification HAADF-STEM image (Figure 9a) appears to be several adjacent Pd-rich particles with some diffuse Re nearby; however, the EDX counts were very low and difficult to accurately interpret. At the least, it is clear that both metals are in close contact on small particles, as suggested by EXAFS and suppressed H₂ chemisorption. The intimate contact of Pd and Re in small particles, in particular, even distribution of small Pd in this catalyst, would lead to improved diffusion of spillover H₂ to Re, facilitating its reduction as seen in TPR.

3.2.5 PdRe/Al₂O₃ Sequential Impregnation

CO uptake on Pd(TA)Re seq. is twice as large as on Pd(NO₃)Re seq.; the CO uptake on the latter is more similar to that of PdRe co., which suggests similar metal particle sizes. Suppression of H₂ chemisorption is very similar over these two catalysts as evident from H₂ uptake at 35°C. The CO DRIFT spectrum of Pd(TA)Re seq. is similar to that of the monometallic Pd (TA) catalyst (Figure 5a), with a broad bridging CO peak at ~1930 cm⁻¹ and without bridging CO on low-index Pd planes (1990 cm⁻¹). As with Re-Pd⁰ seq., made from a Pd (TA) parent catalyst, the linear CO on Pd peak is much larger than bridging CO on Pd. Again, we infer that this is an effect of a PdRe alloy surface, with fewer adjacent Pd surface atoms available as bridging CO sites. The bridging CO on Pd peak at 1990 cm⁻¹ is prominent in the CO DRIFT spectrum of Pd(NO₃)Re seq. (Figure 5b), indicating that low-index surface planes are preferentially exposed on Pd particles. As with PdRe co., this peak is red-shifted

compared to 3% Pd (NO₃), which implies an electronic effect of an alloyed Pd-Re surface, as discussed above. The bimetallic surface also accounts for the higher magnitude of linear CO on Pd (2080 cm⁻¹) relative to the bridging CO on Pd peak for Pd(NO₃)Re seq. A small linear on Re peak is also present at ~2040 cm⁻¹.

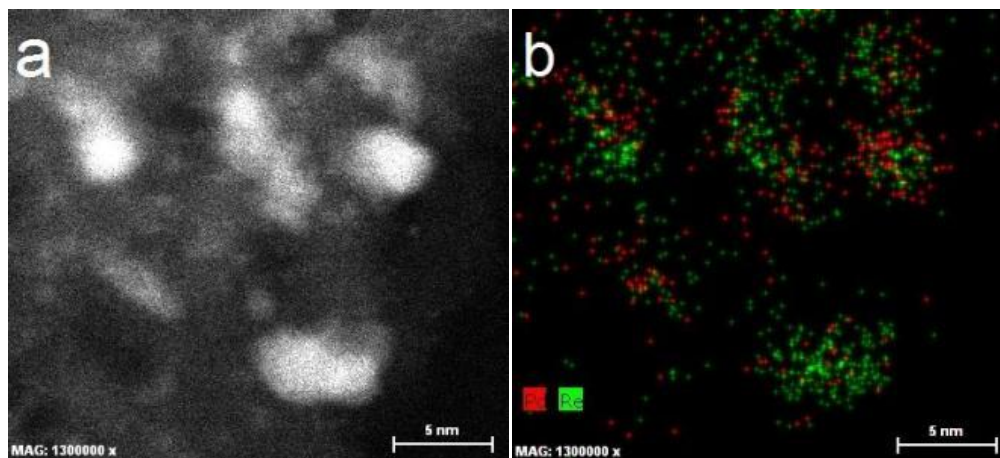


Figure 10. STEM images of Pd(TA)Re seq. a.) HAADF-STEM and b.) STEM-EDX (5 nm scale bar); red – Pd, green – Re, yellow – superposition

Metal particles in Pd(TA)Re seq. are all <10 nm in diameter, as seen in Figure 7a. High-resolution STEM-EDX in Figure 10b shows small Re-rich particles 2-5 nm in diameter in intimate contact with Pd. Small particles of Pd with high index surface planes are indicated by the position of bridging CO in CO DRIFTS. Also, the EXAFS spectrum of an analogous catalyst on Al₂O₃ (B) (Chapter 2) evidences substantial destructive interference at high-*k*, which is demonstrated to result from Pd-Re bonding, consistent with the particle morphology in STEM-EDX images in Figure 10. Small PdO particles evident from Raman spectroscopy of calcined Pd(TA)Re seq. do not sinter significantly during reduction.

Furthermore, their even distribution across the Al_2O_3 support, facilitates reduction of most of the Re in the sample. The peak reduction temperature is $\sim 300^\circ\text{C}$ lower than $\text{Re}/\text{Al}_2\text{O}_3$. In contrast, large PdO particles are present in $\text{Pd}(\text{NO}_3)\text{Re}$ seq. before reduction and mobile species (spillover hydrogen or $[\text{ReO}_4]$) must diffuse across the support, resulting in an expanded reduction profile.

3.3 Furfural hydrogenation catalysis

As explained in Chapter 2, three pathways were observed for furfural reaction over $\text{PdRe}/\text{Al}_2\text{O}_3$ catalysts. Furfural decarbonylation leads to furan and CO. Furan production was suppressed over all bimetallic catalysts as compared to $\text{Pd}/\text{Al}_2\text{O}_3$, as evident from the magnitude of the black shaded sections in Figure 11. Instead, the bimetallic catalysts favored hydrogenation of furfural to furfuryl alcohol (FAL), the desired pathway. A third pathway is hydrodeoxygenation furfural to 2-methyl furan (2-MF), which the bimetallic catalysts were also much more selective to than $\text{Pd}/\text{Al}_2\text{O}_3$ was. Selectivity was generally low to ring-saturation products, tetrahydrofuran (THF), tetrahydrofurfuryl alcohol (THFAL) and 2-methyl THF (2-MTHF). No ring-opening products, i.e., butanols or pentanols, were observed under these conditions. Each bar in Figure 11 represents the furfural consumption rate, and it is clear that the three catalysts made by sequential methods are far more active than $\text{Pd}/\text{Al}_2\text{O}_3$ or the PdRe co. $\text{Pd}(\text{TA})\text{Re}$ seq. (A) is more active than its Al_2O_3 (B) analogue (Chapter 2). We suggest that this could be a promoter effect of the Group I or IIA metal impurities, particularly Na and Ca, as noted in a patent by Mabry, et al. [16]. The Re-Pd^0 seq. catalyst has marginally lower activity than $\text{Pd}(\text{TA})\text{Re}$ seq.

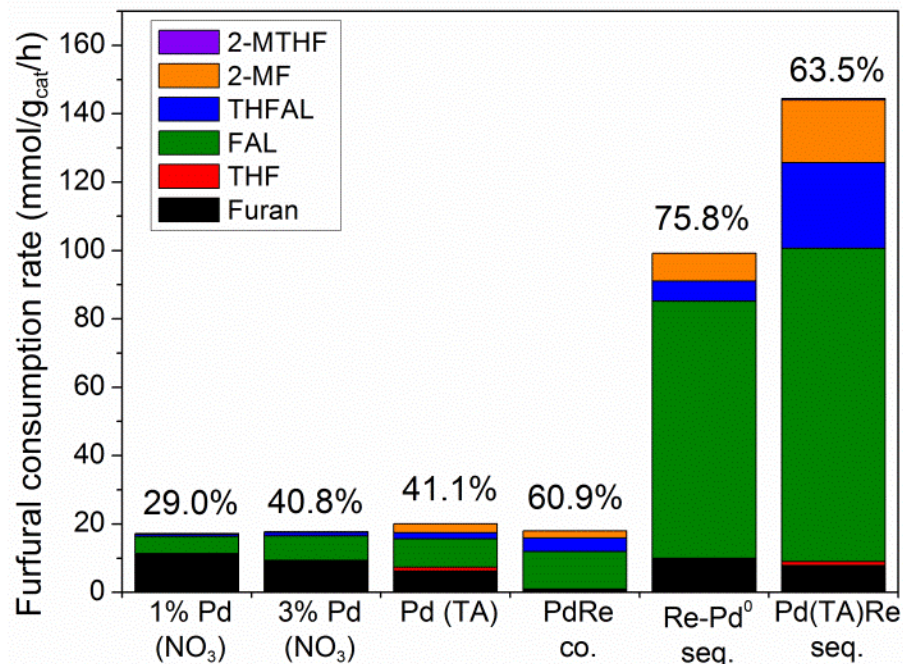


Figure 11. Product formation rates at 150°C, 1 atm; product rates sum to furfural consumption rate. FAL selectivity indicated.

Turnover frequencies (TOFs) for these catalysts based on CO and H₂ chemisorption at 35°C are compared in Table 6. The CO and H TOFs match well over Pd/Al₂O₃ catalysts due to the suitability of both as probe molecules for surface Pd atoms; however, TOFs on a per H atom basis are much larger than a CO basis over PdRe/Al₂O₃ due to suppressed H₂ chemisorption discussed previously. Overall, furfural and FAL TOFs are much higher over Pd(TA)Re seq. and Re-Pd⁰ seq. catalysts than PdRe co. or Pd/Al₂O₃. In conjunction with improved FAL selectivity, this TOF difference suggests that the nature of Pd-Re interaction on these catalysts leads to active sites that have higher intrinsic activity for FAL production. The trend of increasing FAL selectivity with decreasing ratios of chemisorbed H/CO, discussed at length in Chapter 2, suggests that Re, which does not readily dissociatively

adsorb H₂ at 35°C, covers portions of the surface of Pd-rich particles. This Pd-Re contact on the surface is likewise here suggested to be responsible for the superior selectivity of all bimetallic catalysts as compared to Pd/Al₂O₃. It is important to note, however, that there is a less-than-two-fold difference in chemisorbed CO between PdRe co. and the sequential catalysts while there is a four- to seven-fold difference in furfural consumption rate. The ratio of H/CO is ~1 for PdRe co., but <0.5 for the Pd(TA)Re seq. and Re-Pd⁰ seq. catalysts.

Table 6. Furfural TOFs (min⁻¹) at 150°C, 1 atm (volumetric chemisorption uptake basis)

Basis	furfural		FAL		Furan		2-MF		THFAL	
	CO	H	CO	H	CO	H	CO	H	CO	H
Grace support										
1% Pd (NO ₃)	10.1	11.3	2.9	3.3	6.5	7.3	1.5	1.7	0.4	0.4
3% Pd (NO ₃)	9.1	8.9	3.7	3.6	4.7	4.5	1.0	1.0	0.5	0.5
Pd (TA)	3.2	3.7	1.3	1.5	1.0	1.2	1.0	1.1	0.3	0.4
PdRe co.	5.1	5.6	3.1	3.4	0.3	0.3	5.2	5.7	1.1	1.3
Re-Pd ⁰ seq.	20.5	46.2	15.6	35.0	2.1	4.6	1.7	3.8	1.2	2.7
Pd(TA)Re seq.	26.0	59.2	16.5	37.6	1.4	3.2	3.3	7.5	4.5	10.3

4 Conclusions

Due to the low solubility of Pd and Re and to Re-Al₂O₃ interaction induced by calcination, there is considerable difficulty in controlling morphology in PdRe/Al₂O₃ catalysts and understanding the role of Pd-Re interaction in selective hydrogenation. We have demonstrated that by consideration of the Pd precursor and the method by which the two metals are introduced to the support, some control may be exercised over the structure of the catalyst. At a sufficiently low loading (1%), small Pd particles may be generated using the Pd(NO₃)₂ precursor. Very large Pd particles (>20 nm) are evident in the results of CO

DRIFTS and STEM-EDX of the 3% Pd catalysts prepared from Pd (NO₃), whether monometallic, PdRe co. or Pd(NO₃)Re seq. The Pd(TA) precursor, on the other hand, yields smaller Pd particles (≤ 5 nm) in spite of a 3% Pd loading. Large PdO particles form during calcination of the ex-Pd (NO₃) catalysts, but PdO particles remain small in the Pd(TA)-prepared catalysts, as observed by Raman spectroscopy. The large PdO particles in Pd (NO₃) catalysts are reduced suddenly, as evidenced by large, sharp H₂ uptake at 0-25°C in TPR. This peak is shifted to somewhat higher temperatures in the bimetallic catalysts which evidences simultaneous reduction of a portion of the Re. Furthermore, interaction between [ReO₄] and PdO is suggested by the shift of $\nu_s(\text{Re}=\text{O})$ to 1000 cm⁻¹. Incorporation of Re into Pd particles is thought to result in suppression of PdH_x (see Chapter 2). As the temperature continues to increase during reduction, the migration of [ReO₄]⁻ to Pd particles leads to Re coverage of the Pd-rich particle, and then some Re remains isolated on the support, reduced only >250°C.

Catalyst preparation from Pd(TA) leads to better Pd dispersion due to the strong electrostatic adsorption effect. The presence of an equimolar amount of [ReO₄] on the Al₂O₃ support (in the case of Pd(TA)Re seq.) does not obstruct this interaction, as evidenced by small Pd particles in these catalysts as compared to Pd(NO₃)Re seq. The coordination of [ReO₄]⁻ in Pd(NO₃)Re seq. is affected by the presence of large PdO particles after calcination. The smaller PdO particles formed after sequential impregnation or small partially oxidized Pd particles in Re-Pd⁰ seq. give rise to very similar Re reduction profiles. In both cases, the maximum reduction temperature is ~70°C. Rather than Re being integrated into these smaller Pd particles, small Re particles collect on the surface of Pd-rich

particles. It is this interaction that gives these catalysts active sites which are especially active in furfural conversion and selective for FAL. Both sequential methods result in effectively the same catalyst structure.

5 Acknowledgements

This work was funded by Eastman Chemical Company for funding through the Center of Excellence. ICP-OES analysis was performed by Eastman Chemical Company. This research used resources of the Advanced Photon Source, a U.S. Department of Energy (DOE) Office of Science User Facility operated for the DOE Office of Science by Argonne National Laboratory under Contract No. DE-AC02-06CH11357. We gratefully acknowledge the loan of EXAFS equipment from Dr. Jeffrey Miller, and the assistance of Dr. Joshua Wright and Dr. John Katsoudas in operating beamline MR-CAT-10BM. The authors acknowledge the use of the Analytical Instrumentation Facility at NCSU, which is supported by the State of North Carolina and the National Science Foundation, and, in particular, Dr. Xiahan Sang for assistance with STEM-EDX.

References

- [1] C. Betizeau, G. Leclercq, R. Maurel, C. Bolivar, H. Charcosset, R. Frety, L. Tournayan, *J. Catal.*, **45** (1976) 179-188.
- [2] L.W. Jossens, E.E. Petersen, *J. Catal.*, **76** (1982) 265-273.
- [3] A.S. Fung, M.R. McDevitt, P.A. Tooley, M.J. Kelley, D.C. Koningsberger, B.C. Gates, *J. Catal.*, **140** (1993) 190-208.
- [4] G. Meitzner, G.H. Via, F.W. Lytle, J.H. Sinfelt, *J. Chem. Phys.*, **87** (1987) 6354-6363.
- [5] K.Y. Chen, S. Koso, T. Kubota, Y. Nakagawa, K. Tomishige, *Chemcatchem*, **2** (2010) 547-555.
- [6] S. Koso, Y. Nakagawa, K. Tomishige, *J. Catal.*, **280** (2011) 221-229.
- [7] M. Chia, Y.J. Pagan-Torres, D. Hibbitts, Q.H. Tan, H.N. Pham, A.K. Datye, M. Neurock, R.J. Davis, J.A. Dumesic, *J. Am. Chem. Soc.*, **133** (2011) 12675-12689.
- [8] S. Koso, I. Furikado, A. Shimao, T. Miyazawa, K. Kunimori, K. Tomishige, *Chem. Comm.*, (2009) 2035-2037.
- [9] L. Ma, D.H. He, Z.P. Li, *Catal. Comm.*, **9** (2008) 2489-2495.
- [10] L. Ma, D.H. He, *Top. Catal.*, **52** (2009) 834-844.
- [11] Y. Takeda, Y. Nakagawa, K. Tomishige, *Catal. Sci. Tech.*, **2** (2012) 2221-2223.
- [12] A. Shimao, S. Koso, N. Ueda, Y. Shinmi, I. Furikado, K. Tomishige, *Chem. Lett.*, **38** (2009) 540-541.
- [13] Y. Sato, K. Terada, S. Hasegawa, T. Miyao, S. Naito, *App. Catal. A*, **296** (2005) 80-89.
- [14] Y. Sato, K. Terada, Y. Soma, T. Miyao, S. Naito, *Catal. Comm.*, **7** (2006) 91-95.
- [15] B.K. Ly, D.P. Minh, C. Pinel, M. Besson, B. Tapin, F. Epron, C. Especel, *Top. Catal.*, **55** (2012) 466-473.
- [16] M.A. Mabry, W.W. Prichard, S.B. Ziemecki, in, E. I. du Pont de Nemours and Company, United States Patent 4550185, 1985.

- [17] M. Kitson, P.S. Williams, in: U.S.P. Office (Ed.), The British Petroleum Company, United States Patent 5149680, 1992.
- [18] A. Malinowski, W. Juszczak, M. Bonarowska, J. Pielaszek, Z. Karpinski, *J. Catal.*, **177** (1998) 153-163.
- [19] M. Bonarowska, A. Malinowski, Z. Karpinski, *App. Catal. A*, **188** (1999) 145-154.
- [20] K.D. Hurley, J.R. Shapley, *Env. Sci. Tech.*, **41** (2007) 2044-2049.
- [21] K.D. Hurley, Y.X. Zhang, J.R. Shapley, *J. Am. Chem. Soc.*, **131** (2009) 14172.
- [22] W. Juszczak, Z. Karpinski, *App. Catal. A*, **206** (2001) 67-78.
- [23] S. Koso, H. Watanabe, K. Okumura, Y. Nakagawa, K. Tomishige, *J. Phys. Chem. C*, **116** (2012) 3079-3090.
- [24] E.L. Kunkes, D.A. Simonetti, J.A. Dumesic, W.D. Pyrz, L.E. Murillo, J.G.G. Chen, D.J. Buttrey, *J. Catal.*, **260** (2008) 164-177.
- [25] D.A. Simonetti, E.L. Kunkes, J.A. Dumesic, *J. Catal.*, **247** (2007) 298-306.
- [26] O.M. Daniel, A. DeLaRiva, E.L. Kunkes, A.K. Datye, J.A. Dumesic, R.J. Davis, *Chemcatchem*, **2** (2010) 1107-1114.
- [27] M. Chia, B.J. O'Neill, R. Alamillo, P.J. Dietrich, F.H. Ribeiro, J.T. Miller, J.A. Dumesic, *J. Catal.*, **308** (2013) 226-236.
- [28] S.B. Ziemecki, J.B. Michel, G.A. Jones, *React. Sol.*, **2** (1986) 187-202.
- [29] S.B. Ziemecki, G.A. Jones, J.B. Michel, *J. Catal.*, **99** (1986) 207-217.
- [30] M.P. Latusek, B.P. Spigarelli, R.M. Heimerl, J.H. Holles, *J. Catal.*, **263** (2009) 306-314.
- [31] M.D. Skoglund, J.H. Holles, *Catal. Lett.*, **143** (2013) 966-974.
- [32] F.D. Hardcastle, I.E. Wachs, J.A. Horsley, G.H. Via, *J. Mol. Catal.*, **46** (1988) 15-36.
- [33] M.A. Vuurman, I.E. Wachs, *J. Phys. Chem.*, **96** (1992) 5008-5016.
- [34] D.S. Kim, I.E. Wachs, *J. Catal.*, **141** (1993) 419-429.
- [35] J.R. McBride, K.C. Hass, W.H. Weber, *Phys. Rev. B*, **44** (1991) 5016-5028.

- [36] K. Otto, C.P. Hubbard, W.H. Weber, G.W. Graham, *App. Catal. B*, **1** (1992) 317-327.
- [37] A. Baylet, P. Marecot, D. Duprez, P. Castellazzi, G. Groppi, P. Forzatti, *Phys. Chem. Chem. Phys.*, **13** (2011) 4607-4613.
- [38] S.C. Su, J.N. Carstens, A.T. Bell, *J. Catal.*, **176** (1998) 125-135.
- [39] A.S. Mamede, G. Leclercq, E. Payen, P. Granger, J. Grimblot, *J. Mol. Struct.*, **651** (2003) 353-364.
- [40] E. Bus, J.T. Miller, A.J. Kropf, R. Prins, J.A. van Bokhoven, *Phys. Chem. Chem. Phys.*, **8** (2006) 3248-3258.
- [41] F.W.H. Kampers, T.M.J. Maas, J. Vangrondelle, P. Brinkgreve, D.C. Koningsberger, *Rev. Sci. Instr.*, **60** (1989) 2635-2638.
- [42] M. Newville, *J. Synch. Rad.*, **8** (2001) 322-324.
- [43] B. Ravel, M. Newville, *J. Synch. Rad.*, **12** (2005) 537-541.
- [44] T. Arai, T. Shima, T. Nakano, J. Tominaga, *Thin Sol. Films*, **515** (2007) 4774-4777.
- [45] L. Jiao, J.R. Regalbuto, *J. Catal.*, **260** (2008) 329-341.
- [46] C. Sumner, W. Burchett, *Top. Catal.*, **55** (2012) 480-485.
- [47] J.A. McCaulley, *J. Phys. Chem.*, **97** (1993) 10372-10379.
- [48] J. Okal, L. Kepinski, L. Krajczyk, W. Tylus, *J. Catal.*, **219** (2003) 362-371.
- [49] B. Mitra, X.T. Gao, I.E. Wachs, A.M. Hirt, G. Deo, *Phys. Chem. Chem. Phys.*, **3** (2001) 1144-1152.
- [50] G.J. Kruger, E.C. Reynhardt, *Acta Crystall.*, **34** (1978) 259-261.
- [51] J.B. Giorgi, T. Schroeder, M. Baumer, H.J. Freund, *Surf. Sci.*, **498** (2002) L71-L77.
- [52] G. Agostini, R. Pellegrini, G. Leofanti, L. Bertinetti, S. Bertarione, E. Groppo, A. Zecchina, C. Lamberti, *J. Phys. Chem. C*, **113** (2009) 10485-10492.
- [53] T. Lear, R. Marshall, J.A. Lopez-Sanchez, S.D. Jackson, T.M. Klapotke, M. Baumer, G. Rupprechter, H.J. Freund, D. Lennon, *J. Chem. Phys.*, **123** (2005) 13.

- [54] J.A. Moulijn, J.C. Mol, *J. Mol. Catal.*, **46** (1988) 1-14.
- [55] G.W. Chadzynski, H. Kubicka, *Thermochim.Acta*, **158** (1990) 353-367.
- [56] W. Daniell, T. Weingand, H. Knozinger, *J. Mol. Catal.*, **204** (2003) 519-526.
- [57] E. Groppo, S. Bertarione, F. Rotunno, G. Agostini, D. Scarano, R. Pellegrini, G. Leofanti, A. Zecchina, C. Lamberti, *J. Phys. Chem. C*, **111** (2007) 7021-7028.
- [58] V. Pallassana, M. Neurock, L.B. Hansen, J.K. Norskov, *J. Chem. Phys.*, **112** (2000) 5435-5439.
- [59] V. Pallassana, M. Neurock, L.B. Hansen, B. Hammer, J.K. Norskov, *Phys. Rev. B*, **60** (1999) 6146-6154.
- [60] S.R. Bare, S.D. Kelly, F.D. Vila, E. Boldingh, E. Karapetrova, J. Kas, G.E. Mickelson, F.S. Modica, N. Yang, J.J. Rehr, *J. Phys. Chem. C*, **115** (2011) 5740-5755.
- [61] B. Predel, O.E. Madelung, in: *Landolt-Börnstein - Group IV Physical Chemistry*, SpringerMaterials.
- [62] J.H. Sinfelt, *Bimetallic Catalysts: Discoveries, Concepts, and Applications*, John Wiley and Sons, 1983.
- [63] A. Magneli, *Acta Chem. Scand.*, **11** (1957) 28-33.
- [64] M.S. Nacheff, L.S. Kraus, M. Ichikawa, B.M. Hoffman, J.B. Butt, W.M.H. Sachtler, *J. Catal.*, **106** (1987) 263-272.
- [65] J. Okal, W. Tylus, L. Kepinski, *J. Catal.*, **225** (2004) 498-509.

CHAPTER 4: PALLADIUM-RHENIUM SELECTIVE HYDROGENATION CATALYSTS PREPARED FROM A PdRe₂ DOUBLE COMPLEX SALT

Abstract

PdRe/Al₂O₃ prepared from a double complex salt (DCS), Pd(NH₃)₄(ReO₄)₂, leads to remarkably high turnover frequencies (TOF) of furfuryl alcohol (FAL) in selective hydrogenation of furfural at 150°C and ambient pressure. Direct reduction of the DCS-prepared catalyst leads to a uniform catalyst morphology comprising small alloyed nanoparticles (<5 nm), as evidenced by complete suppression of β-PdH_x formation, extended x-ray absorption fine structure (EXAFS) spectroscopy and high-resolution scanning-transmission electron microscopy (STEM) with energy-dispersive x-ray (EDX) imaging. Calcination of the DCS-derived catalyst causes large Pd particles to form after reduction, as evidenced by STEM-EDX and by increased bridging CO adsorption on Pd(100) surface planes in CO diffuse reflectance infrared Fourier transform spectroscopy (DRIFTS). Preparation of a catalyst with analogous metal loading by sequential impregnation (PdRe seq.) results in a closely similar catalyst morphology as the calcined DCS-prepared catalyst, namely, large Pd particles with decreased alloying of Re. Suppression of H₂ chemisorption on all three catalysts is observed and correlates with high FAL selectivity; however, lower Pd surface area in the calcined DCS-derived catalyst and PdRe seq. results in decreased FAL production rate.

1 Introduction

The use of Re as a promoter in bimetallic catalysts, in particular for selective hydrogenation and hydrogenolysis, has increased sharply in the past decade. Formerly, the best-known use of Re was as a promoter which increased catalyst lifetime was in Pt/Al₂O₃ naphtha reforming catalysts by preventing coke formation [1-3]. Recently, many groups have studied supported Group VIII metal-Re bimetallic combinations and noted enhancement in activity and chemoselectivity in reactions such as glycerol hydrogenolysis [4, 5] and cyclic ether and ester hydrogenolysis [6-11] as compared to the supported Group VIII metal alone.

The use of bimetallic precursor molecules in catalyst preparation has been reported to facilitate the formation of alloyed particles [1, 12]. For the Pd-Re bimetallic system, one such compound, Pd(NH₃)₄(ReO₄)₂, or the double complex salt (DCS), was prepared and described in detail by Zadesenets, et al. [13]. Upon reduction, they suggested the formation of a solid solution with an *hcp* geometry and a composition commensurate with the 1:2 Pd:Re molar ratio of the DCS. It should be noted, however, that the binary phase diagram for Pd-Re suggests that an alloy of that composition would be split into a Pd-rich phase (~90 at.% Pd) and an Re-rich phase (>95 at% Re) [14]. Nonetheless, encouraging results are reported for an activated carbon-supported DCS catalyst by Schubert, et al., in a patent for its use in hydrogenation of succinic anhydride [11].

We have demonstrated previously that PdRe/Al₂O₃ catalysts are effective for selective hydrogenation of furfural to FAL (see Chapters 2-3). Furthermore, FAL selectivity as well as the rate of furfural consumption correlates remarkably well with the ratio of H_{ads}/CO_{ads}, that is, the ratio of H to CO uptake in volumetric chemisorption experiments at

35°C. The current work expands on these results using PdRe/Al₂O₃ prepared from the DCS. TPHD, EXAFS spectra and STEM-EDX demonstrate that direct reduction of the supported DCS leads to small metal particles fostering intimate contact of Pd and Re. Catalysts with identical metal loading prepared by other methods lack the activity of PdRe/Al₂O₃ DCS due to Re coverage of Pd during calcination.

2 Experimental

Methods and materials for CO and H₂ chemisorption, TPR/TPHD, EXAFS spectroscopy, HR-STEM-EDX and furfural hydrogenation experiments are the same as described previously (Chapter 2). Only the methods and materials unique to the current work are described below.

2.1 DCS and Catalyst Preparation

The double complex salt, Pd(NH₃)₄(ReO₄)₂, was prepared by mixing saturated aqueous solutions of NH₄ReO₄ and Pd(NH₃)₄(NO₃)₂ at 25°C. Upon mixing, a light yellow salt precipitated from solution; the precipitate was filtered, washed thoroughly with deionized H₂O, and dried at room temperature. The purity of the compound was determined by Fourier transform-infrared (FTIR) and Raman spectroscopies, as shown and briefly explained in Figures 1-2. The catalyst, simply referred to as "DCS", was prepared by wet impregnation of a high purity γ -Al₂O₃ support (Grace-Davison MI-209, 183 m²/g BET surface area) with the DCS at a loading of 1.5 wt% Pd, 5 wt% Re, with a molar ratio of 1:2 Pd:Re, fixed by the composition of the precursor. Due to the insolubility of the precursor in the solvents tested (water, acetone, ethanol, ethyl acetate, acetonitrile), impregnation was carried out using an

aqueous solution slurry with a ratio of 10 mL/g support at 80°C. A rotary evaporator with a bath temperature of 80°C was used to warm the Al₂O₃ support and prevent precipitation of the DCS. Water was evaporated slowly under reduced pressure. When the catalyst appeared dry, it was removed and further dried at 110°C in air overnight. A portion of the sample was calcined at 350°C for 1 h in 0.6 L/min zero-grade air (certified, National Welders). It is referred to in the text as the calcined DCS catalyst. The metal content of each sample, as measured by ICP-OES, is given in Table 1.

Table 1. ICP-OES analysis of PdRe/Al₂O₃ catalysts (loading of DCS and calcined DCS equivalent)

Catalyst	Pd loading (wt %)	Re loading (wt %)
DCS	1.41	4.72
PdRe seq.	1.50	4.85
1.5% Pd	1.49	---
3% Pd	3.00	---
5% Re	---	5.02

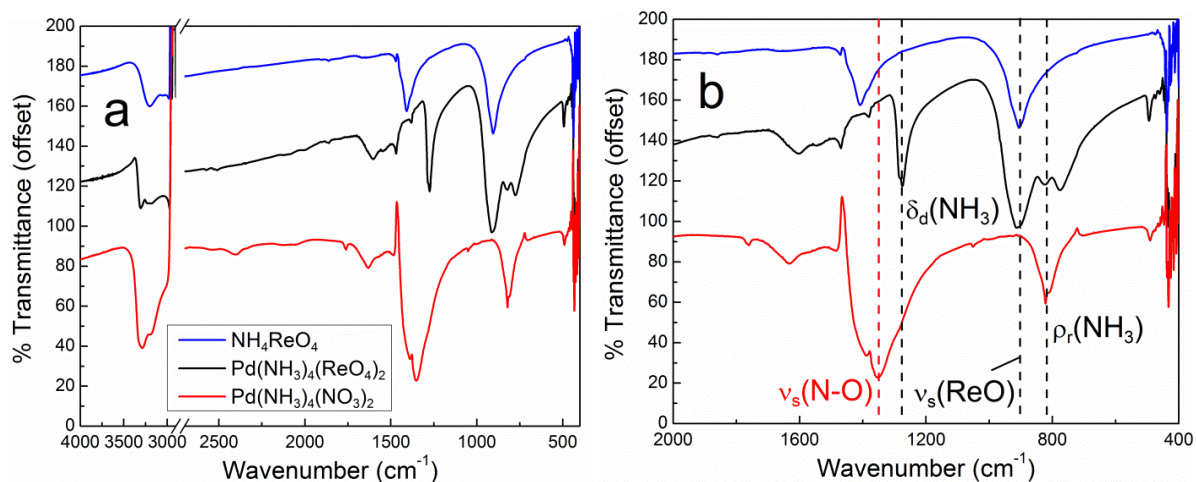


Figure 1. FT-IR spectrum of $\text{Pd}(\text{NH}_3)_4(\text{ReO}_4)_2$ compared to reactants used in its preparation: a) full range of $4000\text{--}400\text{ cm}^{-1}$, b) $2000\text{--}400\text{ cm}^{-1}$ with important vibrational modes indicated.

The solids were scanned in transmission in a mineral oil mull with NaCl disks. The disappearance of the $\nu_{\text{as}}(\text{N-O})$ mode apparent in $\text{Pd}(\text{NH}_3)_4(\text{NO}_3)_2$ and appearance of the $\nu_{\text{s}}(\text{Re=O})$ mode indicates replacement of the NO_3^- counterion with ReO_4^- during preparation of $\text{Pd}(\text{NH}_3)_4(\text{ReO}_4)_2$

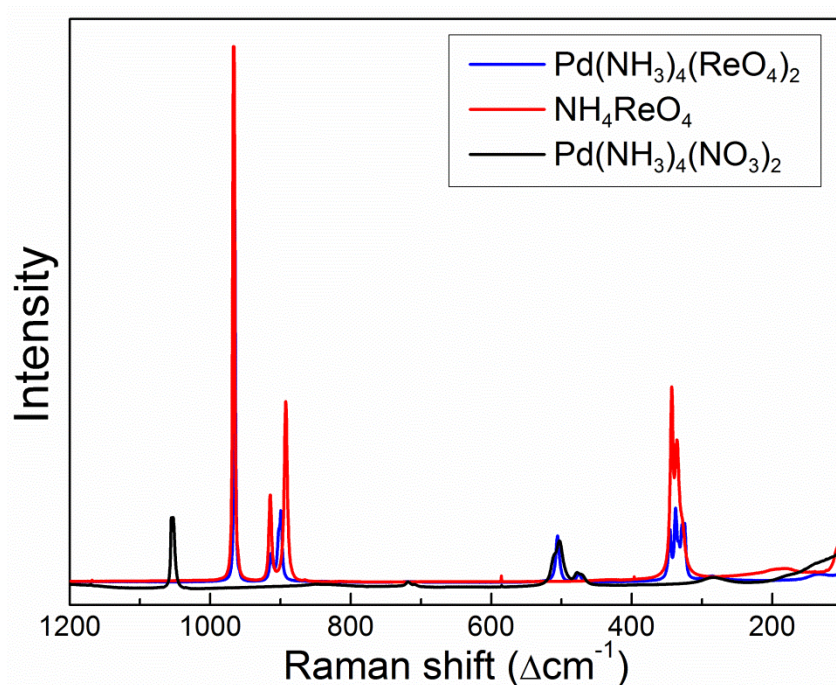


Figure 2. Raman spectrum of $\text{Pd}(\text{NH}_3)_4(\text{ReO}_4)_2$ compared to reactants used in its preparation

For comparison, a bimetallic catalyst with the same metal loading as the DCS was prepared using sequential impregnation. This catalyst is hereafter referred to as PdRe seq. First, 5% Re/Al₂O₃ was prepared from an aqueous solution of NH₄ReO₄. After drying overnight and calcining, this catalyst was impregnated with a pH 10 solution of Pd(NH₃)₄(NO₃)₂, and calcined again. Both calcinations were at 400°C for 3 h in flowing zero-grade air, similar to the PdRe(1:1) seq. catalysts which had the highest activity in furfural hydrogenation (Chapters 2 and 3). Also, 1.5% and 3% Pd/Al₂O₃ catalysts were prepared by incipient wetness impregnation of a pH 10 solution of Pd(NH₃)₄(NO₃)₂. After drying overnight at 110°C, these catalysts were calcined at 350°C for 1 h in flowing zero-grade air.

2.2 CO DRIFTS

The experimental materials, instrumentation and procedure are the same as described previously (Chapter 2), with the exception of thermal desorption experiments. After saturation coverage of CO at 20°C was observed, the catalyst was heated at 5°C/min to the desired temperature, held for 15 minutes, cooled to 20°C and a DRIFT spectrum was recorded. This process was repeated at successively higher temperatures.

3 Results and Discussion

3.1 TPR

The TPR profile of the uncalcined DCS-derived catalyst (Figure 3a) contains a single peak that corresponds to reductive decomposition of the double salt, i.e., simultaneous reduction of both metals. The small quantities of ammonia and water released during TPR of

the DCS catalyst were insufficient for accurate detection by on-line QMS; however, we performed a TGA experiment with on-line QMS to monitor reductive decomposition of the unsupported DCS. When the DCS is heated in flowing 5% H₂, ammonia (m/z 17) is released in two steps and a significant amount of water (m/z 18) is produced, as shown in Figure 4. Reduction of the 1.5% Pd catalyst takes place at 0-150°C with a maximum reduction temperature of ~15°C and continued uptake above that (Figure 3a). The Pd reduced at higher temperature includes isolated PdO_x complexes that interact strongly with the Al₂O₃ support (see Chapter 3). The TPR profile of 5% Re/Al₂O₃ prepared from NH₄[ReO₄] exhibits a peak reduction temperature of ~380°C (Figure 3a).

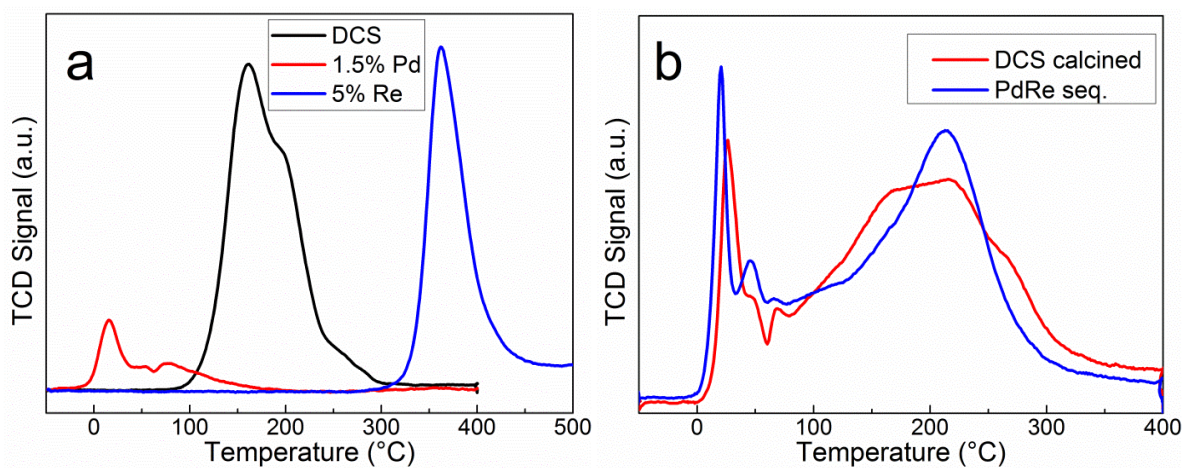


Figure 3. TPR of PdRe/Al₂O₃ in 5% H₂/Ar at 10°C/min

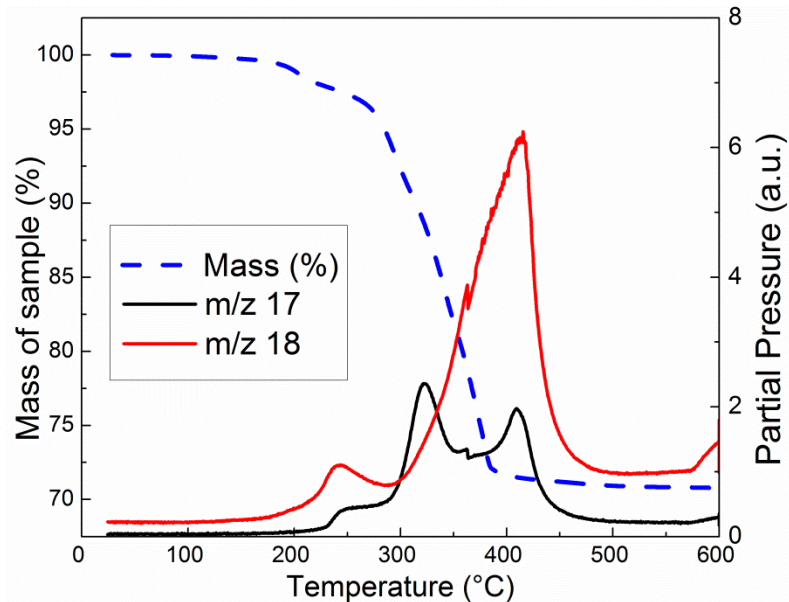


Figure 4. Overplot of mass loss (left ordinate) and QMS signal of species of interest (right ordinate – arbitrary units) during TGA of the unsupported DCS in 5% H₂/Ar, heated at 10°C/min.

We infer from the sharp PdO→Pd⁰ reduction feature evident at ~25°C that metal precursors in the calcined DCS and PdRe seq. catalysts were decomposed by the calcination process (Figure 1b). This peak is larger and at lower temperature for PdRe seq., which may suggest larger PdO particles in this catalyst (see Chapter 3). Primary reduction of Re is complete by ~325°C for these two catalysts, well below the peak Re reduction temperature of 5% Re/Al₂O₃ (Figure 3a). This lower reduction temperature is explained by hydrogen spillover from Pd which is reduced first and by hydrated [ReO₄]⁻ species which can migrate to be reduced near Pd particles [15]. The range of temperature over which Re is reduced can be explained by a diffusional lag for spilled over hydrogen to Re or [ReO₄]⁻ to Pd. These TPR profiles are similar to that of the PdRe(1:2) seq. catalyst described in Chapter 2 which had double the metal loading (3% Pd-10% Re), and was demonstrated to have poorly

dispersed Pd. Reduction of a significant fraction of the Re at high temperature (200°C) evidences uneven Pd distribution in these two catalysts.

3.2 CO and H₂ Chemisorption

CO chemisorption (CO/metal) on 1.5% Pd indicates that it is more highly dispersed than 3% Pd, although the uptake on a CO/g_{cat} basis is lower (Table 2). H₂ chemisorption also evidences small Pd particles, consistent with ~2 nm particles in 1.5% Pd and ~3 nm in 3% Pd using a basis of 1 H_{ads}/Pd surface site using the approximate relationship:

$$D(\%) = \frac{\text{surface Pd atoms}}{\text{total Pd atoms}} \approx \frac{1}{d(\text{nm})}$$

where D is dispersion, and d is the average particle diameter in units of nm. The uncalcined DCS-derived catalyst has the lowest CO uptake per metal atom and per g_{cat}. A decrease in H/metal ratio compared to CO/metal ratio is observed. Hydrogen chemisorption uptake at 35°C selectively probes Pd surface sites because at low temperatures dissociative chemisorption of H₂ is much more favorable over Pd than Re [16]. This explanation is supported by the increase in adsorbed H₂ at higher temperatures, as observed by Chadzynski and Kubicka [16], who inferred that H₂ chemisorption is an activated process on Re. A weakened H-surface bond is also predicted by DFT for PdRe surfaces [17, 18] and has been observed in PdRe overlayer catalysts [19, 20]. The CO/metal ratio of the calcined DCS-derived catalyst and PdRe seq. are higher by about a third than the uncalcined DCS-derived catalyst. Nevertheless, greater H₂ chemisorption suppression on these samples results in lower H/CO chemisorption uptake ratios at 35°C. We infer that the Pd surface area is lower

relative to Re surface area in the DCS catalyst after calcination (and in the sequentially prepared catalyst).

Table 2. CO and H₂ chemisorption specific uptake ($\mu\text{mol/g}_{\text{cat}}$ CO or H₂) and molar CO (or H)/metal ratio as determined by ICP-OES

Catalyst	CO chemisorption		H ₂ chemisorption					
	CO uptake	CO/metal	35°C		70°C		100°C	
			H ₂ uptake	H/metal	H ₂ uptake	H/metal	H ₂ uptake	H/metal
DCS	51.5	0.133	7.27	0.038	11.0	0.057	12.7	0.066
DCS calcined	67.6	0.175	5.96	0.031	19.3	0.100	17.2	0.089
PdRe seq.	73.4	0.183	7.64	0.038	11.8	0.059	16.1	0.080
1.5% Pd	59.4	0.640	31.7	0.452	27.7	0.396	27.8	0.398
3% Pd	105	0.373	49.7	0.353	42.2	0.299	41.3	0.293
5% Re	37.1	0.138	3.2	0.024	10.0	0.074	10.2	0.076

3.3 CO DRIFTS

CO DRIFT spectra shown in Figure 5 help elucidate the surface structures of the catalysts using CO as a probe molecule. The largest peak in each spectrum ($\sim 2080\text{ cm}^{-1}$) corresponds to linear (atop) CO on Pd [21-23]. The large broad peak at $1900\text{-}1950\text{ cm}^{-1}$ corresponds to two-fold bridging CO on Pd. Some three-fold bridging CO at lower frequencies contributes to this peak as well [22]. Two-fold bridging CO on low-index Pd planes, in particular (100) with intensity "borrowing" from (111), is suggested to be distinct from bridging CO on Pd(111) (Chapters 2-3 and [21, 23]), and can be observed at 1990 cm^{-1} . The peak at $\sim 2040\text{ cm}^{-1}$ corresponds to linear CO on Re (Figure 5d) [24].

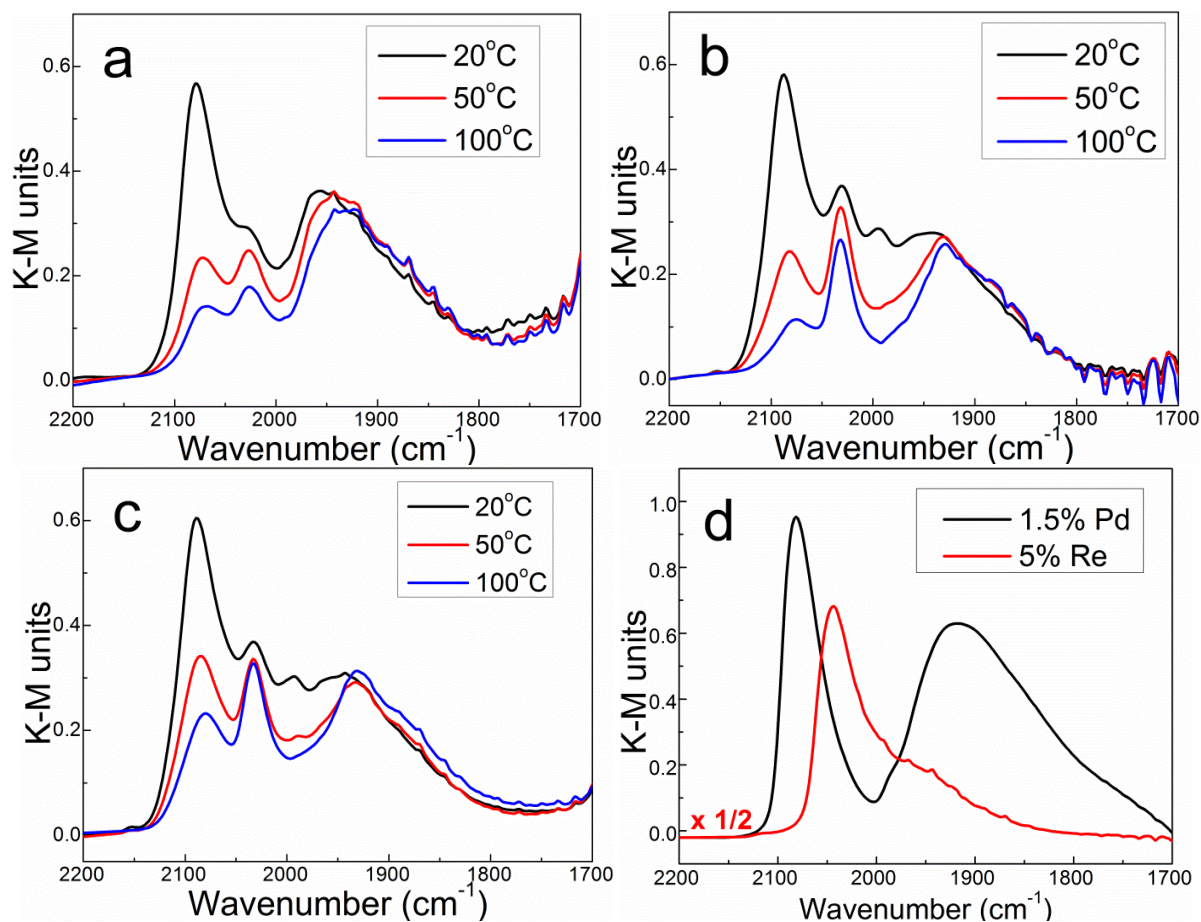


Figure 5. CO DRIFT spectra of PdRe/Al₂O₃ in Kubelka-Munk (K-M) units after 400°C reduction He purge and thermal desorption at the indicated temperatures on a.) DCS, b.) calcined DCS and c.) PdRe seq.; d.) at 20°C following reduction and He purge (5% Re not purged)

The intensities of atop CO peaks in DRIFT spectra of PdRe/Al₂O₃ catalysts is lower in Kubelka-Munk (K-M) units than in that of 1.5% Pd/Al₂O₃; however, the linear CO peak is significantly enhanced compared to the bridging CO peak. Rather than being an effect of the exposed Pd facet, this is explained by a mixed particle surface, comprising both Pd and Re sites. Small Re particles or clusters on the surface of Pd-rich particles are inferred to reduce the number of contiguous Pd sites necessary for CO to adsorb in a two- or three-fold bridging

configuration. The spectra of the calcined DCS-derived catalyst and PdRe seq. (Figures 5c and 5d, respectively) are essentially the same, suggesting a very similar surface structure for these two catalysts. The presence of larger Pd particles, that expose low-index surface planes, is suggested by the peak at 1990 cm^{-1} . This peak is notably absent from the uncalcined DCS-derived catalyst indicating that Pd particles are smaller (Figure 5a). Linear CO on Re is present as a weak band in the CO DRIFT spectra of all three bimetallic catalysts at 2040 cm^{-1} , as in 5% Re/Al₂O₃ in Figure 5d. The CO DRIFT spectrum of 1.5% Pd/Al₂O₃ evidences small Pd particles from the higher intensity of the atop CO peak relative to the bridging CO peak, and the absence of bridging CO on low-index planes. Small particles expose more corner and edge atoms which bind CO preferentially in the atop configuration, thus the peak at 2080 cm^{-1} is greater in magnitude than the bridging CO peak at $\sim 1930\text{ cm}^{-1}$.

CO DRIFT spectra following thermal desorption experiments at the indicated temperatures reflect relative CO-surface bond energies; weakly bound CO desorbs at lower temperatures. Following treatment at successively higher temperature, the CO surface coverage is reduced, and as a result dipolar coupling between adjacent adsorbed CO molecules is reduced. For CO peaks on Pd, $\tilde{\nu}_{\text{CO}}$ shifts to lower wavenumber. In spectra of all three catalysts PdRe/Al₂O₃ in Figure 5a-c, atop CO on Pd appears to be weakly bound, as this peak is greatly diminished by treatment at 50-100°C. Weak binding of atop CO on Pd is also the case for Pd/Al₂O₃ (Figure 6). Similar amounts of linear CO on Pd desorb from the two catalysts prepared using the DCS, but more of it remains on PdRe seq., suggesting that Pd sites on this catalyst bind CO more strongly. The bridging CO peak on the calcined DCS-derived catalyst and PdRe seq. at 1990 cm^{-1} is gone after desorption at 50°C, indicating that

this CO is bound weakly. Linear CO on Re binds more strongly, in particular over the calcined DCS-derived and PdRe seq. catalysts, on which most of this CO species remains bound after heating to 100°C. The binding energy of CO on Pd and Re is lowest for the uncalcined DCS-derived catalyst, which we infer to suggest intimate Pd-Re contact on surface. Bimetallic surfaces in general tend to adsorb CO more weakly than monometallics [12]. The reduced CO adsorption energy may explain the lower CO chemisorption uptake on this catalyst compared to the calcined DCS-derived and PdRe seq. catalysts. We note that desorption of bridging CO on Pd(100) occurs at 50°C, but desorption of bridging on Pd(111) and high-index Pd surface planes does not occur until higher temperatures than those tested for these catalysts. It is evident that some bridging CO is removed by 200°C thermal desorption from 3% Pd/Al₂O₃ (Figure 6).

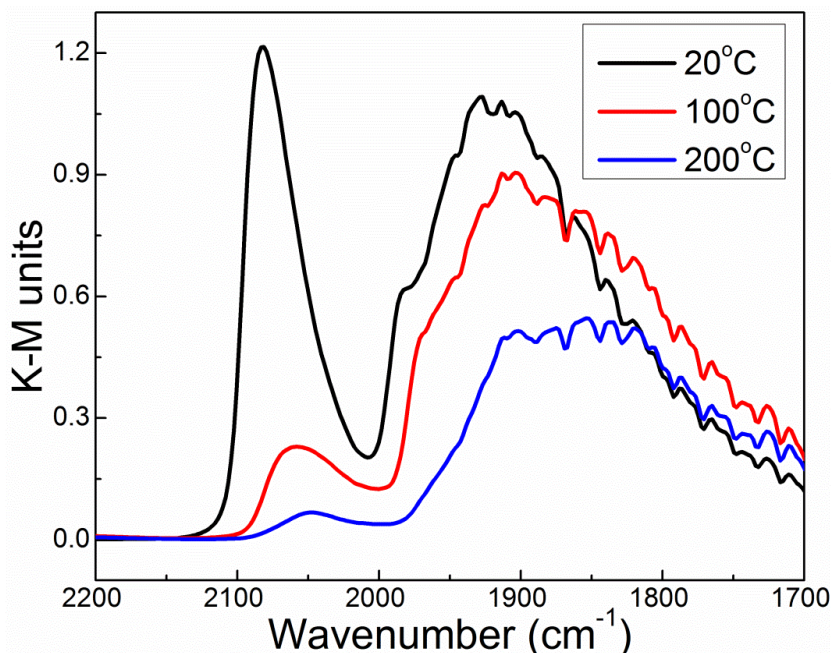


Figure 6. CO DRIFTS on 3% Pd/Al₂O₃ at 20°C and after thermal desorption at the temperatures indicated

3.4 TPHD

The H₂ evolution peak (seen as an inverse peak) at 50°C in Figure 7 indicates the thermal decomposition of β-PdH_x [25-27]. The size of the hydride decomposition peak (reflecting the PdH_x stoichiometry) depends on Pd particle size and alloying. Alloying of Pd with Re has been demonstrated to suppress PdH_x formation [26], and this explains the notable lack of H₂ evolution in the TPHD profile of the uncalcined DCS-derived catalyst. Previous TPHD experiments covering the range of -50 to 50°C on PdRe/Al₂O₃ catalysts have evidenced similar small H₂ evolution features at -50 to 0°C and between 0-25°C (Chapter 2). We infer that these are due to decomposition of less stable PdH_x species, e.g., in very small particles or in alloyed particles. These two features are also missing from the profile of the uncalcined DCS-derived catalyst, which is taken as further evidence of Pd-Re alloying. Others who have studied PdRe catalysts with TPHD have begun from higher temperatures or used a different gas mixture or ramp rate and have not observed these features [26, 27]. These low temperature features are similar in all catalysts, except the uncalcined DCS-derived catalyst. It is clear that the β-PdH_x decomposition peak in 1.5% Pd is smaller than in the calcined DCS-derived and PdRe seq catalysts. This diminution of the peak suggests that there are Pd particles in the two bimetallic catalysts which are larger than Pd particles in 1.5% Pd, in agreement with the presence of bridging CO bound to low-index surface planes on the former and missing on the latter (*vide supra*). Quantitative results for hydride decomposition are displayed in Table 3. All values are below the bulk value of 0.65 H/Pd [25]. The H/Pd ratio of 0.175 for 1.5% Pd suggests an Pd dispersion of >60% [28], which is in agreement with CO chemisorption. To summarize, TPHD suggests strongly that Pd-Re

alloying and/or small Pd particles are present in the uncalcined DCS-derived catalyst after reduction, but that this interaction does not develop if the DCS is decomposed by calcination, or if the precursors are added in sequence. More definitive proof of particle structure, namely Pd-Re alloying, is discussed below.

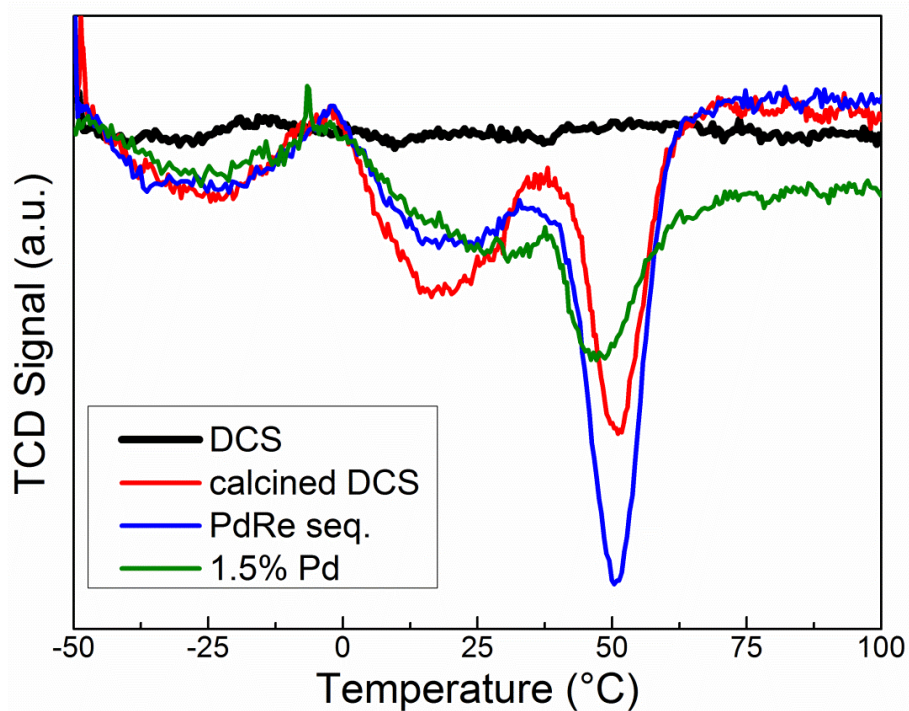


Figure 7. TPD of PdRe/Al₂O₃ in 5% H₂/Ar at 10°C/min

Table 3. H/Pd ratios based on H₂ evolution in TPD

Catalyst	H/Pd		Total
	<0°C	>0°C	
DCS	0	0	0
DCS calcined	0.054	0.223	0.278
PdRe seq.	0.061	0.300	0.361
1.5% Pd	0.031	0.144	0.175

3.5 EXAFS Spectroscopy

The uncalcined DCS-derived catalyst was analyzed by EXAFS spectroscopy at the Pd K- and Re L_{III}-edges to investigate alloying suggested by TPHD. The EXAFS chi data and Fourier transform at each edge are shown in Figure 8. The Fourier transforms were fit using Pd-Pd, Pd-Re, Re-Re, Re-Pd and Re-O contributions (absorber-backscatterer, respectively) using paths calculated from single-scattering theory using FEFF6. The two edges were fit simultaneously over the ranges indicated in Table 4, which contains the values for the adjustable parameters used in fitting each path. Comparisons of the Fourier transform (FT) magnitudes of the data and fits are shown in Figure 9a. The real part of the FT and contributions from each FEFF path of the Pd K-edge (Figure 9b) and Re L_{III}-edge (Figure 9c) evidence destructive interference of the homo- and heterometallic FEFF paths at both edges.

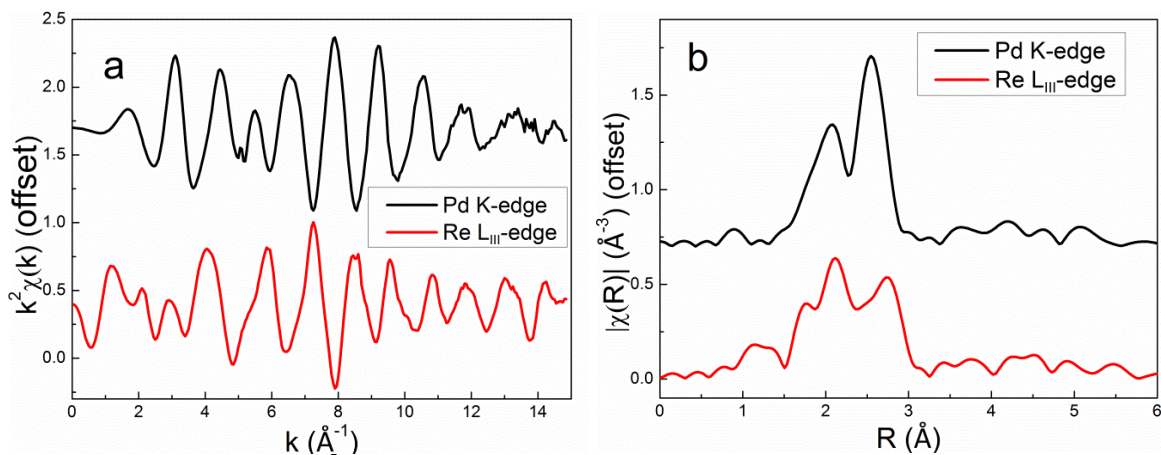


Figure 8. a.) EXAFS (k^2 -weighting) of PdRe/ Al_2O_3 DCS and b.) magnitude FT (Pd K k -range: 2.5-14.1 \AA^{-1} ; Re L_{III} k -range: 3.5-14.0 \AA^{-1})

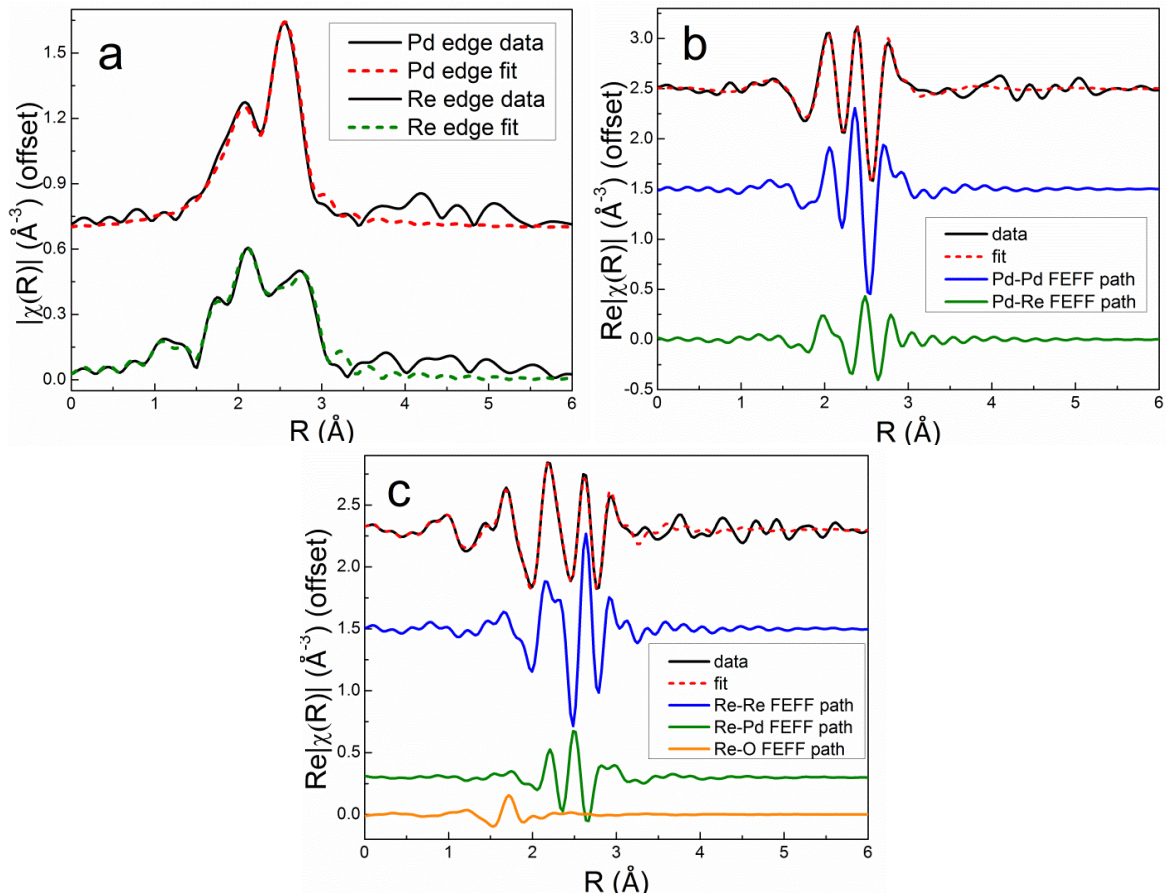


Figure 9. PdRe/Al₂O₃ DCS EXAFS Fourier transform fits: a) magnitude, b) real part of Pd K-edge FT, c) real part of Re L_{III}-edge FT

The total first-shell metal coordination number about Pd is 7.0, which suggests metal particles <5 nm in diameter based on a cuboctahedral particle shape [21]. The Re contribution to the Pd Fourier transform is much higher than observed in other PdRe/Al₂O₃ catalysts (Chapters 2-3). The average Pd coordination shell is only 63 at% Pd, which is well below the ~90 at% Pd composition expected from the binary phase diagram [14]. This may be explained by Re-rich bimetallic particles. The Pd contribution to the Re Fourier transform is half as large, as expected from the 2:1 Re:Pd molar composition of the catalyst. This is

consistent the Via criterion [29], which says that the ratio of the coordination numbers at each edge should match the molar ratio of the metals in bimetallic catalysts. Vegard's law suggests that the bond length of the alloy should be the weighted average of the two component metal's bond lengths (Pd-Pd: 2.75 Å, Re-Re: 2.75 Å); however, fitting of the EXAFS for the DCS evidences a shorter Pd-Re bond length. This surprising result has been observed previously in x-ray diffraction (XRD) and EXAFS spectroscopy of Pd-Re catalysts [27, 30] and bulk alloys [26, 31]. Meitzner, et al., determined a Pd-Re bond length via EXAFS spectroscopy of PdRe(1:1)/Al₂O₃ [30]; however, this Pd-Re bond length is significantly shorter than fitting of the DCS-derived catalyst suggests. The current result in better agreement with the 2.71 and 2.74 Å bond lengths observed via XRD for two distinct alloy phases which result from impregnation of Pd black with KReO₄ [26].

Table 4. EXAFS Fourier transform fitting parameters for uncalcined DCS-derived catalyst after 400°C reduction and He purge

Path	N	R (Å)	σ^2 (10 ⁻³ Å ²)	ΔE_0 (eV)	R-value
Pd-Pd	4.4 ± 0.5	2.74 ± 0.01	5.9 ± 0.8	-2.7 ± 0.7	0.0051
Pd-Re	2.6 ± 0.5	2.72 ± 0.01	4.3 ± 1.3	-2.7 ± 0.7	
Re-Re	5.4 ± 0.6	2.73 ± 0.01	5.9 ± 0.8	9.0 ± 1.1	0.0077
Re-Pd	1.3 ± 0.3	2.72 ± 0.01	4.3 ± 1.3	9.0 ± 1.1	
Re-O	0.5 ± 0.2	2.06 ± 0.02	(1.0)*	9.0 ± 1.1	

*Fixed during fit

Pd K-edge fit range: k-space 2.7-12.8 Å⁻¹; R-space 1.0-3.0 Å

Re L_{III}-edge fit range: k-space 3.6-14.0 Å⁻¹; R-space 1.4-3.1 Å

The Re-Re and Re-Pd coordination numbers must be adjusted because of the Re-O contribution to the first coordination shell of Re. Assuming the octahedral structure of ReO₂

for the oxide present in the uncalcined DCS-derived catalyst after reduction, the adjusted Re-metal coordination number is 7.3, which agrees well with the total first-shell coordination number of Pd. The Re-O bond length in the fit of the data is 2.06 Å, which is similar to the weighted average Re-O bond length in ReO₂, 2.00 Å [32]. This bond length is consistent with the Re-O interatomic distance observed in fitting EXAFS spectra of other M-Re (M=Pd, Rh, Pt) by Tomishige, et al., who attribute it to partially reduced ReO_x species [33-35]. Tetravalent Re has been shown to be present in Re/Al₂O₃ catalysts by x-ray photoelectron spectroscopy [36] and electron spin resonance [37]. Furthermore, the Al₂O₃ support stabilizes Re⁴⁺ against reduction >500°C [37]. Bare, et al., observed a 2.06-Å Re-O bond in 0.7% Re/Al₂O₃-MOR, but ascribed it to an Re-O single bond tethering of perrhenate (ReO₄⁻) tetrahedra to the Al₂O₃ support [38]; however, this implies that there should be a Re-O bond at 1.72 Å with a coordination number three times greater than that indicated for Re-O at 2.06 Å. No such contribution is consistent with the Re EXAFS data; hence, we infer that the bond length corresponds to partially reduced Re (Re⁴⁺) species.

3.6 HAADF-EDX Imaging

Metal nanoparticles ~1.5 nm in size are easily visible in HAADF-STEM images of the uncalcined DCS-derived catalyst after reduction (Figure 10a-b). These very small particles are distributed across the Al₂O₃ support. The STEM-EDX image in Figure 10c corresponds to the area of the HAADF-STEM image in Figure 10b. The particles in the middle of the image evidence intimate Pd-Re contact. Small Pd clusters and Pd atoms are adjacent to the Re-rich particles seen in the middle of the image. The yellow pixels show up where red and green pixels are superimposed; however, due to the small size of the field and

very small particle size, the signal collected was low compared to the field shown in Figures 10d-e. These larger nanoparticles (2-10 nm in diameter) are also rich in Re, but with much more yellow caused by the association of Pd with these particles. Pd clusters (<1 nm) appear to be uniformly distributed, but are primarily associated with Re. Intimate contact of Pd clusters with Re nanoparticles may explain the reduced CO-Re and CO-Pd bond energy observed in CO DRIFTS thermal desorption experiments on this catalyst.

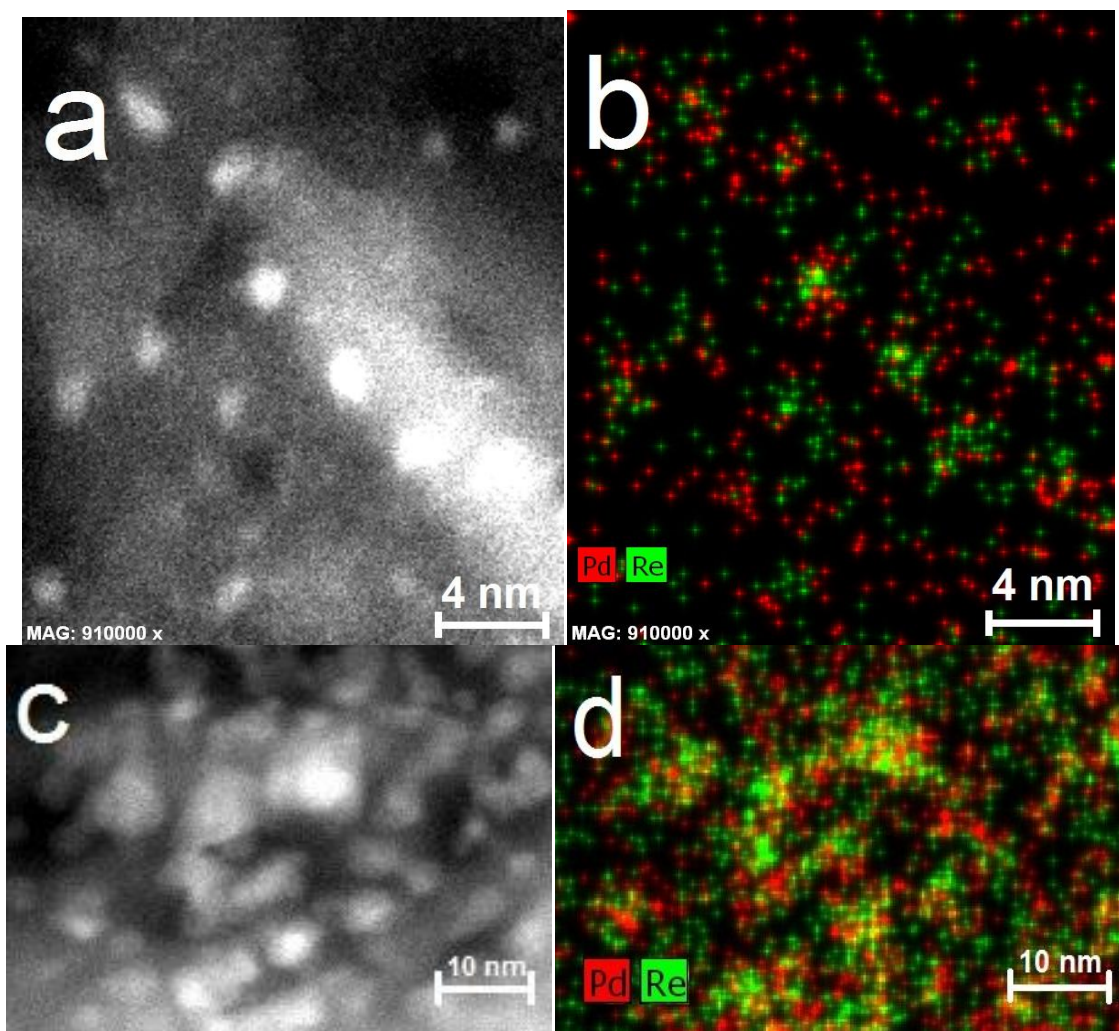


Figure 10. STEM images of PdRe/Al₂O₃ DCS: a.) and c) HAADF-STEM images and b.) and d) corresponding composite STEM-EDX images; Pd – red, Re – green, superposition – yellow

Small metal particles 1-2 nm in size are also spread over the support in the calcined DCS-derived catalyst after reduction, as shown by HAADF imaging (Figure 11a); however, EDX analysis demonstrates that these particles are almost all Re (Figure 11b). A few isolated Pd atoms or clusters are visible in the EDX image, but the overall ratio of Pd to Re is dramatically lower than the 1:2 atomic composition of the catalyst. Large, irregular metal

particles (>50 nm diameter) were apparent at the edges of some Al₂O₃ particles HAADF-STEM (Figure 11c). These large particles are composed primarily of Pd, and Re particles much less than 10 nm in diameter cover the Al₂O₃ and these Pd particles (Figure 11d). Thus, we infer that calcination causes segregation of the two metals and significant sintering of PdO, giving rise to large Pd particles. Intimate contact of Re with the surface of these particles is suggested by Figure 6d. Moreover, some alloying is still suggested by β -PdH_x suppression in TPHD: Pd particles of these size would be expected to have the bulk H/Pd value of 0.65 [28].

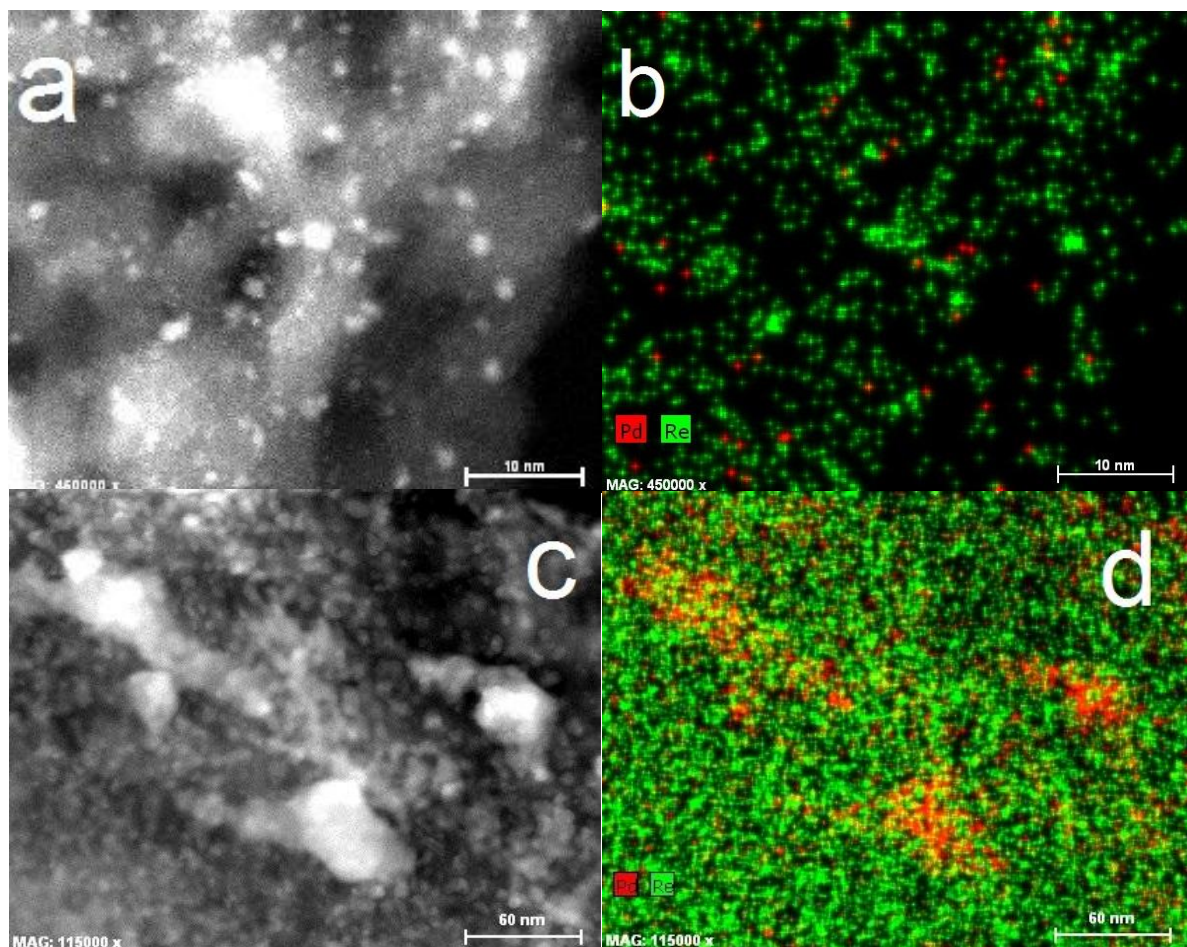


Figure 11. STEM images of calcined DCS -prepared catalyst: a) and c) HAADF –STEM images b) and d) corresponding composite STEM-EDX images; Pd – red, Re – green, superposition – yellow

3.7 Furfural Hydrogenation

Three furfural reaction pathways account for the observed products formed by PdRe/Al₂O₃ catalysts. Decarbonylation of furfural leads to furan which may be saturated to THF. Selective hydrogenation of the aldehyde moiety leads to FAL, the desired product. Saturation of the furfural molecule leads to THFAL. 2-Methyl furan may be produced by

hydrodeoxygenation of furfural or FAL. Ring opening products, e.g., 1,5-pentanediol, were not formed under these conditions.

The rate of furfural consumption is equal to the sum of the production rates of these six products (Figure 12). The uncalcined DCS-derived catalyst is nearly twice as active as any of the other three catalysts. FAL selectivities are ~70-80% over PdRe/Al₂O₃ catalysts, but only ~40% over 3% Pd/Al₂O₃. There is a large increase in FAL selectivity over all three bimetallic catalysts. The selectivity of each catalyst correlates well with the H/CO chemisorption uptake ratios given for these catalysts in Table 2. The calcined DCS-derived catalyst, which has the lowest H/CO ratio has the highest selectivity to FAL, 80.6%. PdRe seq. also has higher selectivity to FAL than the uncalcined DCS-derived catalyst.

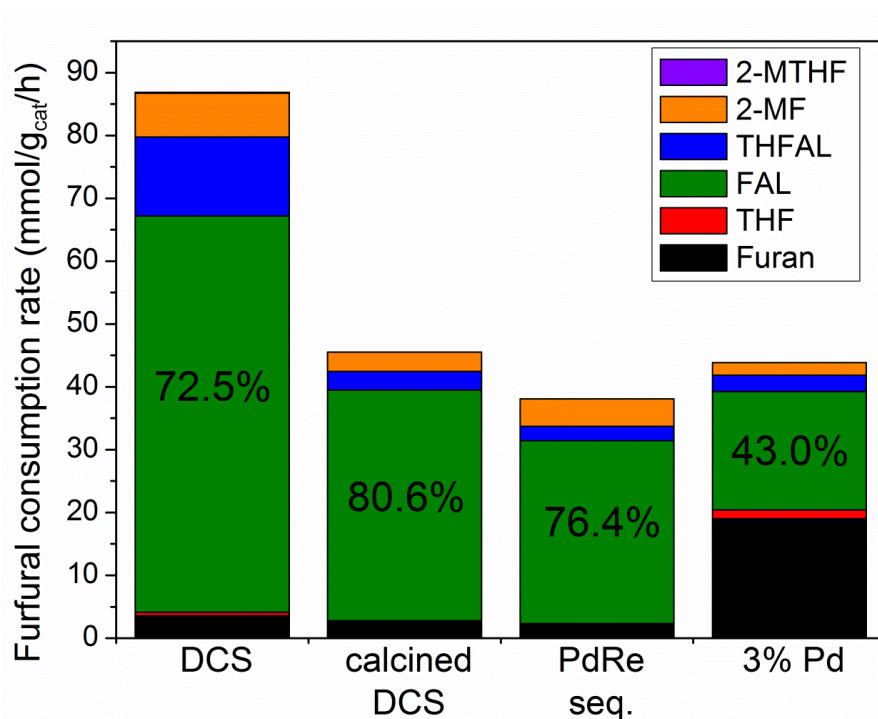


Figure 12. Furfural consumption rate (sum of production rates) over Al₂O₃-supported catalysts at 150°C and ambient pressure; FAL selectivity indicated

The rate of furfural consumption and the production rates were normalized by CO and H uptake to calculate turnover frequencies (TOF). The TOFs calculated for 3% Pd on each basis are equal (Table 5). Furfural and FAL TOFs on the basis of H uptake (since this is more selective for Pd surface sites) are more than an order of magnitude larger for the uncalcined DCS catalyst than for 3% Pd. The furfural and FAL TOFs over the uncalcined DCS catalyst are more than double those of the calcined DCS catalyst and PdRe seq. The enhanced TOFs on the DCS catalyst indicate higher intrinsic activity of the active sites in this catalyst.

Table 5. TOFs (min^{-1}) at 150°C based on CO and H₂ chemisorption uptake at 35°C

Basis	Furfural		FAL		Furan		2-MF		THFAL	
	CO	H	CO	H	CO	H	CO	H	CO	H
DCS	28.1	99.6	20.4	72.3	1.2	4.1	2.2	8.0	4.1	14.4
DCS calcined	11.2	63.6	9.1	51.3	0.7	3.9	0.8	4.3	0.7	4.1
PdRe seq.	8.6	41.5	6.6	31.8	0.5	2.4	1.0	4.8	0.5	2.5
3% Pd	6.9	7.3	3.0	3.2	3.0	3.2	0.3	0.3	0.4	0.4

We sought to correlate the significant differences in catalyst morphology between the PdRe/Al₂O₃ catalysts, evident in TPR/TPHD, CO DRIFTS and HAADF-EDX, with furfural hydrogenation performance. Although CO and H₂ chemisorption uptake on all three Pd-Re catalysts suggests similar metal dispersion at face value, CO DRIFT spectra and STEM-EDX evidence smaller Pd particles in the uncalcined DCS-derived catalyst. A higher fraction of Pd surface area comprises Pd(100) and Pd(111) surface planes in the calcined DCS-derived catalyst and PdRe seq., which corresponds to the large Pd particles in STEM-EDX images of the calcined DCS catalyst. The small Re particles in contact with the surface of these large

Pd particles suppress H₂ chemisorption to a high degree. There is surface contact of Pd and Re in the uncalcined DCS-derived catalyst, too, as seen in the close association of the two metals in HAADF-EDX; however, the average metal particle size is much smaller. Furthermore, the lack of a doubly bridging CO peak on low-index Pd surface planes in the CO DRIFT spectrum suggests smaller Pd particles. This observation may indicate that sites with adjacent Pd-Re atoms on smaller particles enhances the furfural hydrogenation rate more than the same sites on Pd(100). DFT calculations by Pallassana and Neurock [39] predict that small Re ensembles or substituted Re atoms on the Pd(111) surface decrease the energy barrier for the hydrogenation of acetaldehyde as compared to a monometallic Pd surface. Another difference between HAADF-EDX images of the calcined and uncalcined catalyst is that there are small Pd clusters on the surface of Re-rich particles evident in the latter. These Pd atoms may be expected to be bonded to Re (based on the Pd-Re coordination number in EXAFS). Calculations by Pallasana, et al. [17, 18], evidence significant changes to the *d* band of Pd atoms in Pd pseudomorphic overlayers on Re. The *d* band configuration of a Pd monolayer on the Re(0001) surface makes these sites more favorable to hydrogenation reactions [39]. Thus, these Pd sites may be expected to have distinct behavior from Pd sites on the surface of Pd-rich particle. In order to create these sites in the DCS catalyst, direct reduction is necessary. It is clear that calcination has a deleterious effect on the catalyst, probably due to sintering of Pd (or PdO).

4 Conclusions

- Preparation of a Pd-Re double complex salt, $\text{Pd}(\text{NH}_3)_4(\text{ReO}_4)_2$, and a novel preparation method for a PdRe/ Al_2O_3 DCS catalyst were demonstrated.
- This catalyst shows the highest activity in furfural hydrogenation to FAL on both a rate and a per site basis as compared to a calcined analogue and PdRe seq.
- Direct reduction of this catalyst leads to small, alloyed nanoparticles in this catalyst evidenced by EXAFS and STEM-EDX; calcination causes the two metal oxides to segregate, as evidenced by high temperature Re reduction in TPR. Large Pd particles form in the latter case are inferred to result from sintering of PdO during calcination.
- Enhanced FAL selectivity and concomitant suppression of H_2 chemisorption uptake indicates that the active sites comprise adjacent Re and Pd metal atoms.
- The increased intrinsic activity of sites on the uncalcined catalyst may be explained by the effect of Pd particle size: the smaller metal particles with intimate Pd-Re contact on more stepped surfaces gives rise to increased hydrogenation activity.

5 Acknowledgements

This work was funded by Eastman Chemical Company for funding through the Center of Excellence. ICP-OES analysis was performed by Eastman Chemical Company. This research used resources of the Advanced Photon Source, a U.S. Department of Energy (DOE) Office of Science User Facility operated for the DOE Office of Science by Argonne

National Laboratory under Contract No. DE-AC02-06CH11357. We gratefully acknowledge the loan of EXAFS equipment from Dr. Jeffrey Miller, and the assistance of Dr. Joshua Wright and Dr. John Katsoudas in operating beamline MR-CAT-10BM. The authors acknowledge the use of the Analytical Instrumentation Facility at NCSU, which is supported by the State of North Carolina and the National Science Foundation, and, in particular, Dr. Xiahan Sang for assistance with STEM-EDX.

References

- [1] A.S. Fung, M.R. McDevitt, P.A. Tooley, M.J. Kelley, D.C. Koningsberger, B.C. Gates, *J. Catal.*, **140** (1993) 190-208.
- [2] L.W. Jossens, E.E. Petersen, *J. Catal.*, **76** (1982) 265-273.
- [3] J.L. Xiao, R.J. Puddephatt, *Coord. Chem. Rev.*, **143** (1995) 457-500.
- [4] D.A. Simonetti, E.L. Kunkes, J.A. Dumesic, *J. Catal.*, **247** (2007) 298-306.
- [5] E.L. Kunkes, D.A. Simonetti, J.A. Dumesic, W.D. Pyrz, L.E. Murillo, J.G.G. Chen, D.J. Buttrey, *J. Catal.*, **260** (2008) 164-177.
- [6] M. Chia, Y.J. Pagan-Torres, D. Hibbitts, Q.H. Tan, H.N. Pham, A.K. Datye, M. Neurock, R.J. Davis, J.A. Dumesic, *J. Am. Chem. Soc.*, **133** (2011) 12675-12689.
- [7] K.Y. Chen, S. Koso, T. Kubota, Y. Nakagawa, K. Tomishige, *Chemcatchem*, **2** (2010) 547-555.
- [8] S. Koso, I. Furikado, A. Shima, T. Miyazawa, K. Kunimori, K. Tomishige, *Chem. Comm.*, (2009) 2035-2037.
- [9] S. Koso, Y. Nakagawa, K. Tomishige, *J. Catal.*, **280** (2011) 221-229.
- [10] M.A. Mabry, W.W. Prichard, S.B. Ziemecki, in: U.S.P. Office (Ed.), E. I. du Pont de Nemours and Company, United States Patent 4550185, 1985.
- [11] M. Schubert, M. Hesse, R.H. Fischer, T. Constantinescu, in, United States Patent 7214641, 2007.
- [12] O.S. Alexeev, B.C. Gates, *Ind. Eng. Chem. Res.*, **42** (2003) 1571-1587.
- [13] A.V. Zadesenets, S.P. Khranenko, Y.V. Shubin, I.A. Baidina, S.V. Korenev, *Russ. J. Coord. Chem.*, **32** (2006) 374-379.
- [14] B. Predel, O.E. Madelung, in: Landolt-Börnstein - Group IV Physical Chemistry, SpringerMaterials.
- [15] S.B. Ziemecki, G.A. Jones, J.B. Michel, *J. Catal.*, **99** (1986) 207-217.
- [16] G.W. Chadzynski, H. Kubicka, *Thermochim. Acta*, **158** (1990) 353-367.

- [17] V. Pallassana, M. Neurock, L.B. Hansen, B. Hammer, J.K. Norskov, *Phys. Rev. B*, **60** (1999) 6146-6154.
- [18] V. Pallassana, M. Neurock, L.B. Hansen, J.K. Norskov, *J. Chem. Phys.*, **112** (2000) 5435-5439.
- [19] M.P. Latussek, B.P. Spigarelli, R.M. Heimerl, J.H. Holles, *J. Catal.*, **263** (2009) 306-314.
- [20] M.D. Skoglund, J.H. Holles, *Catal. Lett.*, **143** (2013) 966-974.
- [21] G. Agostini, R. Pellegrini, G. Leofanti, L. Bertinetti, S. Bertarione, E. Groppo, A. Zecchina, C. Lamberti, *J. Phys. Chem. C*, **113** (2009) 10485-10492.
- [22] E. Groppo, S. Bertarione, F. Rotunno, G. Agostini, D. Scarano, R. Pellegrini, G. Leofanti, A. Zecchina, C. Lamberti, *J. Phys. Chem. C*, **111** (2007) 7021-7028.
- [23] T. Lear, R. Marshall, J.A. Lopez-Sanchez, S.D. Jackson, T.M. Klapotke, M. Baumer, G. Rupprechter, H.J. Freund, D. Lennon, *J. Chem. Phys.*, **123** (2005) 13.
- [24] W. Daniell, T. Weingand, H. Knozinger, *J. Mol. Catal. A*, **204** (2003) 519-526.
- [25] J.A. McCaulley, *J. Phys. Chem.*, **97** (1993) 10372-10379.
- [26] S.B. Ziemecki, J.B. Michel, G.A. Jones, *React. Sol.*, **2** (1986) 187-202.
- [27] A. Malinowski, W. Juszczak, M. Bonarowska, J. Pielaszek, Z. Karpinski, *J. Catal.*, **177** (1998) 153-163.
- [28] G. Fagherazzi, A. Benedetti, S. Polizzi, A. Dimario, F. Pinna, M. Signoretto, *Catal. Lett.*, **32** (1995) 293-303.
- [29] G.H. Via, K.F. Drake, G. Meitzner, F.W. Lytle, J.H. Sinfelt, *Catal. Lett.*, **5** (1990) 25-33.
- [30] G. Meitzner, G.H. Via, F.W. Lytle, J.H. Sinfelt, *J. Chem. Phys.*, **87** (1987) 6354-6363.
- [31] E.M. Savitskii, V.P. Tsyganova, M.A. Tylkina, *Izv. Akad. Nauk SSSR, Neorg. Mater.*, **7** (1962) 1917.
- [32] A. Magneli, *Acta Chem. Scand.*, **11** (1957) 28-33.
- [33] S. Koso, H. Watanabe, K. Okumura, Y. Nakagawa, K. Tomishige, *J. Phys. Chem. C*, **116** (2012) 3079-3090.

- [34] T. Ebashi, Y. Ishida, Y. Nakagawa, S.-i. Ito, T. Kubota, K. Tomishige, *J. Phys. Chem. C*, **114** (2010).
- [35] Y. Amada, H. Watanabe, M. Tamura, Y. Nakagawa, K. Okumura, K. Tomishige, *J. Phys. Chem. C*, **116** (2012) 23503-23514.
- [36] J. Okal, W. Tylus, L. Kepinski, *J. Catal.*, **225** (2004) 498-509.
- [37] M.S. Nacheff, L.S. Kraus, M. Ichikawa, B.M. Hoffman, J.B. Butt, W.M.H. Sachtler, *J. Catal.*, **106** (1987) 263-272.
- [38] S.R. Bare, S.D. Kelly, F.D. Vila, E. Boldingh, E. Karapetrova, J. Kas, G.E. Mickelson, F.S. Modica, N. Yang, J.J. Rehr, *J. Phys. Chem. C*, **115** (2011) 5740-5755.
- [39] V. Pallassana, M. Neurock, *J. Catal.*, **209** (2002) 289-305.

CHAPTER 5: SUMMARY AND OUTLOOK

Palladium (Pd) and rhenium (Re) do not form a continuous range of bulk solid solutions [1]; however, as explained by Sinfelt in his seminal work on bimetallic catalysts, metals which are immiscible in the bulk may still bond to form bimetallic nanoparticles over a large range of composition [2]. Ponc and Bond explain more precisely that metal nanoparticles produced by chemical means may survive equilibration and annealing as a frozen solution, i.e., a non-equilibrium solution preserved by the inability of metal atoms in sufficiently small particles to overcome energy barriers to form new surfaces or interfaces necessary to achieve phases with equilibrium compositions [3]. This investigation demonstrates that PdRe/C and PdRe/Al₂O₃ are valuable bimetallic catalysts for total hydrodeoxygenation (HDO) of biomass-derived compounds (specifically, guaiacol and anisole) to hydrocarbons and for selective hydrogenation of furfural to furfural alcohol, respectively. Advanced characterization of PdRe/C and PdRe/Al₂O₃ catalysts using x-ray absorption fine structure (XAFS) spectroscopy and high-angle annular dark field (HAADF) scanning transmission electron microscopy (STEM) with energy dispersive x-ray (EDX) analysis provides a deeper understanding of their atomic-scale structures. This final chapter summarizes the important results and conclusions and suggests additional research.

1 Bimetallic Synergy in PdRe Catalysts

1.1 HDO

Wildschut, et al. screened many supported-Group VIII metal catalysts in HDO of fast pyrolysis oils and found that carbon-supported noble metals, particularly Pd/C and Ru/C, gave the highest yield of liquid products with the lowest oxygen content [4]. Based on these results for Pd/C, we hypothesized that addition of Re, which is more oxophilic than Pd and activates C-O bonds more easily [5], would lead to better HDO performance than Pd/C alone. To test this hypothesis, a PdRe/C catalyst was prepared with a 1:1 atomic ratio by conventional incipient wetness co-impregnation, and its HDO performance was compared to monometallic catalysts, including Pd/C, Re/C and Ru/C, at 300°C and 1-6 atm H₂. Lignin-derived phenolic compounds comprise a substantial fraction of bio-oils [6, 7], and two model compounds, guaiacol and anisole, were chosen. One of the most significant findings was that Pd/C is unable to fully deoxygenate guaiacol—deoxygenation proceeds as far as phenol (or cyclohexanol), but phenol is not deoxygenated to benzene over Pd/C. In contrast, benzene and anisole are produced from guaiacol over Re/C, which suggests that Re can catalyze phenol HDO. Therefore, removal of a hydroxyl substituent from a phenyl ring via HDO occurs over Re but not over Pd. Moreover, Pd and Re monometallic catalysts differ in selectivity toward methoxy substituents: Pd is selective to scission of the phenyl C-O bond (demethoxylation), whereas Re is selective to hydrogenolysis of the methyl C-O bond to form methane (demethylation). It is assumed that benzene is produced by HDO of catechol and phenol subsequent to demethylation over Re.

Several considerations suggest that the superior catalytic performance of PdRe/C is due to synergy between Pd and Re rather than simply their independent action. Given the availability of multiple HDO pathways for methoxy group removal and the capability of Re to deoxygenate phenol to benzene, it is not surprising that PdRe/C exhibits high yields of benzene and cyclohexane, the desired hydrocarbon products. However, the total yield of benzene and cyclohexane is higher than the sum of these yields over Pd/C and Re/C. Similarly, the phenol production rate from guaiacol (which occurs by one of the two aforementioned pathways) is greater than the sum of the rate over Pd/C and Re/C. The anisole production rate is also greater over PdRe/C than the sum over the two monometallic catalysts, indicating that another significant HDO pathway is available with the bimetallic catalyst. Moreover, anisole HDO results show that PdRe/C is particularly effective at converting anisole to benzene. Indeed, the benzene formation rate is equivalent to the anisole formation rate in HDO of guaiacol, second only to the phenol production rate. Phenol and anisole are both primary products but benzene is not, which indicates that phenol and anisole are the two most important intermediate products in the HDO of guaiacol to benzene. The rate of benzene production over Pd/C and Re/C is negligible. These results support the conclusion that both metals work together to achieve total HDO of guaiacol and other phenolic compounds. The synergistic interaction of Pd and a more oxophilic metal for total HDO is also observed for PdFe/C catalysts [8]. Finally, the interaction of the two metals is also inferred from the ability of PdRe/C to maintain high conversion of guaiacol with time on stream, unlike Re/C, which is initially highly active, but deactivates rapidly before stabilizing at a much lower conversion. In short, HDO of guaiacol to benzene over Re/C is possible, but

PdRe/C exhibits dramatic enhancement in the rate of formation of benzene due to the availability of multiple pathways for deoxygenation of guaiacol, and does not suffer significant deactivation.

We attribute the HDO performance of PdRe/C to bimetallic surface sites comprising Re metal clusters on Pd nanoparticles. Even though the two metals are not highly miscible in the bulk [1], extended x-ray absorption fine structure (EXAFS) spectroscopy evidences Pd-Re bonding in all of the catalysts, regardless of the support or preparation method. Contact between clusters and small particles of Re with the surface of Pd-rich particles is evident from STEM-EDX. These results support Pd-Re surface alloying.

1.2 Selective Hydrogenation

Recent interest in the production of specialty chemicals, in particular alcohols, from oxygenated organics derived from woody biomass, motivated us to investigate PdRe/Al₂O₃ catalysts for selective hydrogenation of furfural to furfural alcohol (FAL). Our hypothesis was that PdRe/Al₂O₃ catalysts would be chemoselective, favoring the hydrogenation of carbonyl moieties, e.g., aldehydes, ketones, carboxylic acids, over hydrogenation of C-C double bonds. Furfural was chosen as a model compound for products of hemicellulose pyrolysis. The desired product, FAL, its saturated analogue, tetrahydrofurfuryl alcohol (THFAL), 2-methyl furan (2-MF) and furan were all observed as primary products. It was observed that the bimetallic catalysts were more selective to FAL than Pd/Al₂O₃, and more active as compared to monometallic catalysts prepared from the same precursors. Furfural decarbonylation to furan is favored over Pd/Al₂O₃ catalysts, in particular highly dispersed catalysts made from tetraamminepalladium (TA) nitrate, whereas hydrogenation products,

FAL and THFAL are favored over PdRe/Al₂O₃. There is excellent correlation between the sum of the production rates of FAL and THFAL with the furfural consumption rate over all PdRe/Al₂O₃ catalysts tested (Figure 1). The selectivity to FAL and THFAL is roughly 82%, as indicated by the slope of a linear fit of these data. This is a surprising result: regardless of preparation method or Pd:Re ratio, the selectivity to the hydrogenation pathway is nearly the same irrespective of catalytic activity.

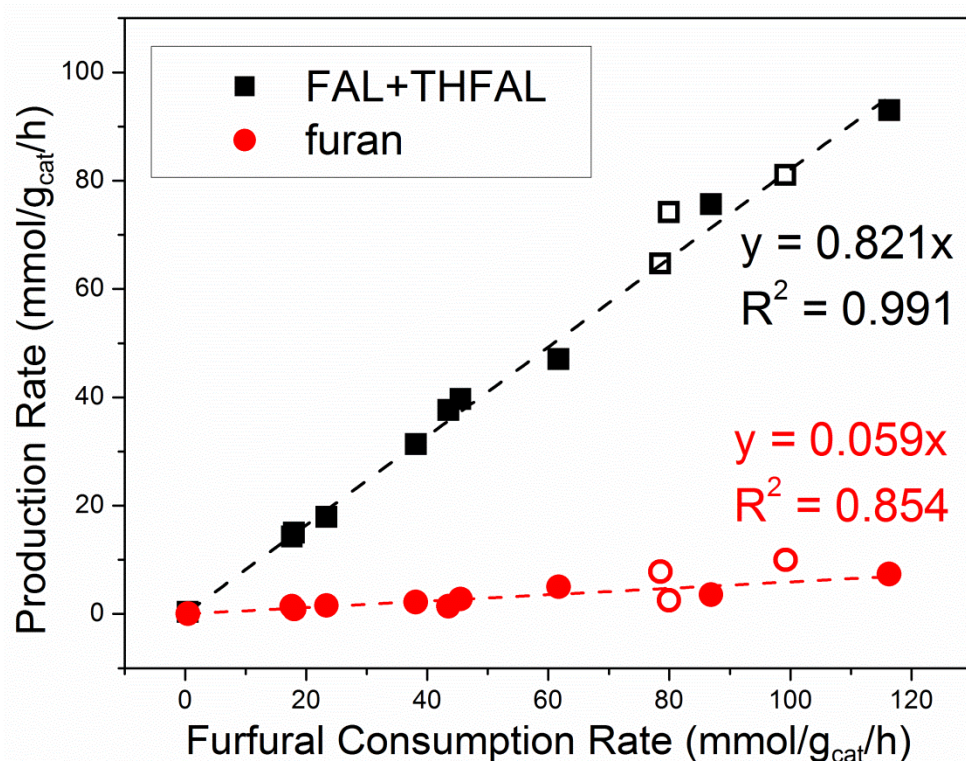


Figure 1. Production rates of furan and the sum of FAL and THFAL versus furfural consumption rate; the slope, calculated by linear regression, is indicated in the figure. Open symbols – Al₂O₃ (A) supported PdRe catalysts; closed symbols – Al₂O₃ (B) supported catalysts.

Although selectivity to the hydrogenation pathway was approximately constant, furfural turnover frequencies (TOFs) over PdRe/Al₂O₃ catalysts varied by approximately an order of magnitude. Furfural TOF over Pd/Al₂O₃ catalysts is nearly constant regardless of average particle size, which suggests that Pd sites in the monometallic catalysts have similar intrinsic activities. The range of TOFs observed over PdRe/Al₂O₃ has two possible explanations: 1) a difference in intrinsic activity of sites, or 2) CO and H₂ chemisorption are unreliable for counting active sites in PdRe/Al₂O₃ catalysts. To the latter point, it is expected that both CO chemisorption will measure both Pd and Re sites, but that H₂ will primarily chemisorb on Pd and not Re [9]. Indeed, uptake of CO is up to ten times greater on Re/Al₂O₃ than H₂ uptake. We observe that the ratio of H_{ads}/CO_{ads} from volumetric chemisorption for PdRe/Al₂O₃ catalysts fall somewhere between the extremes of H/CO \approx 1 for Pd/Al₂O₃ and H/CO \approx 0.1 for Re/Al₂O₃. It is logical to infer that the suppression of H₂ chemisorption is due to a mixed metal surface in bimetallic catalysts, but there are two possible contributions. The first contribution comes from Re covering Pd sites and physically blocking chemisorption; Re is unable to dissociatively adsorb H₂ at 35°C [9]. The second contribution is a reduced H-surface binding energy on mixed Pd-Re particle surfaces as predicted by DFT calculations [10, 11] and confirmed by H₂ chemisorption on catalysts made by selective deposition of Pd on Re⁰ particles [12].

There is an interesting and somewhat unexpected correlation between furfural TOF (on either a CO or H basis) and the H_{ads}/CO_{ads} ratio (Figure 2). More samples were prepared on Al₂O₃ (B), so the trend is more apparent in Figure 2b. TOF increases with decreasing H/CO ratio from H/CO \approx 1 for Pd monometallic catalysts to H/CO \approx 0.3. The maximum TOF

in Figures 2a and 2b corresponds to PdRe/Al₂O₃ prepared by direct reduction of the supported double complex salt (DCS), [Pd(NH₃)₄(ReO₄)₂]. It should be noted that Re-Pd⁰/Al₂O₃ (B), which has a 1:1 atomic Pd:Re ratio, has a similarly high TOF. Below an H/CO ratio of ~0.3, there is a precipitous decline in TOF toward the almost negligible TOF of Re/Al₂O₃, as traced out by the catalysts with a molar Pd:Re ratio of 1:2. Therefore, this ratio, which gives a quantitative indication of H₂ chemisorption suppression, describes the average intrinsic activity of these catalysts. A mixed Pd-Re surface is necessary for enhanced hydrogenation activity, but the highest activity per site occurs with the optimum surface composition. If the surface is Pd-poor (low H₂ chemisorption), the measured TOF suffers, as in the case of PdRe(1:2)/Al₂O₃ catalysts (except the uncalcined DCS-derived catalyst), and the TOFs approach the value for Re/Al₂O₃. One possible explanation is that the most active site consists of an ensemble of Pd and Re atoms on the surface and that a surface composition corresponding to an H_{ads}/CO_{ads} ratio of ~0.3 favors these surface structures.

Extended x-ray absorption fine structure (EXAFS) spectroscopy evidences Pd-Re bonding in all of the catalysts, regardless of the support or preparation method. Clusters and nanoparticles of Re (~1-2 nm diameter) are observed on the surface of Pd-rich particles in STEM-EDX images of all PdRe/Al₂O₃ catalysts tested. The most significant difference between these catalysts is the size of Pd particles. Catalysts prepared from Pd(NO₃)₂ all have very large Pd-rich particles (>10 nm diameter), whereas catalysts prepared from Pd(NH₃)₄(NO₃)₂ have much smaller Pd-rich particles (<5 nm diameter). The DCS-derived catalyst presents a special case in that we observe particularly small Pd particles (~1 nm) in

diameter and even Pd clusters on the surface of Re-rich particles. These images support the mixed surface composition, but they are not conclusive as to the surface geometry of sites on all the different catalysts. Bimetallic surface ensembles remain a likely explanation, rather than a concrete conclusion; however, DFT calculations on mixed Pd-Re surfaces also point to sites comprising small Re ensembles on a Pd(111) surface as most favorable for acetic acid hydrogenolysis to ethanol [5]. Substitutional alloying of Re in Pd-rich particles, i.e., in the "bulk" of 20-30 nm diameter particles, is observed in some cases. This was detected by temperature-programmed hydride decomposition (TPHD), in which H₂ from the β-PdH_x phase desorbs at ~55°C. The stoichiometry of the hydride decreases for smaller Pd particles and for substitutionally alloyed PdRe particles. In some cases, particularly PdRe/Al₂O₃ made by co-impregnation (co.), no β-PdH_x phase was detected. EXAFS results for this catalyst also suggest a contracted Pd-Re bond and an alloy composition equivalent to that observed by Meitzner, et al., on a similar PdRe/Al₂O₃ catalyst [13]. Although this is an interesting result, the H/CO ratio of this catalyst is ~0.5, which leads to relatively low furfural TOF. Furfural hydrogenation results for PdRe/Al₂O₃ co. agree with the results for other catalysts which still have extensive hydride decomposition features, and therefore do not have significant Re migration into the bulk of Pd-rich particles. This means that the surface composition is key to predicting the activity in PdRe catalysts, rather than alloying in the "bulk" of particles.

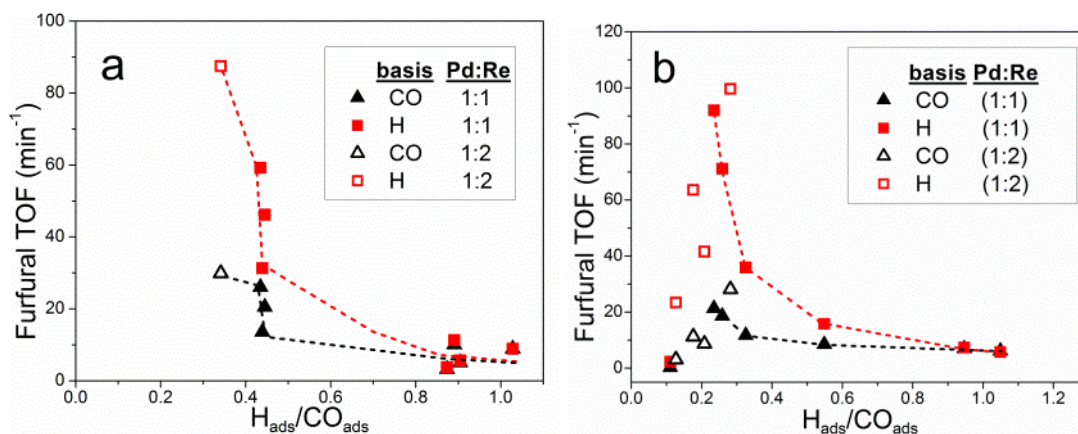


Figure 2. Furfural TOF versus the ratio of strongly adsorbed H/CO in chemisorption experiments at 35°C for a.) PdRe/Al₂O₃ (A) catalysts and b.) PdRe/Al₂O₃ (B) catalysts

2 Future Work

2.1 HDO

First, PdRe/C should be tested for use in catalytic upgrading of fast pyrolysis oil samples. Initially, upgrading of condensates, i.e., bio-oil, may be done in a batch reactor, but we suggest that a more effective approach would be continuous upgrading of pyrolysis vapors downstream from a pyrolysis unit. Furthermore, we propose to combine in situ catalytic upgrading using mesoporous metal oxides (e.g., Al-MCM-41) and microporous acid zeolites (e.g., H-MOR, H-ZSM-5 and H-Beta) with ex-situ catalytic upgrading using PdRe/C. The proposed reactor scheme is shown in Figure 3. High-surface-area solid acids mentioned above catalyze dehydration and cracking reactions under pyrolysis conditions [14], facilitating the break-up of large molecules commonly encountered in biomass pyrolysis. Such a reactor scheme would allow optimization the conversion of levoglucosan (the main product of cellulose pyrolysis), high-molecular-weight phenolic compounds and tars in the

pyrolysis reactor, and the catalytic deoxygenation of organic acids, furfurals, furans, and substituted phenolic compounds in the downstream fixed-bed reactor.

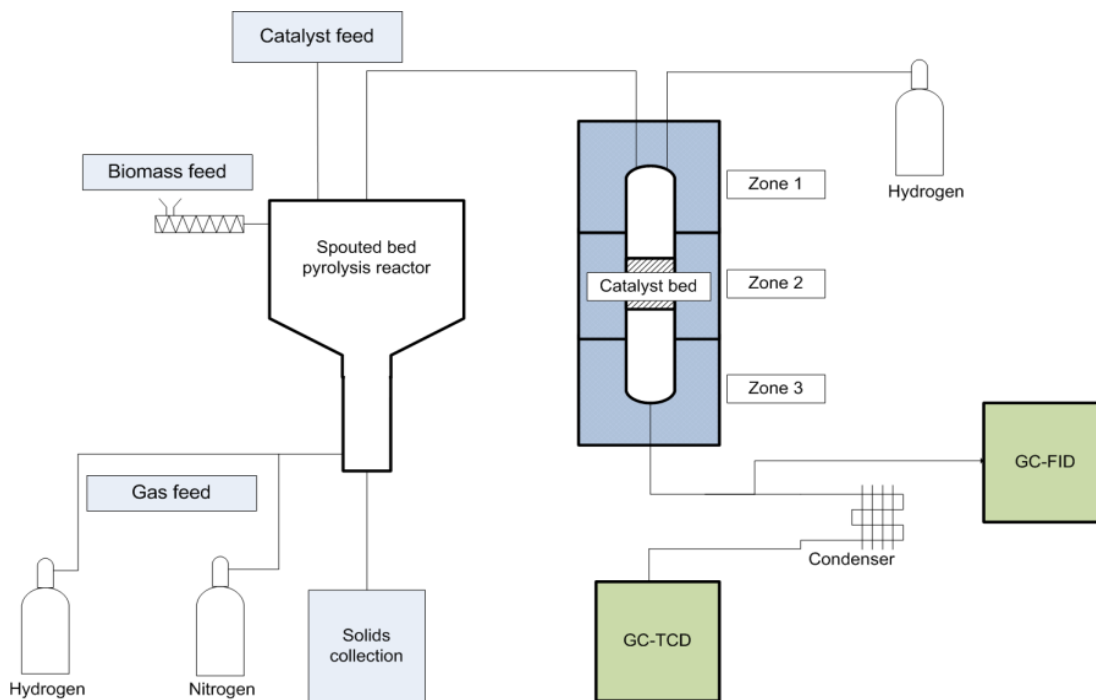


Figure 3. Schematic diagram of bench-scale apparatus for continuous biomass pyrolysis and catalytic upgrading

Also, investigation of PdRe/Al₂O₃ catalysts has pointed the way to controlling catalyst morphology in Pd-Re catalysts, especially using the DCS. Preparation of a DCS-derived PdRe/C is expected to result in a highly active catalyst as compared to the conventionally prepared PdRe/C catalyst used in guaiacol and anisole HDO. The importance of a mixed metal surface for creation of highly active sites in HDO and selective hydrogenation reactions suggests that studying the effect of Pd-Re surface composition on HDO reactions would be worthwhile.

2.2 *Selective Hydrogenation*

The success of PdRe/Al₂O₃ in selective hydrogenation of furfural suggests further experiments, beginning with a related compound, 5-hydroxymethyl-furfural (5-HMF). High selectivity to 5-hydroxymethyl-furfuryl alcohol is expected over these catalysts. We also suggest the use of PdRe/Al₂O₃ catalysts in selective hydrogenation of other carbonyl-containing organics, such as organic acids, dicarboxylic acids, other aldehydes and ketones, following the promising results of previous studies [15-17].

References

- [1] B. Predel, O. Madelung, in: Landolt-Börnstein - Group IV Physical Chemistry, SpringerMaterials.
- [2] J.H. Sinfelt, Bimetallic Catalysts: Discoveries, Concepts, and Applications, John Wiley and Sons, 1983.
- [3] V. Ponec, G.C. Bond, Catalysis by Metals and Alloys, Elsevier Science B.V., Amsterdam, The Netherlands, 1995.
- [4] J. Wildschut, F.H. Mahfud, R.H. Venderbosch, H.J. Heeres, *Ind. Eng. Chem. Res.*, **48** (2009) 10324-10334.
- [5] V. Pallassana, M. Neurock, *J. Catal.*, **209** (2002) 289-305.
- [6] A. Oasmaa, E. Kuoppala, Y. Solantausta, *Energy Fuels*, **17** (2003) 433-443.
- [7] L. Ingram, D. Mohan, M. Bricka, P. Steele, D. Strobel, D. Crocker, B. Mitchell, J. Mohammad, K. Cantrell, C.U. Pittman, *Energy Fuels*, **22** (2008) 614-625.
- [8] J.M. Sun, A.M. Karim, H. Zhang, L. Kovarik, X.H.S. Li, A.J. Hensley, J.S. McEwen, Y. Wang, *J. Catal.*, **306** (2013) 47-57.
- [9] G.W. Chadzynski, H. Kubicka, *Thermochim. Acta*, **158** (1990) 353-367.
- [10] V. Pallassana, M. Neurock, L.B. Hansen, B. Hammer, J.K. Norskov, *Phys. Rev. B*, **60** (1999) 6146-6154.
- [11] V. Pallassana, M. Neurock, L.B. Hansen, J.K. Norskov, *J. Chem. Phys.*, **112** (2000) 5435-5439.
- [12] M.D. Skoglund, J.H. Holles, *Catal. Lett.*, **143** (2013) 966-974.
- [13] G. Meitzner, G.H. Via, F.W. Lytle, J.H. Sinfelt, *J. Chem. Phys.*, **87** (1987) 6354-6363.
- [14] J. Adam, M. Blazso, E. Meszaros, M. Stocker, M.H. Nilsen, A. Bouzga, J.E. Hustad, M. Gronli, G. Oye, *Fuel*, **84** (2005) 1494-1502.
- [15] M.A. Mabry, W.W. Prichard, S.B. Ziemecki, in: U.S.P. Office (Ed.), E. I. du Pont de Nemours and Company, United States Patent 4550185, 1985.

[16] M. Schubert, M. Hesse, R.H. Fischer, T. Constantinescu, United States Patent 7214641, 2007.

[17] M. Kitson, P.S. Williams, in: U.S.P. Office (Ed.), The British Petroleum Company, United States Patent 5149680, 1992.